Investigation of Crosslinked Network Design and Light Scattering Modeling in Support of Vat Photopolymerization of High-Performance Materials

Keyton D. Feller

Dissertation submitted to the Faculty of the

Virginia Polytechnic Institute and State University

in partial fulfillment of the requirements for the degree of

Doctor of Philosophy

in

Macromolecular Science and Engineering

Christopher B. Williams, Co-chair

Timothy E. Long, Co-chair

J. Robert Mahan

Richey Davis

Robert B. Moore

Carolina Tallon

Feb 17, 2023

Blacksburg, Virginia

Keywords: Additive Manufacturing, Vat Photopolymerization, Process Modeling, Stereolithography, Light Scattering, Monte Carlo Ray-Tracing

Copyright 2023, Keyton D. Feller

Investigation of Crosslinked Network Design and Light Scattering Modeling in Support of Vat Photopolymerization of High-Performance Materials

Keyton D. Feller

(ABSTRACT)

The reliance on low-viscosity and photoactive resins limits the accessible properties for vat photopolymerization (VP) materials required for engineering applications. This has limited the adoption of VP for producing end-use parts, which typically require high MW polymers and/or more stable chemical functionality. Decoupling the viscosity and molecular weight relationship for VP resins has been completed recently for polyimides and high-performance elastomers by photocuring a scaffold around polymer precursors or polymer nanoparticles, respectively. Both of these materials are first shaped by printing a green part followed by thermal post-processing to achieve the final part properties. This dissertation focuses on improving the processability of these material systems by (i) investigating the impact of scaffold architecture and polysalt monomer composition on photocuring, thermal post-processing, and resulting thermomechanical properties and (ii) developing a Monte Carlo ray-tracing (MCRT) simulation to predict light scattering and photocuring behavior in particle-filled resins, specifically zinc oxide nanoparticles in a rigid polyester resin and styrene butadiene rubber latex resin.

The first portion of the dissertation introduces VP of a tetra-acid and half-ester-based polysalt resin derived from 4,4'-oxydiphthalic anhydride and 4,4-oxydianiline (ODPA-ODA), a fully aromatic polyimide with high glass transition temperature and thermal stability. This

polyimide, and polyimides like this, find use in demanding industries such as aerospace, automotive and electronic applications. The author evaluated the hypothesis that a non-bound triethylene glycol dimethacrylate (TEGDMA) scaffold would facilitate more efficient scaffold burnout and thus achieve parts with reduced off-gassing potential at elevated temperatures. Both resins demonstrated photocuring and were able to print solid and complex latticed parts. When thermally processed to 400 ^{o}C, only 3% of the TEGDMA scaffold remained within the final parts. The half-ester resin exhibits higher char yield, resulting from partial degradation of the polyimide backbone, potentially caused by lack of solvent retention limiting the imidization conversion. The tetra-acid exhibits a T_g of 260^{o}C, while the half-ester displays a higher T_g of 380 ^{o}C caused by the degradation of the polymer backbone, forming residual char, restricting chain mobility. Solid parts displayed a phase-separated morphology while the half-ester latticed parts appear solid, indicating solvent removal occurs faster in the half-ester composition, presumably due to reduced polar acid functionality. This platform and scaffold architecture enables a modular approach to produce novel and easily customizable UV-curable polyimides to easily increase the variety of polyimides and the accessible properties of printed polyimides through VP.

The second section of this dissertation describes the creation and validation of a MCRT simulation to predict light scattering and the resulting photocured shape of a ZnO-filled resin nanocomposite. Relative to prior MCRT simulations in the literature, this approach requires only simple, easily acquired inputs gathered from dynamic light scattering, refractometry, UV-vis spectroscopy, beam profilometry, and VP working curves to produce 2D exposure distributions. The concentration of 20 nm ZnO varied from 1 to 5 vol% and was exposed to a 7X7 pixel square (250 μm) from 5 to 11 s. Compared to experimentally produced cure profiles, the MCRT simulation is shown to predict cure depth within 10% (15 μm) and cure widths within 30% (20 μm), below the controllable resolution of the printer. Despite this success, this study was limited to small particles and low loadings to avoid polycrystalline

particles and maintain dispersion stability for the duration of the experiments.

Expanding the MCRT simulation to latex-based resins which are comprised of polymer nanoparticles that are amorphous, homogeneous, and colloidally stable. This allows for validating the MCRT with larger particles (100 nm) at higher loadings. Simulated cure profiles of styrene-butadiene rubber (SBR) loadings from 5 vol% to 25 vol% predicted cure depths within 20% (μm) and cure widths within 50% (μm) of experimental values. The error observed within the latex-based resin is significantly higher than in the ZnO resin and potentially caused by the green part shrinking due to evaporation of the resin's water, which leads to errors when trying to experimentally measure the cure profiles.

This dissertation demonstrates the development of novel and functional materials and creation process-related improvements. Specifically, this dissertation presents a materials platform for the future development of unique photocurable engineering polymers and a corresponding physics-based model to aid in processing.

Investigation of Crosslinked Network Design and Light Scattering Modeling in Support of Vat Photopolymerization of High-Performance Materials

Keyton D. Feller

(GENERAL AUDIENCE ABSTRACT)

Vat Photopolymerization (VP) is a 3D printing process that uses ultraviolet (UV) light to selectively cure liquid photosensitive resin into a solid part in a layer-by-layer fashion. Parts produced with VP exhibit a smooth surface finish and fine features of less than 100 μm (i.e., width of human hair). Recoating the liquid resin for each layer limits VP to low-viscosity resins, thus limiting the molecular weight (and thus performance) of the printed polymers accessible. Materials that are low molecular weight are limited in achieving desirable properties, such as elongation, strength, and heat resistance. Solvent-based resins, such as polysalt and latex resins have demonstrated the ability to decouple the viscosity and molecular weight relationship by eliminating polymer entanglements using low-molecular-weight precursors or isolating high-molecular-weight polymers into particles. This dissertation focuses on expanding and improving the printability of these methods.

The second chapter of the dissertation investigates the impact of scaffold architecture in printing polyimide polysalts to improve scaffold burnout. Polysalts are polymers that exist as dissolved salts in solution, with each monomer holding two electronic charges. When heated, the solvent evaporates and the monomers react to form a high molecular-weight polymer. While previous work featured a polysalt that was covalently bonded to the monomers, the polysalt in this work is made printable by co-dissolving a scaffold. The polysalt resins are photocured and thermally processed to polymerize and imidize into a high-molecular-weight

polymer, while simultaneously pyrolyzing the scaffold. Using a co-dissolved scaffold allows the investigation of two different monomers of tetra-acid and half-ester functionality. The half-ester composition underwent degradation during heating, increasing the printed parts' glass transition or softening point. The scaffold had little impact on the polysalt polymerization or final part properties and was efficiently removed, with only 3% remaining in final parts. The composition and properties of the monomers selected played a bigger role due to partial degradation altering the properties of the final parts. Overall, this platform and scaffold architecture allows for a larger number of polyimides to be accessible and easily customizable for future VP demands.

The third chapter describes the challenges of processing photocurable resins that contain particles due to the UV light scattering in the resin vat during printing. When the light from the printer hits a particle, it is scattered in all directions causing the layer shape to be distorted from the designed shape. To overcome this, a Monte Carlo ray-tracing (MCRT) simulation was developed to mimic light rays scattering within the resin vat. The simulation was validated by comparing simulation results against experiment trials of photocuring resins containing 20nm zinc oxide (ZnO) nanoparticles. The MCRT simulation predicted all the experimental cure depths within 10% (20 μm) and cured widths within 30% (15 μm) error. Despite the high accuracy, this study was limited to small particles and low concentrations. Simulating larger particles is difficult as the simulation assumes each particle to be uniform throughout its volume, which is atypical of large ceramic particles.

The fourth chapter enables high particle volume loading by using a highly stretchable styrene-butadiene rubber (SBR) latex-based resin. Latex-based resins maintain low viscosity by separating large polymer chains into nano-particles that are noncrystalline and uniform. When the chains are separated, they cannot interact or entangle, keeping the viscosity low even at high concentrations (>30 vol%). Like the ZnO-filled resin, the latex resin is experimentally cured and the MCRT simulation predicts the resulting cure shape. The MCRT

simulation predicted cure depths within 20% (100 μm) and over-cure widths within 50% (100 μm) of experimental values. This error is substantially higher than the ZnO work and is believed to be caused by the water evaporating from the cured resin resulting in inconsistent measurements of the cured dimensions.

Dedication

To my family and former educators for their continued support

Acknowledgments

I am grateful for the opportunity to pursue my Ph.D. at Virginia Tech. I am fortunate for the consistent support from my parents, Steve and Angie, and my siblings, Kyle and Kelsey. I am grateful for the encouragement you have all provided to me throughout this journey. I would also like to thank my girlfriend Alisa Omelchenko for her love, unrivaled support, and patience as she put up with constant polymer-based conversations at every social gathering throughout the years.

I want to thank my advisors, Dr. Christopher B. Williams, and Dr. Timothy E. Long. Dr. Williams for the opportunity to perform research in the DREAMS Lab as his first chemist. Your advisement has changed how I approach problems and enabled me to develop an adaptive skill set to be a chemist, engineer, and programmer simultaneously. Thank you for also having my best interest in mind and providing academic and finical support through this degree. Your constant positivity made this degree an incredibly joyful experience. Dr. Long, for his polymer chemistry teachings and training through memorable lectures, labs, group meetings, and research projects. I would also like to provide a special thanks to committee member Dr. J. Robert Mahan, for being an incredibly valuable committee member and for your patience in teaching me your ray tracing methods throughout the pandemic. Your assistance in both reviewing papers and providing helpful discussions are greatly appreciated.

I am grateful for having supportive educators during high school, specifically Mr. Vorland for always creating an interesting learning environment and stimulating scientific curiosity. Thank you to my undergrad professors, Dr. Raja Maunnamalai for always having time to discuss random chemistry insights, supporting the Alchemist club, and making

organic chemistry lab enjoyable, Dr. Soma Chattopadhyay for being a great professor and making physical chemistry my favorite course, Dr. Brian Barry for the extensive undergraduate research experience that provided me exceptional laboratory skills and synthetic mindset before graduate school. Finally, thank you to Dr. Jeffery Buboltz for your kindness and long conversations about the true purpose of science and learning, you have become a valuable role model in my life and I look forward to some more beers in Asheville with you.

Thank you to the support staff of Macromolecules Innovation Institute (MII) and the Department of Mechanical Engineering: Dr. Rituraj Borgohain, Patrick Finley, Lance Yelton, and Diana Israel for their aid in my research and making the campus socially cohesive and collaborative research environment for interdisciplinary research to take place. As well as all of MII fellow researchers and friends for the memorable experiences along the way, with special thanks to Michelle Pomatto, Garrett Godshall, Glenn Spiering, Dr. Clay Arrington, Dr. Lindsey Mondschein, Dr. Rayn Mondschein, Dr. Phil Scott, Julia Goyer, Morgan Wilson, and Andrew Willson. A special thanks to Dr. Chris Kasprzak, Dr. Brad Sutliff (and Deb), for being a great cohort and incredibly supportive life-long friends.

Lastly, I would like to acknowledge I would like all of my fellow researchers in the DREAMS Lab and Long Group for their academic support, and for aiding in my professional development through group meetings, random conversations, and great social events of lab lunch and competitive Halloween costume contests. Finally, thank you to Dr. Viswanath Meenakshisundaram for being a fantastic mentor, friend, roommate, and owner of Mani throughout this journey.

Contents

List of Figures

List of Tables

Chapter 1

Introduction

Vat Photopolymerization (VP) is a high-resolution additive manufacturing (AM) process in which ultraviolet (UV) light selectively irradiates photosensitive resin in a layer-by-layer fashion. The process begins by positioning the build stage in the vat where it is covered by one layer thickness (50-100 μm) of resin. This layer is selectively irradiated by UV light, causing the exposed regions to undergo a free radical polymerization/crosslinking reaction, converting the liquid resin into a solid part, a process referred to as curing. This first layer adheres to the build stage through the duration of the print. In top-down VP, the build stage descends one layer thickness lower into the vat to allow the liquid resin to recoat the previous layer. This new layer is exposed, fusing it to the previous layer. This process is repeated until the part(s) is complete. VP printers used in this dissertation utilize either a UV mercury bulb or UV LED as their energy source, a process called projection VP. Projection-based VP printers' high level of selectivity is enabled through the use of a digital mask, typically a digital micromirror device (DMD) or liquid crystal display (LCD). These masks modulate which pixels are on or off, thus defining which voxel will be cured within the vat. The schematic diagram of a top-down mask projection VP printer is displayed in Figure 1.1.

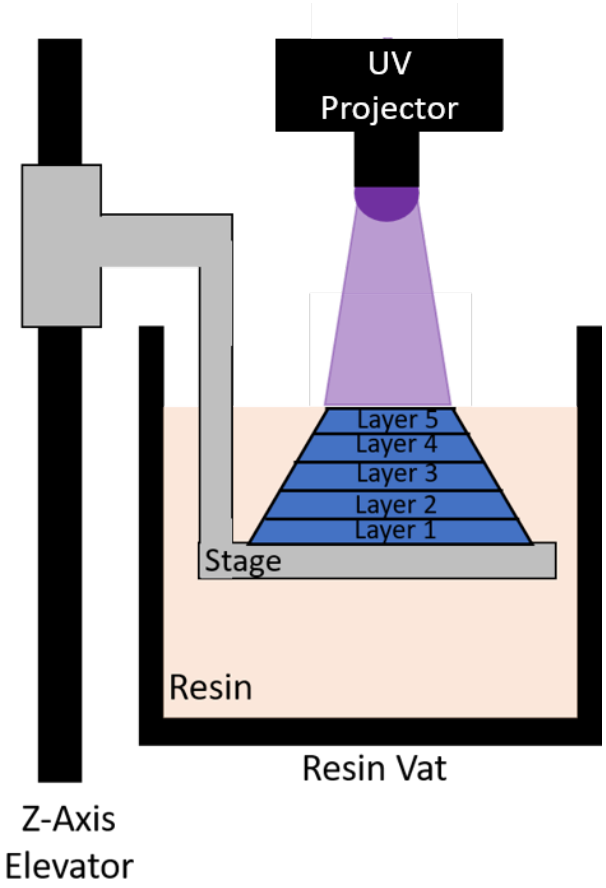

Figure 1.1: Schematic diagram of common VP embodiment of Mask Projection VP system.

Once the light reaches the resin surface, the photons collide with photoinitiators causing photolysis and producing two free radicals. The free radicals react with photocurable groups, such as acrylic, vinyl, or thiol-based monomers or oligomers, initiating polymerization. The radical is transferred to the front of the chain and propagation of the polymer continues.

In order for a material to be printable in VP, a crosslinking mechanism is needed. Traditionally, the photocurable monomers are difunctional, enabling linear polymer chains to crosslink together forming a solid part. Other approaches include physical crosslinks such as pendent ionic groups or hydrogen bonding. Many VP resin systems exhibit high crosslink density, resulting in brittle behavior. Additives, fillers, and other polymers are added into

resins to influence the final part properties. When the resin contains other non-photoreactive species, the photocurable network is referred to as the scaffold.

VP has found commercial applications in rapid prototyping, rapid tooling (e.g., thermoforming molds, and sacrificial patterns for investment and lost wax casting), and the manufacture of consumer products. While these applications leverage the high resolution of VP, the parts used are either sacrificial tooling or non-load-bearing components due to the poor mechanical and thermal properties of current materials produced with VP.

Acquiring high-performance properties in polymers has been achieved through crosslinking an acrylate network around a non-photocurable polymer within a solvent. The resulting part is a solvent-laden gel, which is then thermally post-processed to remove the solvent and/or the scaffold which allows the desired properties to be obtained. Gel-based printing has enabled the fabrication of multiple high-performance materials such as polyimides[1] and elastomers[2, 3]. However, these gel-based printing methods have tradeoffs that hinder processability. Polyimide resins rely upon a bonded scaffold, which is difficult to remove from the final part. This dissertation focuses on improving these tradeoffs by investigating a novel non-bound scaffold architecture to improve scaffold burnout in photocurable polyimide resins (Research Gap 1.1.1)

High-performance properties can also be acquired by filling the resin with particles to produce nanocomposites[4], ceramic[5], and elastomeric[2, 3] parts. Particle-filled resins suffer from reduced resolution due to light scattering of the filler reducing the resolution of the printer. This dissertation focuses on the development of a light scattering simulation to predict the photocuring behavior and cured shape of particle-filled resins (Research Gap 1.1.2).

1.1 Research Gaps

1.1.1 Gap 1: Limited investigation on polysalt scaffold architecture

Aromatic polyimides are a class of performance polymers that exhibit high thermal stability due to their rigid backbone. Polyimides are made photocurable and printable by dissolving polyimide precursor polymers functionalized with photopolymerizable moieties. Unfortunately, these polyimide precursors are difficult to process using VP due to the high resin viscosity at low loadings (15 wt%)[6]. While printable at these viscosities, the high solvent content causes high shrinkage (53%).

Recently a polysalt method was developed that leveraged polyimide dianhydride monomers covalently bonded with acrylates, creating acid-acrylate functionality[1]. When co-dissolved with diamine monomers, the acid and amine groups react to form an ammonium-carboxylate salt, creating a photocurable salt-bridged polymer, or polysalt. The polysalt platform decouples the viscosity and molecular weight relationship through the supramolecular monomer salts[1]. The polysalt resin exhibits low viscosity (1 Pa·s) even at high solids loadings (50 wt%), as the resin is comprised of small molecules. Upon thermal processing, the solvent evaporates and the monomers polymerize and subsequently imidize resulting in linear shrinkage of only 26%.

The polysalt, and all previous VP polyimide printing methods, currently rely on a covalent or ionic photocurable scaffold bound to the polyimide monomer/backbone. This scaffold architecture has demonstrated limited success in being removed from the printed parts during post-processing, with most methods only removing 25%[1] or less[7, 8, 9, 10, 11]. This is due to the use of scaffolds that char and do not volatilize at the post-processing

temperatures.

In this work, the author explores an extension of the polysalt approach wherein a non-bound scaffold is co-dissolved with the polyimide monomers. Unbound scaffolds allow the formation of a crosslinked network without the influence of the polysalt monomers while exhibiting thermal degradation behavior which closely mimics that of a neat scaffold sample. The author hypothesizes that using an unbound scaffold will facilitate more efficient scaffold burnout and less scaffold remaining within the final part. Additionally, not having a scaffold attached to the monomer opens the site, typically the anhydride monomer, to new chemical functionalities to tune the polymerization and imidization reaction.

This dissertation presents an investigation of using a non-bound triethylene glycol dimethacrylate (TEGDMA) scaffold within a 4,4'-oxydiphthalic anhydride and 4,4-oxydianiline (ODPA-ODA) polysalt resin. Two different monomer compositions are studied, half-ester and tetra-acid, to determine the impact of the scaffold and monomer composition on photocuring, post-processing, morphology, and resulting thermomechanical properties.

1.1.2 Gap 2: Limited resolution of particle-filled VP resins

VP resins filled with particles provide access to mechanical and functional properties that traditional resins are unable to achieve. Most notably the fabrication of printed ceramic parts[12, 13, 14, 15, 16], composite parts[4, 17], and latex-based resins[2, 3]. However, the dispersed particles cause an adverse effect of light scattering, which redistributes the light energy within the vat. This reduces cure depth and increases cure width, thus reducing the printing resolution[18], as displayed schematically in Figure 1.2. This creates a trade-off between material properties and spatial resolution. The trade-off worsens as the filler loading, particle size, and/or refractive index difference increases. Commercial resin manufacturers tend to minimize these factors by using ceramics with low refractive indexes, such as silica[5]

and alumina[19]. Still, higher refractive materials have yet to reach the commercial market due to light scattering.

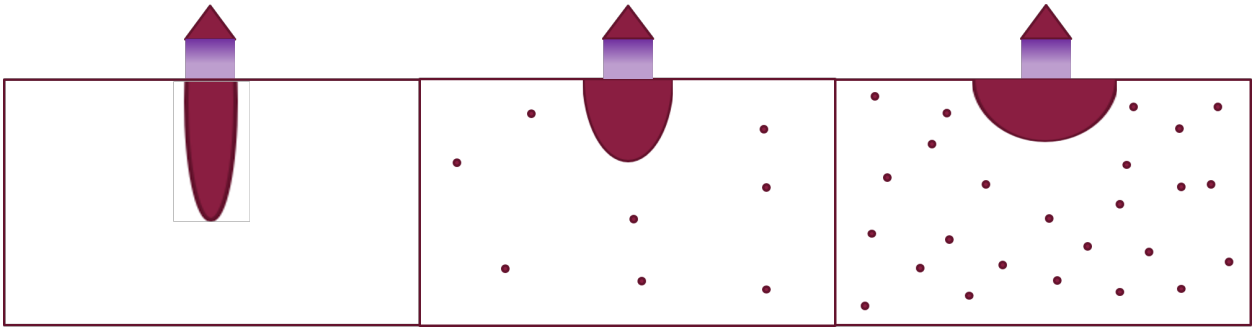

Figure 1.2: Schematic diagram of layers becoming shallower and wider as particle volume loading of the resin increases, which increases UV scattering in the vat.

Prediction of the scattering behavior allows for the redistributed energy to be corrected and parts to be printed at higher resolution. Over the past 30 years, numerous models have been proposed to describe the scattering and absorption of filled systems. Three types of approaches have been attempted: computer vision corrections[2], empirical relationships[18, 20, 21, 22, 23], and simulations[24, 25]. However, all of the proposed models require either the fabrication of filled resins to produce an empirical model or require difficult experiments to determine specific optical properties of the resin. This dissertation demonstrates a Monte Carlo ray-tracing (MCRT) simulation that utilizes intrinsic resin properties to predict the scattering behavior and the resultant photocuring behavior to predict the cured shape of a given layer.

1.2 Research Goals and Roadmap

The comprehensive research goal of this dissertation is to enhance VP's ability to print high-performance materials. In order to accomplish this, the aforementioned research gaps are addressed by *(1) Developing and investigating a modular polysalt approach that leverages a nonbound scaffold and (2) Developing a ray tracing simulation to*

predict light scattering and photocuring behavior of particle-filled resins. To this end, Research Objective 1 investigates the impact of monomer composition and scaffold architecture on photocuring, thermal post-processing, morphology, and thermomechanical properties. Research Objectives 2 and 3 investigate the feasibility of a ray-tracing-based simulation to predict the layer shape of scattering resins. The research questions driving the synthesis of new VP resins and modeling efforts are presented in Sections 1.2.1-1.2.3.

1.2.1 Research Objective 1

To address the limited material and material properties accessible as VP resins, the author presents a novel method of printing polyimide polysalt resin using a non-bonded scaffold architecture in a 4,4'-oxydiphthalic anhydride and 4,4-oxydianiline (ODPA-ODA) resins. Previous printing attempts of polyimides require a dedicated photocurable scaffold covalently attached to the polyimide backbone. The scaffold requires a dedicated synthetic step and is difficult to remove due to the increased thermal stability of the connected polyimide.

With the discovery of polysalt resins, the scaffold is no longer required to be connected to achieve sufficient modulus during printing. Without the covalent scaffold, monomer composition is able to be altered from either an acid or half-ester monomer composition. This enables the investigation of the scaffold architecture and monomer composition and the impacts on photocuring, polymerization, imidization, and the resulting final part properties. The research objectives of this investigation are shown in Table 1.1.

Table 1.1: Research Objective (RO) 1 and its developmental objective (DO) and driving research questions (RQ).

RO1	**Investigate the influence of scaffold architecture and monomer composition in polysalt-polyimide resins (Chapter 2)**
RQ1.1	How does incorporating a non-bonded scaffold influence photocuring and the printing of complex parts?
RQ1.2	How does a scaffold with low thermal stability affect burnout and thermal properties?
RQ1.3	How is morphology affected during the imidization protocol?

In Chapter 2, the printing of a polyimide polysalt resin using a non-bonded crosslinker and monomer composition is explored. Properties of geometric fidelity during post-processing, thermal stability, morphology, and thermomechanical behavior are examined. The material platform developed offers increased modularity and faster resin formulation time for the further development of a wider variety of polysalt resins.

1.2.2 Research Objective 2

To address the larger scattering seen in high-refractive ceramics used to print nanocomposites, the authors present a Monte Carlo ray-tracing simulation that simulates the scattering and absorption from the matrix and particles to produce the layer shape. This model requires only simple material parameters to perform the simulation and without ever needing to fabricate the filled resin of interest. Unlike previous models that require analytical descriptions, this simulation operates upon purely numerical data to enable the use of any particle size distribution and light source distribution, which is desirable for DLP projectors that do not exhibit a Gaussian distribution.

Validation of this simulation was performed by comparing the simulated and experi-

mental results of photocurable ZnO-filled resins. The research questions driving this research objective are shown in Table 1.2

Table 1.2: Research Objective (RO) 2 and its developmental objective (DO) and driving research question (RQ).

RO2	**Model and predict cure profile shape of ceramic filled resins using Monte Carlo ray-tracing simulation (Chapter 3)**
DO2	Develop a Monte Carlo ray-tracing simulation to model the light scattering behavior of photocurable resins containing polydisperse particles and volume-dependent light scattering.
RQ2	What is the accuracy of the MCRT simulation when photocuring of ZnO-filled resins?

In Chapter 3, difficulties in photocuring light scattering resins are presented in detail with the mathematical logic of the MCRT simulation. The simulation improves upon previous attempts to simulate MCRT simulation of particle-filled resins for VP through the incorporation of dependent light scattering, polydisperse particles, and using the neat resin working curve to define the photocured region. Validation of the simulation is achieved through the comparison of simulated and experimentally printed working curves of a zinc oxide suspension.

1.2.3 Research Objective 3

To address light-scattering latex-based resins, the authors present the Monte Carlo ray-tracing simulation to predict the photocuring behavior of an SBR latex resin. A resin that has been used to produce highly elastic 3D printed parts[2, 3]. The SBR, and latex resins in general, provide a unique condition to model compared to ceramics. Unlike ceramics, latex particles are typically amorphous and homogenous for all particle sizes, a common assump-

tion required for most Mie theory-based models. Latexes also maintain colloidal stability at high loadings, providing a useful case study for the simulation predicting concentration colloids. The research questions driving this research objective are shown in Table 1.3.

Table 1.3: Research Objective (RO) 3 and driving research question (RQ).

RO3	**Model and predict photocuring in light scattering resins (Chapter 4)**
RQ3.1	What is the accuracy of the MCRT simulation when photocuring of latex-based resins?

In Chapter 4, the MCRT simulation is used to predict the light scattering and photocuring behavior of SBR-latex resins of varying SBR concentrations. The simulation is compared to experimental trials of the same composition. This is the first investigation of predicting the photocuring behavior of latex-based resins in VP through a non-empirical method.

In Chapter 5, the summary and contributions of each research chapter are presented along with the assumptions, limitations, and potential future work for each objective.

Chapter 2

Vat Photopolymerization of Supramolecular ODPA-ODA Polyimide Salts using Unbound Scaffolds

Keyton Feller[1,2], Michelle Pomatto[2,3], Yiqun Fu [1,2], Yifeng Lin[1,2], Garrett Godshall[2,3] Clay Arrington[4] Timothy E. Long[4] and Christopher B. Williams[1,2].

[1] Department of Mechanical Engineering at Virginia Tech.

[2] Macromolecules Innovation Institute at Virginia Tech.

[3] Department of Chemistry at Virginia Tech.

[4] School of Molecular Science and Biodesign Center for Sustainable Macromolecular Materials and Manufacturing at Arizona State University.

Abstract

Additive manufacturing of UV-curable polyimides has relied on the photo-crosslinking of an acrylate scaffold bound to a high molecular weight polyamic acid precursor. Thermal post-processing pyrolyzes the scaffold and converts the polyamic acid into polyimide. This reliance on polymer precursors has hindered processing due to high resin viscosity and the limited solubility of the precursor. Recently, a supramolecular salt approach (deemed "polysalt") demonstrated vat photopolymerization (VP) of a low-viscosity precursor resin using a covalent-bound scaffold that resulted in a fully aromatic polyimide following post-processing. The use of a bound scaffold limits scaffold pyrolysis and results in a large fraction of the scaffold remaining in the final part.

In order to increase scaffold burnout and impart better final properties, this work uses an unbound scaffold (triethylene glycol dimethacrylate: TEGDMA) co-disolved with 4,4'-oxydiphthalic anhydride and 4,4-oxydianiline (ODPA-ODA) polysalt monomers. The dianhydride is converted to tetra-acid or half-ester monomers via one-pot synthetic routes.

Complex and solid parts are printed via vat photopolymerization and able to be thermally post-processed to remove 97% of the scaffold, resulting in linear shrinkage of 28-32%. A globular phase-separated morphology appears within printed solid geometries but does not occur within the latticed half-ester parts. Additionally, the half-ester undergoes thermal decomposition above 300 ^{o}C, leaving char within the parts and increasing the T_g by 80 ^{o}C. This platform and scaffold architecture enables a modular approach in which any acid-amine precursor can be combined with an unbound scaffold to produce novel and easily customizable UV-curable polyimide or polyamide thus further expanding the VP material catalog.

Keywords: Vat Photopolymerization, Polyimide, Additive Manufacturing, 3D Printing

2.1 Introduction

Aromatic polyimides (PI) are high-performance polymers that exhibit high organic solvent resistance[26, 27], glass transition temperatures (T_g) in excess of 200 ^{o}C, and thermal degradation temperatures near or above 400 ^{o}C[26, 27]. Polyimides also exhibit low dielectric constants[28, 29, 30, 31, 32, 33] and low coefficients of thermal expansion[28]. These superior properties also cause aromatic polyimides to be difficult to process through traditional means. The rigid backbone of polyimdes leads to high melt viscosities and limited solubility in most organic solvents, hindering melt and solution-based processing[34]. Due to these difficulties, polyimides are typically processed in their preimidized, polyamic acid (PAA) state, which offers increased solubility in polar aprotic solvents; the solution is then typically coated onto a substrate and subsequently thermally or chemically imidized.

For selective high-resolution patterning, PAA is functionalized with acrylate moieties (deemed "scaffold"), becoming photocurable and able to be selectively crosslinked using patterned UV light to form the shape of the part. Once photocured, the PAA is imidized and the crosslinker is either left within the part, or taken to elevated temperatures for degradation and removal. This approach is utilized within lithography and has recently expanded to UV-based additive manufacturing processes, including UV-assisted-direct ink write (UV-DIW) and vat photopolymerization (VP).

Previous work has demonstrated VP of pyromellitic dianhydride and 4,4'-oxydianililine (PMDA-ODA) through a multi-step synthesis to covalently functionalize PAA with acrylates, deemed poly(amic diacrylate esters) (PADE)[6]. The PADE approach produced complex parts via VP, but due to the high molecular weight PADE, the resin required near 85 wt%

solvent to achieve a printable viscosity. The high solvent content also resulted in 50% linear shrinkage following post-processing. Herzberger et. al simplified the PADE synthesis through the use of an acid-base reaction between the PAA and the acrylate to form a pendant salt acrylate. The PAA pendent salts, like PADE, were high molecular weight precursors and suffered from low solubility (15 wt% solids), which resulted in similar shrinkage (48%). The resulting resin also exhibited higher viscosity (15 Pa·s) caused by the charged backbone and acrylates[9].

The high viscosity of high molecular weight PAA solutions afforded processing via UV-DIW. High extrusion pressure and shear thinning behavior of the resin enabled higher solids loading (17%) and reduces shrinkage (40%)[35]. Printed parts exhibited identical thermal stability compared to commercial polyimides. Guo et. al incorporated an aliphatic trifunctional crosslinker into PMDA-ODA PAA resins and reduced linear shrinkage to only 20% and demonstrated final parts with thermal stability up to 400 ^{o}C, despite the addition of the crosslinker[8]. However, the addition of the crosslinker does result in a T_g below 250 ^{o}C. Other UV-DIW approaches using a fully aromatic poly(amide imide) displayed exhibited a printable viscosity at solids loading of 50 wt% and linear shrinkage of only 26%[36]. Similar to previous efforts, T_g suppression was observed due to the remaining photocurable scaffold after post-processing.

Approaches using low molecular weight fluorinated PAA exhibit increased solubility[10] in reactive diluents and thus have achieved solids loading of approximately 50 wt% [7, 11]. These methods enable VP of high-resolution features and linear shrinkage below 6%. However, the low shrinkage contributed to the low temperature of post-processing, which failed to pyrolyze the crosslinked scaffold. The remaining scaffold results in final parts with reduced thermal stability and caused thermal degradation to occur at $\leq$300 ^{o}C.

Recently, Arrington et. al demonstrated the printing of PMDA-ODA and 4,4'-(4,4'-

isopropylidene-diphenoxy)diphthalic anhydride-meta phenylene diamine (BPADA-mPD) through a supramolecular salt (polysalt) approach.[1] The polysalt platform is formulated by covalently functionalizing a dianhydride monomer with acrylates, forming a photocurable half-ester. When the half-ester acrylate is dissolved with the diamine monomer, an acid-base reaction occurs and the monomers form salts that result in a supramolecular polymer during a thermal post-process. Due to the use of small molecules, high concentrations of the precursor (50 wt% solids) are accessible at resin viscosity of only 1 Pa·s. This high loading results in linear shrinkage of only 26% and thermal stability of final parts up to 400 ^{o}C.

All of these previous polyimide printing approaches utilize ionic or covalent-bound scaffolds. There is currently no work investigating the impact of scaffold architecture in UV printing of polyimides. Fortunately, the introduction of the polysalt method enables the use of traditional non-bound multifunctional crosslinkers to print polyimides similar to other hydrogel/organogel-based resins[2, 37, 38, 39]. Decoupling the scaffold from the monomer also affords the facile study of polysalt compositional differences.

This work investigates the effect of a non-bound triethyleneglycol dimethyacrylate (TEGDMA) scaffold in 4,4'-oxydiphthalic anhydride and 4,4'- oxydianiline (ODPA-ODA) polysalt resins. The TEGDMA scaffold exhibits low thermal stability and low char yield in the neat state, which is hypothesized to increase scaffold burnout and reduced char in the final part. Additionally, without the synthetic step of attaching the scaffold to the precursor monomers, this approach creates a modular platform for easily printing a variety of monomers. Using TEGDMA as a scaffold, and other scaffolds like it, enables polyimide parts to be fabricated with properties that are not influenced by the scaffold and open up a wider variety of printable polyimides with the need to develop novel synthetic strategies.

Tetra-acid and half-ester versions of ODPA are used to investigate the impact of reduced polarity within polysalt resin post-processing, and as a case study to demonstrate the

modularity of the platform. The goal of this work is to determine how both the scaffold and monomer compositions affect the resin photocuring rate and resulting modulus to fabricate solid and complex parts, and evaluate the impact of the imidization protocol on final part morphology, and thermomechanical properties.

2.2 Experimental Procedure

2.2.1 Polysalt Resin Formulation

4,4'-Oxydiphthalic anhydride (ODPA) and 4,4'-oxydianiline (ODA), and crosslinker triethyleneglycol dimethyacrylate (TEGDMA) were purchased from TCI and used as received. A photoinitiator, diphenyl(2,4,6- trimethylbenzoyl) phosphine oxide (TPO), was purchased from Millipore Sigma.

Dimethyl sulfoxide (DMSO) was used for the polysalt solvent and was purchased from Oakwood Chemical. Resins were formulated in one-pot at 50 wt% total solids (ODPA, ODA, TEGDMA) loading. Specifically, for 70 g of resin, 11.92 g of ODPA is placed in a flask with 35 g of DMSO and is reacted at 50 ^{o}C for an hour with either 1.38 g of DI water to form the tetracarboxylic (ODPAC) or 3.54 g of ethanol to form the ethyl half-ester (ODPAE). Once dissolved and cooled, 7.695 g of ODA and 0.875 g (2.5 wt% of solids) of TPO is added to the solution and allowed to dissolve at ambient conditions for 2 hours while stirring. Once all components are dissolved, 14.0 g of TEGDMA is added and the resin is ready to be photocured. The synthesis scheme is described in Scheme 2.1, which outlines the modularity of the polysalt platform enabling the use of any acid and amine-functionalized precursors to be combined with an unbound scaffold.

Scheme 2.1 Synthesis of ODPA-ODA polyimide polysalt resins through tetra-acid ODPAC-ODA (left) and half-ester ODPAE-ODA (right) templates.

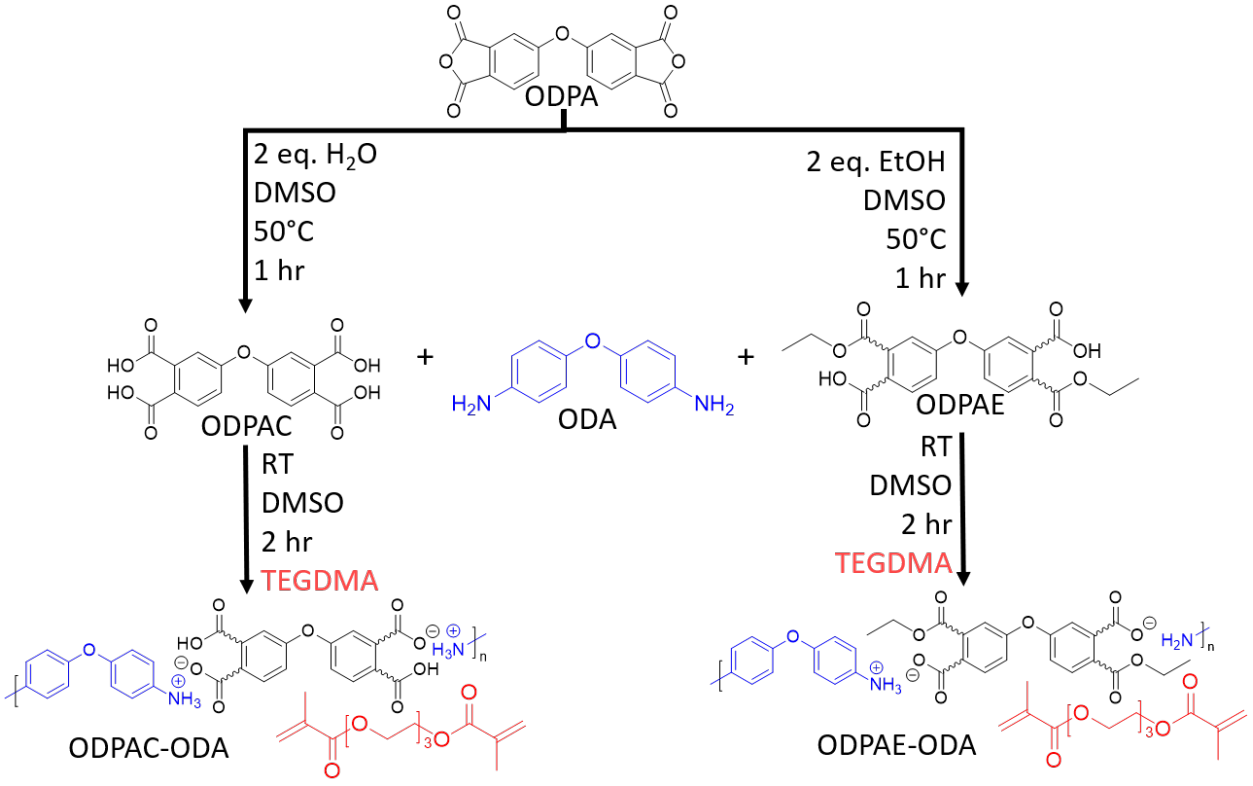

2.2.2 Resin Characterization

Synthesis of ODPAC and ODPAE were determined by H^1 NMR using a 400 MHz Agilent U4-DD2 in DMSO-d6.

Photorheology was performed using a TA Instruments Discovery HR-30 with 20 mm parallel plate geometry, UV curing accessory, and Omicure S200 light source with an emission bandwidth of 320-500 nm. A 400 nm high pass filter was used to block light below 400 nm. The emitted light was calibrated to an intensity of 42 mW/cm^2 with a Dymax Accucal-160 LED radiometer to best mimic the VP printer's UV light source. Oscillatory experiments were performed at a frequency of 1 Hz, strain amplitude of 0.1%, and gap thickness of 100 μm. Polysalt resins oscillated for 30 s to equilibrate and were then irradiated for 90 s. The

gel-time, or crossover time, of the resin is identified as the exposure time required for the storage modulus and loss modulus to become equal.

2.2.3 Vat Photopolymerization & Post Processing

Parts were fabricated on a custom-built top-down VP printer equipped with a 405 nm UV-LED Wintech Digital PRO4710-1080p compact optical engine. The maximum intensity of the projector is 42 mW/cm^2, with a pixel size of 35.5 μm and layer thickness of 100 μm. The ODPAC-ODA resin was exposed for 8 seconds/layer (exposure=336 mJ/cm^2) and the ODPAE-ODA resin was exposed for 12 seconds/layer (exposure=504 mJ/cm^2). Exposure times were empirically determined using photorheology crossover times as an initial value, with small increases in exposure, via trial and error, to successfully print complex lattice parts.

Printed parts are left in ambient air to dry until they are no longer tacky (approximately 4-7 days, depending on geometry). The parts are then placed in an MTI GSL 1600X tube furnace with N_2 environment. The tube furnace is heated at 0.5 ^{o}C/min with isotherms at 60 ^{o}C for 10 hours, and 100, 150, 200, 250, 300, 350, and 400 ^{o}C for 2 hours each. Thermal post-processing conditions were modified from Zhang et al.[40], which produced ODPA-ODA films. The isotherms are used to slowly remove the solvent, scaffold, and condensates from the part and minimize residual stress.

Samples "ODPAE-ODA-300C" and "ODPAC-ODA-300C" were prematurely stopped at 300^{o}C for analysis to investigate the progress of scaffold removal and part property development. "Control" polysalt samples that neither contained TEGDMA nor TPO were subjected to the same thermal post-processing and stopped at 300 and 400 ^{o}C to enable comparison against printed samples and isolate processing effects caused by the TEGDMA scaffold.

2.2.4 Part Characterization

Thermal stability of printed parts and control samples (i.e., no scaffold) were measured with thermogravimetric analysis (TA Discover 550) at 3 ^{o}C/min to 800 ^{o}C. Thermomechanical properties of the printed samples were determined with dynamic mechanical analysis (DMA) on a TA-Q800 DMA at 1 Hz, 0.1% strain up to 300 ^{o}C or 400 ^{o}C, depending on the maximum processing temperature of the sample. Imidized photocured discs were analyzed using Fourier transform infrared spectroscopy (Varian ATR) to verify that samples are imidized and to determine if residual scaffold is present. The morphology of printed sample cross-sections were analyzed on a JEOL IT-500HR field emission gun – scanning electron microscope (SEM). Density measurements were performed using an analytical balance density kit. Linear shrinkage was determined by taking dimensional measurements via a micrometer on printed cuboids following (i) printing, (ii) four days of air drying, (iii) 300 ^{o}C processing, and (iv) 400 ^{o}C processing. All characterization requiring solids parts used printed specimens, with the exception of FTIR, which used photorheology discs.

2.3 Results and Discussion

2.3.1 Synthesis of ODPA-ODA Polysalt Resins

Both the ODPAE and ODPAC were successfully synthesized and verified with NMR (Figure A.1-A.3), with the ODPAE exhibiting a combination of four different isomers. When resins are completely mixed, both were homogeneous and transparent with orange-yellow hues. The ODPAE-ODA resins appeared darker than ODPAC-ODA-based resins, potentially resulting from differences in the supramolecular salt structure. The darker color in the ODPAE-ODA resulted in the resin being more absorptive and requiring more UV exposure to cure. This is observed in photorheology, Figure 2.1, where a longer crossover time for

ODPAE-ODA (10 s) is observed compared to that of ODPAC-ODA (7 s). Both resins exhibited sufficient plateau modulus of $> 10^5$ Pa and very low uncured viscosities, below 0.1 Pa·s at 50 wt% solids (Figure A.4), for VP processing.

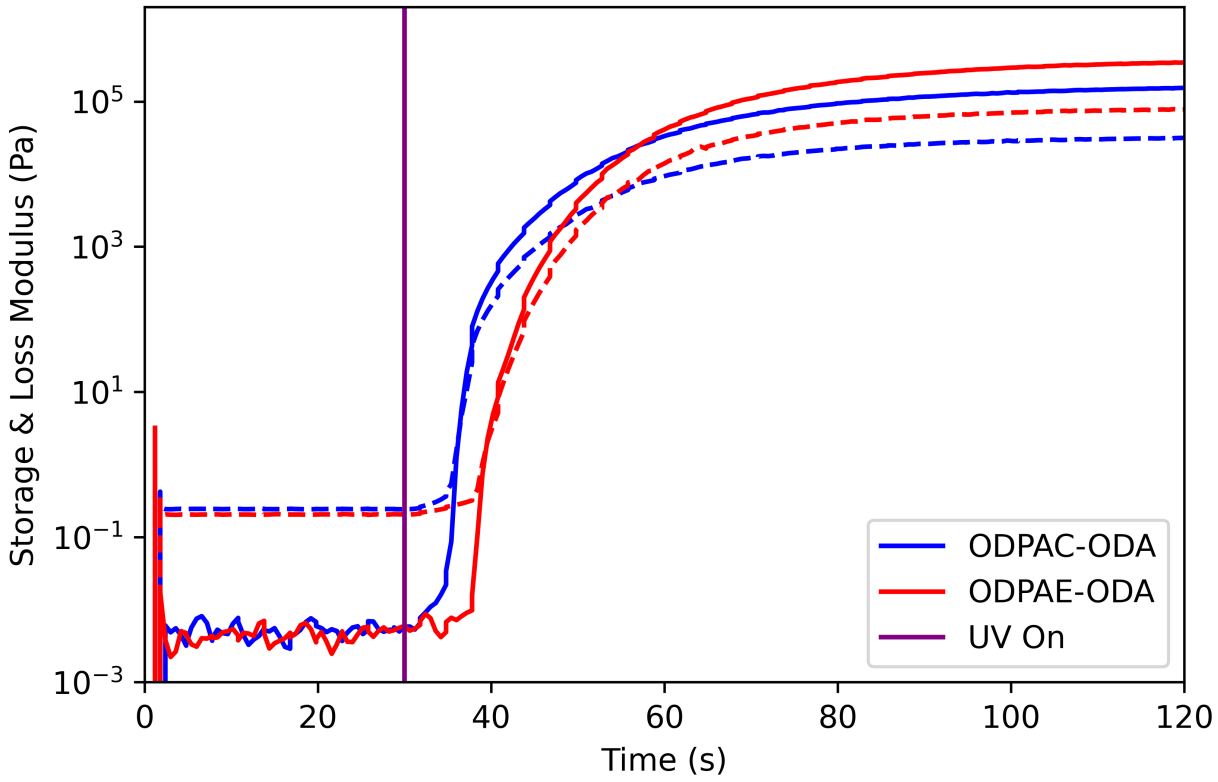

Figure 2.1: Photorheology curves of ODPAC-ODA and ODPAE-ODA resins at 50 wt% solids in DMSO at gap thickness of 100 μm. Storage and loss modulus are denoted with solid and dashed lines, respectively. The 42 mW/cm^2 UV light (400-500 nm) turns on at Time = 30s.

2.3.2 Vat Photopolymerization and Post Processing of Polysalt Resin

Complex latticed (Figure 2.2) and rectangular solid parts (Figure A.5) were printed with 100 μm layers and exposure dosages of 8 s (336 mJ/cm^2) for ODPAC-ODA and 12 s (504 mJ/cm^2) for ODPAE-ODA. Exposure dosages required for printing are higher than photorheology crossover times, potentially resulting from the resins experiencing higher ex-

posure due to reflected light from the aluminum top plate and reduced oxygen inhibition in the photorheology setup that reduces the resin's contact with air.

When printed, parts are transparent with an orange/tan hue; within approximately 12 hrs the parts become darker and opaque, as shown in Figure 2.2a and 2.2b. The printed lattices exhibit a more uniform hue. Thicker parts (>6 mm), as seen in Figure A.5, exhibited faster solvent removal on sharp edges than in the bulk of the part, which results in light edges. The opaqueness is attributed to phase separation and is discussed in greater detail in Section 2.3.3.

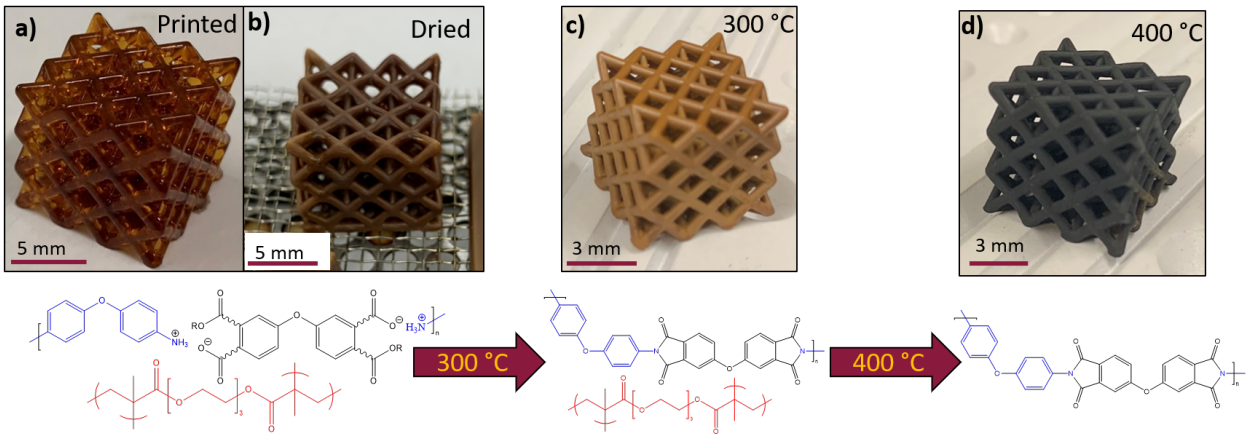

Figure 2.2: Post-processing of the ODPA-ODA parts to thermally imidize and remove the TEGDMA scaffold and the resulting chemical changes occurring through the process. Images display the visual changes of the part after being printed (a). Lattice parts are left to air dry for four days, removing solvent and causing the part to become opaque (b). Dried parts are processed to 300 ^{o}C for imidization (c) but require processing up to 400 ^{o}C to pyrolysis the scaffold(d).

Once dried, the parts are thermally imidized by slowly heating to 300 ^{o}C, displayed in Figure 2.2c. Both ODPAE-ODA and ODPAC-ODA parts become a brighter orange/tan hue, the typical color of conventionally processed polyimides. At this stage, the precursor polymer has reached its maximum imidization conversion with approximately 30 % of the scaffold remaining within the part, based upon TGA (Section 2.3.3). Upon heating to 400

^{o}C, the scaffold degrades and volatilizes, leaving the polyimide behind.

ODPAE-ODA latticed parts maintained geometric fidelity through all thermal post-processing, but ODPAC-ODA lattices were unable to retain the printed shape when processed to 400 ^{o}C. The authors hypothesize that the failure results from reduced mechanical strength, discussed in Section 2.3.5. Post-processing to 400 ^{o}C results in parts becoming black, as seen in Figure 2.2d. Darkening of printed polyimide parts is frequently observed and contributed to degraded scaffold char remaining in the part[1].

However, both control ODPAE-ODA and ODPAC-ODA polysalt solutions thermally processed to 400 ^{o}C without scaffold also exhibited a similar change of color. This indicates that the color change is not the result of the scaffold, but the result of the chemical composition of the polysalt structure and/or the thermal processing protocol. The cause of this darkening is further explained with TGA results (Section 2.3.3). Additionally, printed parts heated without sufficient air drying tended to warp and crack. This behavior is particularly noticeable with thin, film-like structures and ODPAC-ODA when processed to 400 ^{o}C.

During post-processing, both ODPAE-ODA and ODPAC-ODA exhibited similar isotropic shrinkage of approximately 23% linear shrinkage when heated to 300 ^{o}C. However, when heated to 400 ^{o}C, ODPAC-ODA-400C exhibited 28% linear shrinkage and ODPAE-ODA-400C with 32% linear shrinkage. The shrinkage values measured are greater than previous polyimide printing investigations using a poly(HEA) scaffold at these temperatures [1]. This is attributed to a larger fraction of the scaffold removed from the printed parts.

2.3.3 Characterization of Processed Printed Parts

Degradation

TGA in Figure 2.3a displays poly(TEGDMA) degradation as a two-step pathway, with the first being attributed to the volatilization of low order cycles degrading from the network formed during photopolymerization[41], which comprises near 70% of the total mass of the TEGDMA network. These cycles arise from flexible propagating TEGDMA chains to backbite forming low-order rings/cycles within the network. These cycles do not entangle and are not a structural component of the scaffold network. Upon thermal processing, these cycles degrade around 300 ^{o}C, with the rest of the network degrading above 300 ^{o}C. The degradation of the cycles are seen as the first degradation step for ODPAC-ODA-300C and ODPAE-ODA-300C in Figure 2.3a. Comparing the printed and control specimens, there is a 3% difference in char yield at 600 ^{o}C, indicating approximately 97% of the TEGDMA scaffold is removed during thermal post-processing.

An 8% difference in char yield is observed between ODPAC-ODA-400C and ODPAE-ODA-400C. This difference in char yield is also observed in the scaffold-free control specimens of ODPAC-ODA-400C and ODPAE-ODA-400C (Figure 2.3b). This indicates that the scaffold is not a contributing factor to the resulting char yield. The authors surmise this difference in char yield is the result of the ODPAE-ODA degrading between 300 and 400 ^{o}C, supported by the darkening of the parts in Figure 2.2c and 2.2d. The degradation of the ODPAE-ODA is believed to be caused by incomplete imidization, resulting in amide bonds, which thermally degrade and leave behind degraded byproducts. A potential cause for incomplete imidization is poorer solvent (DMSO) retention in ODPAE-ODA which limits the imide conversion.

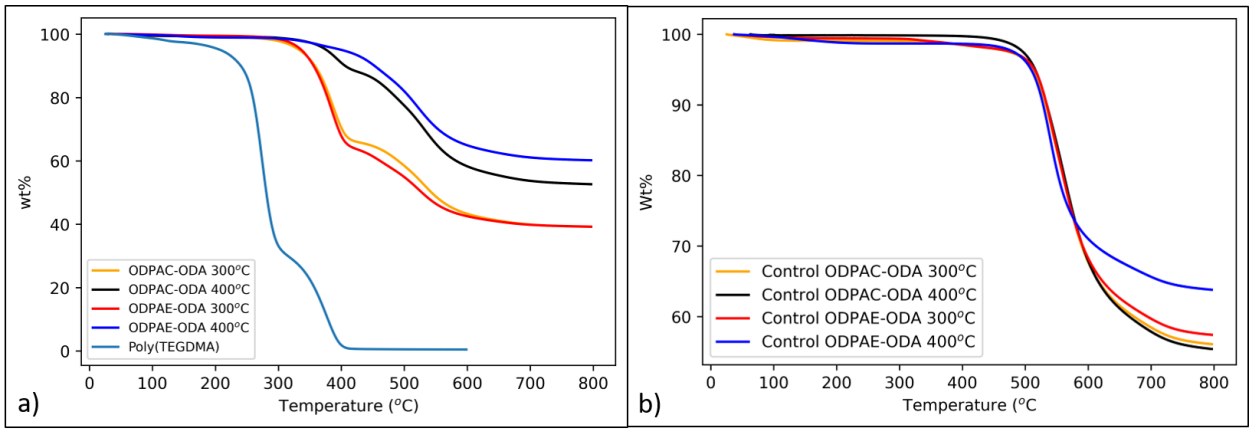

Figure 2.3: a) TGA of 3D printed parts and poly(TEGDMA) scaffold and b) control polysalt resin containing no TEGDMA.

Imidization Analysis

FTIR of all post-imidized samples (normalized to 1230 cm^{-1} peak) displayed in Figure 2.4, displays near complete imidization. This is indicated by the imide C-N-C peaks at 1370 cm^{-1} and 743 cm^{-1} and the imide carbonyl (C=O) peaks at 1780 cm^{-1} and 1709 cm^{-1}[42]. Other major peaks at 882, 1604, 1498, 1470, and 1435 are attributed to the phenyl (C-C & C=C) stretches and deformations, and peaks at 815 and 1230 cm^{-1} are attributed to the out-of-phase phenyl (C-H) deformations[42]. The aliphatic C-O ether linkage of the poly(TEGDMA) scaffold is observed at 1110, 960, and 840 cm^{-1} [43] across all samples, indicating a small amount of the scaffold does remain within the part.

The ODPAE-ODA-400C exhibits more noisy FTIR spectra, with many peaks broadening or nonexistent compared to other samples analyzed. This behavior is observed under polymer degradation and in carbon black polymer composites[44, 45], consistent with the TGA results presented in Section 2.3.3.

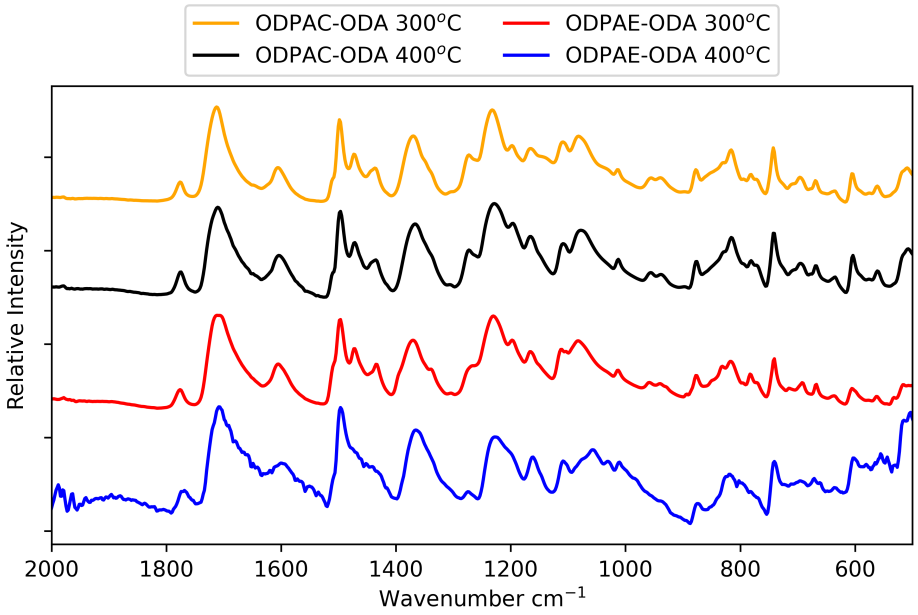

Figure 2.4: Plot of FTIR spectrum of printed imidized polysalt parts.

2.3.4 Structure/Morphology

Printed parts, processed to either 300 or 400 ^{o}C, exhibited a connected phase-separated globular morphology, as observed via SEM. ODPAC-ODA is shown in Figure 2.5; ODPAE-ODA is shown in Figure A.7. The globs are uniform in size, approximately 100 μm in diameter, with a random structure not affiliated with the printing layer size or location. No printing layers are observed in any part analyzed, consistent with other solvent-based polyimide printing approaches[1, 6, 9].

At further magnification, porosity is observed within ODPAE-ODA-300C and ODPAC-ODA-300C. Upon processing to 400 ^{o}C, the porosity appears to densify, while the globular structure remains. Therefore, the printed parts exhibited lower than bulk density (1.4 g/mL[46]), as seen in Table 2.1. The lower density of ODPAE-ODA-400C is attributed to the formation of lower-density char, or closed porosity within the parts.

Table 2.1: Density of post-processed printed ODPA-ODA specimens

Sample	Density (g/cm^3)
ODPAC-ODA-300C	1.20 ± 0.05
ODPAC-ODA-400C	1.21 ± 0.03
ODPAE-ODA-300C	1.27 ± 0.06
ODPAE-ODA-400C	1.08 ± 0.02

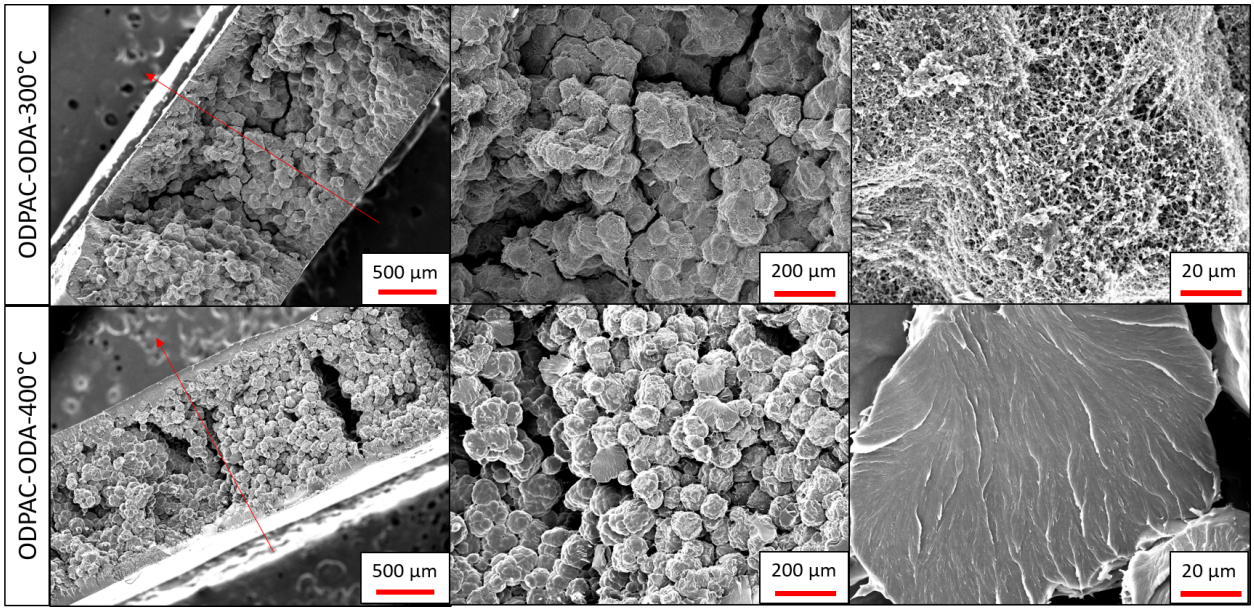

Figure 2.5: SEM of ODPAC-ODA-300 (top) and ODPAC-ODA-400 (bottom) fracture surface. Printed layers follow the shortest dimension, denoted by the red arrow in the left images.

The globular microstructure is also observed within the scaffold-free control samples when processed to 300 ^{o}C, as seen in Figure 2.6a and 2.6c. However, the control samples did not exhibit similar porosity. This leads the authors to hypothesize that the porosity seen in scaffold-containing parts is the result of the network cycles from the TEGDMA scaffold degrading and leaving pores. Once the cyclics are volatilized, the polyimide is still restricted by the remaining scaffold and unable to flow into the empty volume, which causes porosity. Processing to 400 ^{o}C, the scaffold degrades and allows the polyimide chains to consolidate the porosity, but the globular microstructure remains, as shown in Figure 2.6b and 2.6d.

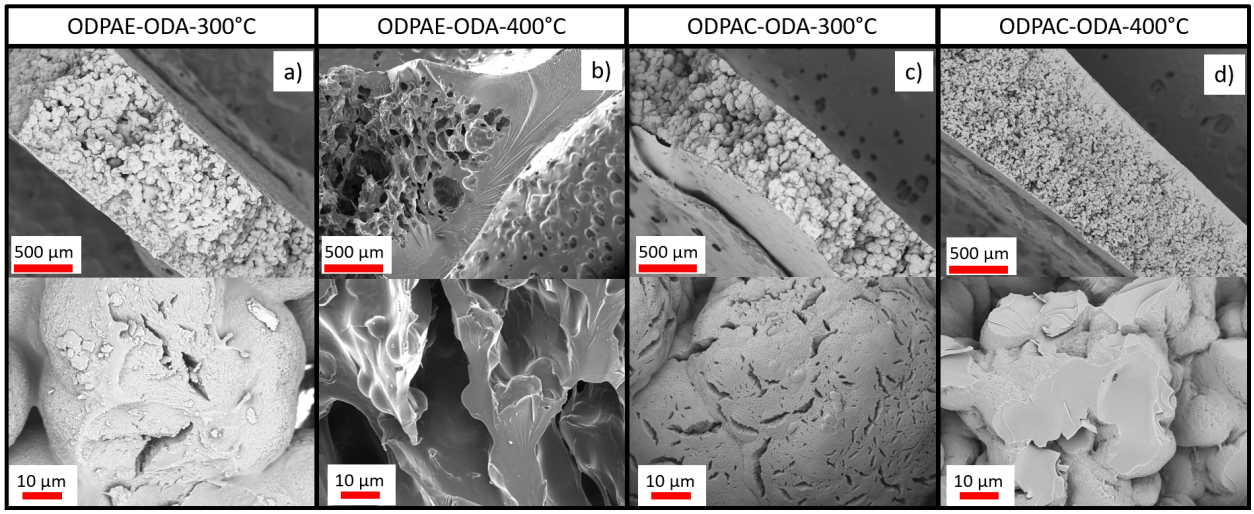

Figure 2.6: SEM of scaffold-free control samples of a)ODPAE-ODA-300C, b)ODPAE-ODA-400C, c)ODPAC-ODA-300C, and d)ODPAC-ODA-400C.

Unlike the scaffold-free control specimens and thicker printed specimens, SEM of the printed ODPAE-ODA lattices display homogeneous microstructure after processing at 300 (Figure 2.7a) and 400 ^{o}C (Figure 2.7b). The ODPAC-ODA lattice, exhibited similiar morphology as the thicker samples but the globular microstructure appears more platet-shaped but the porosity remains (Figure A.6). This may indicate that the tetra-acid has a higher affinity for the DMSO solvent and requires more time for the solvent to evaporate or to leave the part. Alternatively, the porosity may be the result of ODPAC, as it has been previously been used as a foaming agent in ODPA-ODA foams[47]. The foaming occurs from excess water being produced during both polymerization and imidization. However, it is currently unknown how the post-processing protocol enhances or mitigates the foaming process.

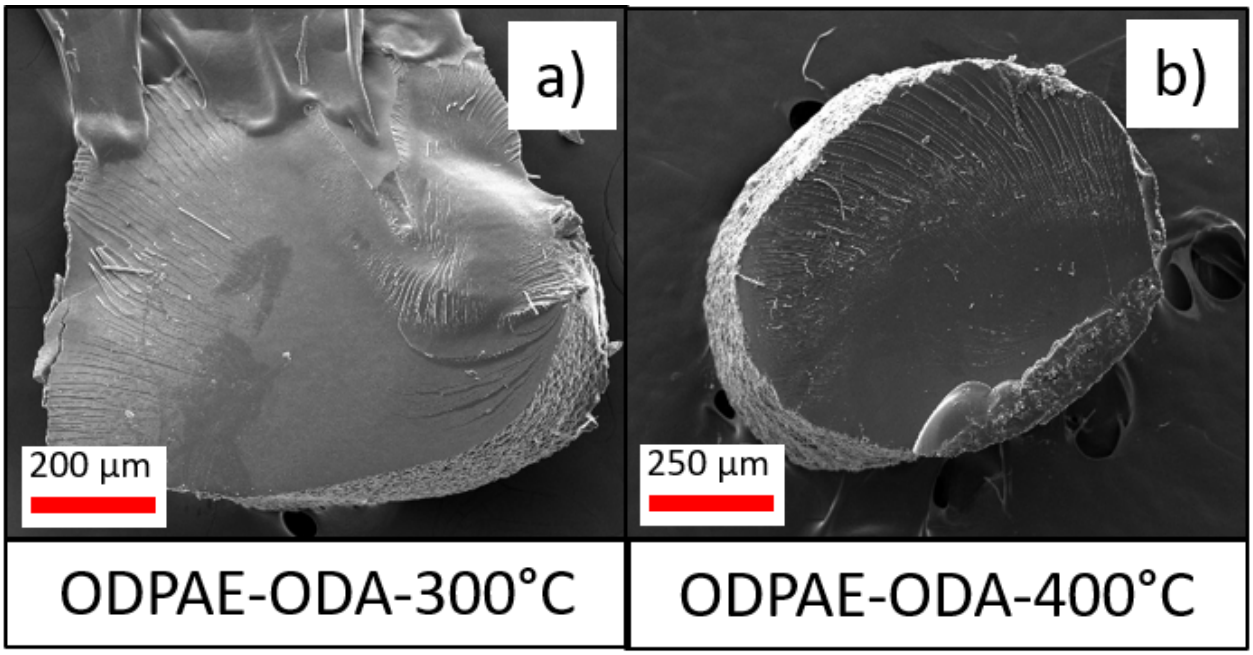

Figure 2.7: SEM of printed lattice strut cross-section of ODPAE-ODA-300C (left) and ODPAE-ODA-400C (right). Lattice parts exhibited homogeneous morphology at both processing temperatures.

2.3.5 Thermo-Mechanical Properites

DMA of ODPAC-ODA-300 and ODPAE-ODA-300 (Figure 2.8) displays near-identical thermo-mechanical curves, exhibiting peak tan(δ) T_gs of 260 ^{o}C and 257 ^{o}C, respectively. This agrees with literature values, which report T_g's between 250 ^{o}C and 260 ^{o}C[28, 48]. ODPAC-ODA-300 and ODPAE-ODA-300 also exhibit lower glassy moduli compared to the 1 GPa storage modulus observed in their respective 400 ^{o}C samples. The authors believe the differences in glassy moduli correspond to differences in specimen porosity, as observed in Figure 2.5 and A.7.

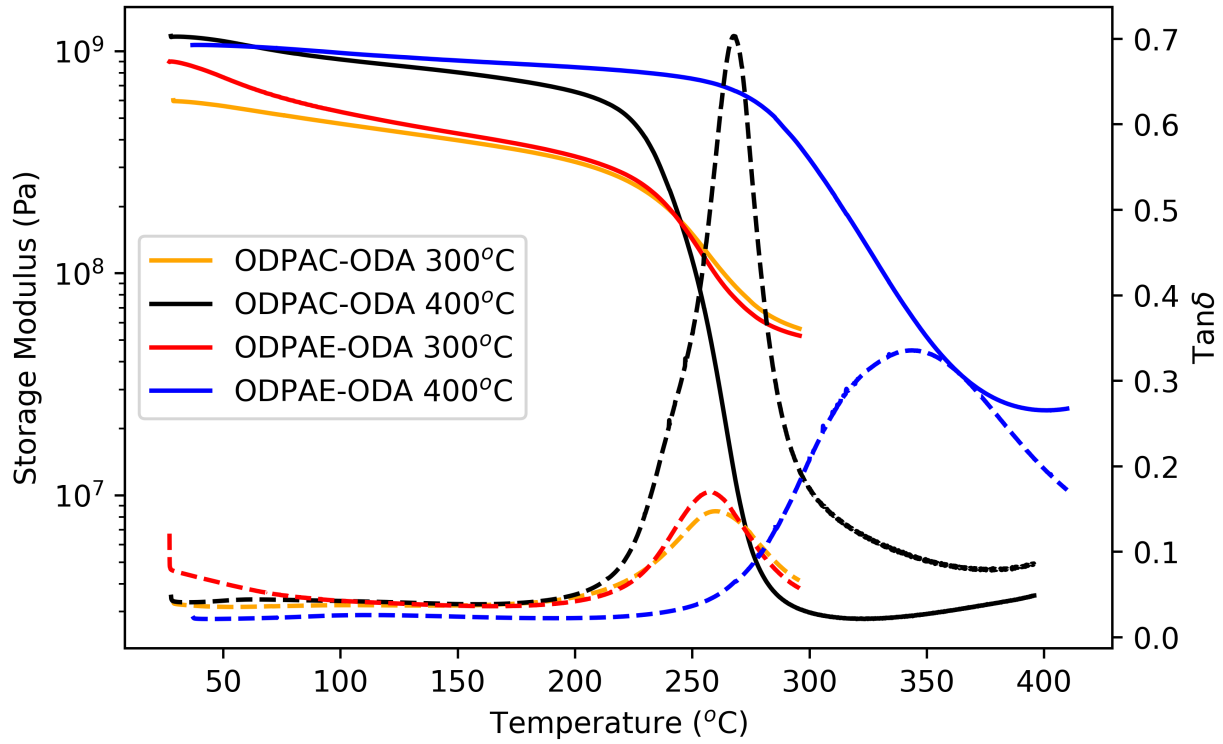

Figure 2.8: Dynamical mechanical analysis of printed specimens in an N_2 environment. Storage modulus is represented by solid lines and tan(δ) by dashed lines.

As seen in TGA (Figure 2.3), samples processed to 400 °C have a large majority of poly(TEGDMA) removed, resulting in a more thermoplastic-like behavior. This is demonstrated with ODPAC-ODA-400C, which exhibits a lower rubbery plateau and larger tan(δ) peak than ODPAC-ODA-300C. This larger storage modulus drop in ODPAC-ODA-400C is believed to contribute to the ODPAC-ODA lattice parts failing when processed to 400 °C, as flow is observed at elevated temperatures.

ODPAE-ODA-400C behaves differently, exhibiting a higher rubbery plateau, broader tan(δ), and T_g of 343 °C, approximately 80 °C higher than reported in literature[48]. Increases in T_g through thermal degradation have been observed through degradation of pendent groups[49]; however, the authors hypothesize the degradation may be the result of

non-imidized, amide species degrading above 300 ^{o}C and restricting chain mobility, thus increasing T_g.

The specific cause of higher degradation in ODPAE-ODA may result from a lower overall imidization conversion due to poorer solvent retention. The extra acid functionality in ODPAC-ODA allows for twice the hydrogen bonding donation, improving retention of DMSO at elevated temperatures, and aiding in greater imidization conversion[50, 51, 52]. The reduced imdization in ODPAE-ODA results in the presence of thermally unstable amide species, which degrade above 300 ^{o}C, and produce char within the polyimide. The char formed is molecularly mixed within the polyimide, causing a large effect on chain mobility, and is reflected in the higher T_g.

2.4 Conclusion

Photocurable ODPA-ODA polysalts enabled low-viscosity VP printing, which resulted in fully aromatic polyimide with limited shrinkage. The use of a non-associating scaffold (TEGDMA) enabled photocuring at reasonable time scales (8-12 s per layer, 336-504 mJ/cm^2) and printing of complex geometries across the tetra-acid and half-ester compositions. TGA shows that Approximately 97% of the TEGDMA scaffold was removed during thermal post-processing. Solid parts processed to 300 ^{o}C exhibit a complex phase-separated globular morphology with porosity due to the presence of the solvent. Upon processing to 400 ^{o}C, the porosity densifies and the globular morphology remains. The microstructure remains in the latticed tetra-acid parts but half-ester latticed parts appear fully homogenous at both 300 and 400 ^{o}C. Parts processed to 300 ^{o}C appear to reach maximum imidization conversion and exhibit T_g in agreement with literature values. When processed to 400 ^{o}C, the tetra-acid maintains its T_g, while the half-ester undergoes partial degradation, which increases the T_g by 80 ^{o}C.

This work demonstrates that the unbound scaffold has little impact on photocuring, imidization, morphology, or thermo-mechanical properties due to a large portion of the scaffold degrading and volatilizing from the part. The dominant factors determining the printed part properties result from the polysalt monomer composition and part geometry. This indicates the expected properties of a desired polysalt-compatible material can be determined without the need for printing or formulation of UV-curable resins. This platform demonstrates the potential to be generalizable to other polyimide systems to produce a wider variety of materials.

Future development of this platform includes investigating a wider variety of polyimides and other salt-compatible monomers such as polyamides to expand the modularity. This work has also been limited to linear polymers; however, crosslinking polymers using multifunctional monomers is also expected to be compatible. Part properties may also be refined through optimizations of the post-processing protocol to tune part morphology.

2.5 Acknowledgments

The authors thank the Virginia Tech Material Characterization Lab (MCL) and Moore Research Group (MoRG) for providing access to the DMA, Rheology, TGA, and DSC instruments. The authors also thank the Virginia Tech NCFL for access to the SEM. Additionally, the authors would like to acknowledge the Virginia Tech Chemistry Department for access to the NMR instrumentation.

Chapter 3

Simulation of Ceramic filled Vat Photopolymerization Resins Using Monte Carlo Ray-Tracing

Keyton Feller[1,2], J. Robert Mahan[1], Yiqun Fu [1,2], Nathan Raeker-Jordan[1], Timothy E. Long[3] and Christopher B. Williams[1,2].

[1] Department of Mechanical Engineering at Virginia Tech.

[2] Macromolecules Innovation Institute at Virginia Tech.

[3] School of Molecular Science and Biodesign Center for Sustainable Macromolecular Materials and Manufacturing at Arizona State University.

Abstract

Photocurable ceramic suspensions used in vat photopolymerization (VP) to produce composite and ceramic parts suffer from reduced resolution due to light scattering by the particles. When irradiated, the scattered light causes a redistribution of the UV intensity, resulting in a reduction in cure depth and an increase in cure width. To predict the resulting exposure distribution and cure profile shape of ceramic-loaded resins, the authors develop a Monte Carlo ray-tracing (MCRT) simulation to predict light scattering and absorption of UV energy in particle-filled resins. The simulation incorporates volume-dependent light scattering physics of polydisperse particle sizes to accurately represent the scattering behavior of filled resins. Additionally, the simulation uses only experimentally acquired parameters including refractive index, particle size distribution, the spatial intensity distribution of the light source, and critical exposure to cure to predict the photocured shape. With these parameters, the authors simulate cure profiles of a ZnO-filled polyester acrylate resin, which has a high refractive index of 2.2. Printed and simulated cure profiles are compared across varying ZnO loadings (1 to 5 vol%) to validate the simulation. The simulation demonstrates a high degree of accuracy in predicting experimental cure profile shape with all cure depth predictions within 10% (20 μm) and cure widths within 30% (15 μm).

Keywords: Vat Photopolymerization, Monte Carlo Ray-Tracing, Additive Manufacturing, 3D Printing, Light Scattering

3.1 Glossary

C_d	Cure Depth
D_p	Penetration Depth
E	Incident Exposure
E_c	Critical Curing (Depth) Exposure
W_{ex}	Excess Width
E_w	Critical Curing (Width) Exposure
$I(\theta)$	Scattering Intensity Distribution
μ_s	Scattering Coefficient
μ_a	Absorption Coefficient
Δs	Transport free path
$E_{c,0vol\%}$	Critical Exposure of Neat Resin
$P(\theta)$	Form Factor
$S_F(\theta)$	Structure Factor
$S_1(\theta)$	Perpendicular Scattering Amplitude
$S_2(\theta)$	Parallel Scattering Amplitude
a_n, b_n	Mie Coefficients
π_n, τ_n	Angular Scattering Patterns of the Spherical Harmonics
x	Size Parameter
m	Complex Refractive Index Ratio
n_m	Matrix Refractive Index
n_p	Particle Refractive Index
k_p	Particle Absorption Index
r	Particle Radius
λ	Wavelength
Q_s	Scattering Efficiency Factor
E_n	Energy of Ray

3.2 Introduction

3.2.1 VP of Ceramic Filled Resins

Vat photopolymerization (VP) is an additive manufacturing process that patterns UV light to selectively crosslink, or cure, a photosensitive resin in a layer-by-layer fashion. VP printers are classified as laser-based or projection-based according if the UV light is patterned by a rastering laser or dynamic mask, respectively. Both of these printer embodiments allow for high-resolution printing with layer heights typically between 50 and 100 μm and minimum feature size between 10 and 50 μm[53]. Figure 3.1 displays a schematic diagram of a projection-based VP printer used in this work. Despite the high-resolution printing, the material properties of the majority of VP resins are limited in mechanical performance due to the nature of photo-crosslinking chemistry.

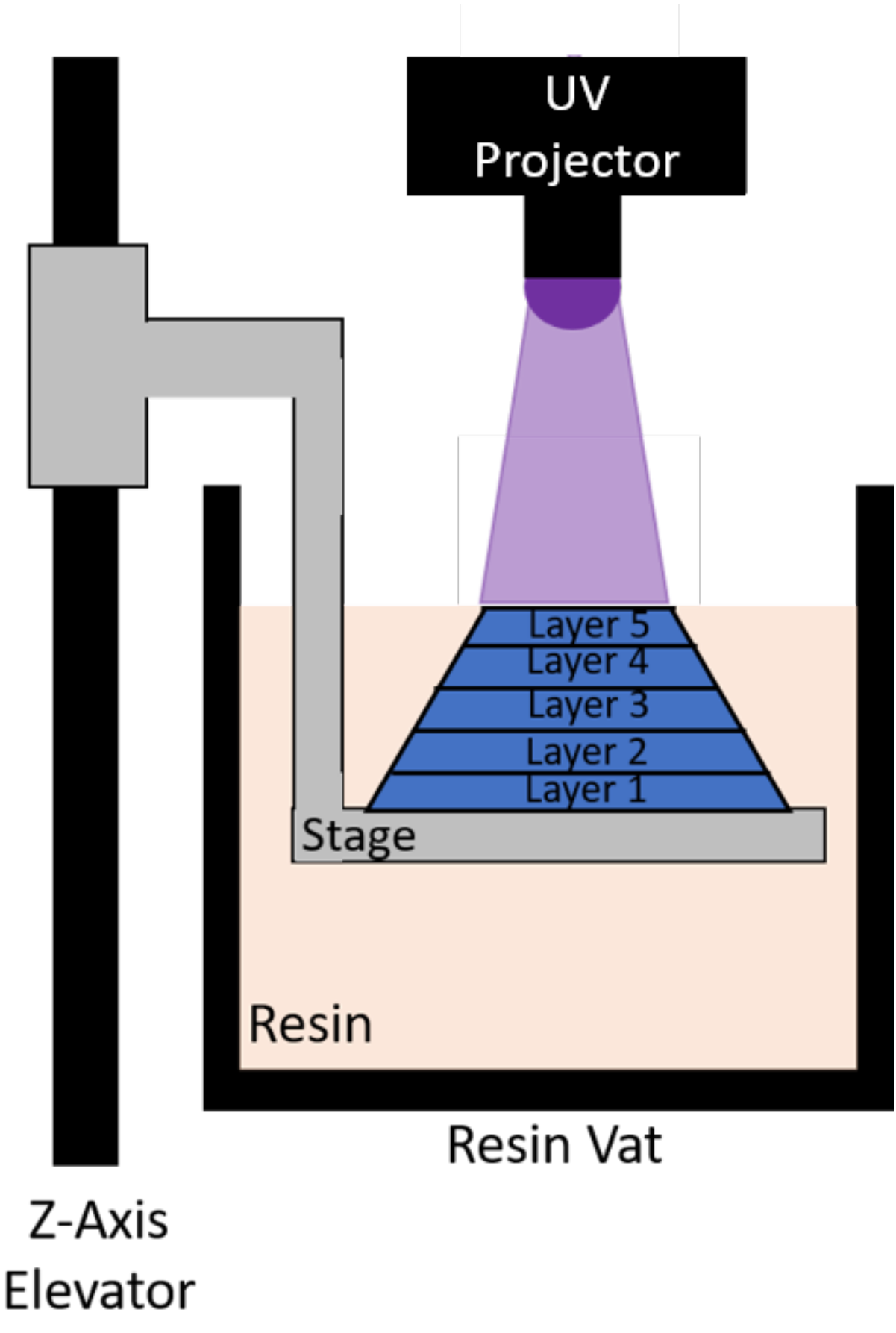
UV
Projector
Layer 5
Layer 4
Layer 3
Layer 2
Layer 1
Stage
Resin
Resin Vat
Z-Axis
Elevator

In order to fabricate stronger and more functional parts, particulate ceramic, metal, and polymer fillers are often added to these photocurable polymer resins. The filler is used to improve part properties as a composite or, as is common in highly loaded ceramic-filled parts, post-processed to high temperatures to pyrolyze the polymer matrix and sinter the ceramic filler to form a homogeneous ceramic part.

VP of particulate nanocomposites has gained popularity within the biomedical field for increasing the bioactivity of the photocurable matrix, frequently polyethylene glycol (PEGDA), through the addition of bioactive ceramics or polymers such as hydroxyapatite[54, 55, 56] or alginate[57]. The addition of these fillers has displayed increases in cell viability, with one study seeing 90% cell survival[57]. Other bio-sourced additives of chitin[57, 58] and bamboo fibers[59] have demonstrated increases in tensile strain and maximum stress. The incorporation of metals and performance ceramics in photocurable nanocomposite resins has enabled more unique properties such as a nanoclay[17] for increasing tensile stress and strain at break, and a copper-PEGDA lattice designed to achieve a negative coefficient of thermal expansion[60]. Magnetic composites have also been fabricated through magnetite particles to create cantilevers[61], impellers[62], and bone tissue scaffolds[63].

Printing complex high-resolution nanocomposites are challenging, especially with fillers that exhibit high reactive indices (>1.7). Materials with a high refractive index scatter light to a greater degree and tend to be more absorptive as well. Light scattering results in a redistribution of light intensity, which reduces cure depth and increases cure width[18, 64]. The increase in cure width limits the ability to fabricate small features, reducing the achievable resolution. Successful printing often requires a trial-and-error approach to optimize process parameters[12, 19, 65, 66, 67]. Predicting this behavior is crucial to producing complex nanocomposite parts to expand the geometries and applications of VP-printed parts.

3.2.2 Analytical modeling of filled resin curing

Generating an analytical relationship to predict the curing behavior of ceramic-filled VP resins has been a long-standing research goal, as doing so would enable automated correction of UV irradiation patterns to fabricate precise and accurate composite parts without the need to actually synthesize the filled resin of interest. Achieving this goal requires defining the light attenuation and curing exposure of the filled resin in both the build (Z) and orthogonal (XY) directions. In neat resins, this is typically defined by the penetration depth, D_p, and the critical curing exposure, E_c, deemed $D_{p,0vol\%}$ and $E_{c,0vol\%}$ for neat resin. $E_{c,0vol\%}$ is particularly difficult to analytically predict as it depends on photo-chemical parameters requiring in-depth characterization of the resin system composition and photo-curing kinetics[68]. Instead, $D_{p,0vol\%}$, and $E_{c,0vol\%}$ are typically experimentally determined by evaluation of a 'working curve' using Jacob's Equation, defined as,

$$C_d = D_p ln\left(\frac{E}{E_c}\right). \tag{3.1}$$

where C_d is the cure depth and E is the incident exposure at the resin surface. Equation 3.1 is derived from Beer's Law and is valid when assuming the resin is optically homogeneous. In filled resins, this assumption becomes invalid due to light scattering to form a quasi-Beer-Lambert relationship[18]. This causes E_c to no longer be the curing exposure of the matrix but the exposure required by the printer to produce a set cure depth, indirectly accounting for the different light intensity from scattering and attenuated light from particle absorption.

Gentry et al. expands this concept to the XY direction by defining excess width (W_{ex}) in a similar quasi-Beer-Lambert relationship defined as,

$$W_{ex} = W_p ln\left(\frac{E}{E_w}\right). \tag{3.2}$$

Where W_p is the penetration width and E_w is the critical curing exposure for the XY direction. Due to the non-isotropic nature of light scattering, $E_w \neq E_c \neq E_{c,0vol\%}$ in filled resins, because the exposure the printer irradiation source delivers does not increase the cure depth and cure width equally. Relating D_p, E_c, W_p, and E_w to measurable resin properties and existing scattering physics through novel empirical and analytical models has been the current focus within the field.

Empirical models relating interparticle spacing, particle size, particle volume loading, and radiation wavelength have demonstrated reasonable accuracy in predicting the cure depth of low refractive index (e.g., alumina and silica) nanoparticle-filled resins[69]. Interparticle spacing is a difficult resin property to determine for polydisperse particle systems, limiting this model to monodisperse, non-absorbing particles. A related term to interparticle spacing, transport mean free path, is able to be experimentally determined through diffuse wave spectroscopy and related to D_p[21]. Despite only requiring a single experiment, this method only predicts D_p and not E_c, limiting its usefulness in determining cure depths or widths. Proposed models address this by relating reaction kinetic and light attenuation factors to E_c and D_p[22, 23] and subsequently predicting cure depth. However, these relationships avoid relating E_c and D_p to scattering physics by isolating scattering variables to a single term. This scattering term is forced to be empirically solved, requiring the repeated processing of filled resin at each concentration of interest. Furthermore, all previously described models do not account for photocuring in the XY direction and/or require difficult experiments to acquire pertinent parameters for said models.

3.2.3 MCRT Simulation of Particle Filled Resins

Monte Carlo ray-tracing (MCRT) is a numerical approach that simulates bundles of photons, or rays, as they are reflected, absorbed, and scattered within an environment. MCRT provides a solution to describe the light scattering in the Z and XY directions that only requires inherent material properties, which are easily measured. There are two approaches to MCRT simulation, sudden death, where energy is a binary value, and slow death, where energy is continuous[70]. MCRT is typically used to model the light scattering in water clouds and dust; however, the same physics can be applied to VP to describe the light scattering in particle-filled resins from which the cure profile shape can be predicted.

Previous MCRT work in VP of filled systems has demonstrated a sudden death MCRT simulation that provided accurate predictions of cure profile dimensions, within 25%, of laser-based light sources[25, 71], without the need to fabricate and process the filled resin. These models assumed the particles were monodisperse, use scattering physics designed for dilute systems, and describe curing exposure threshold using reaction kinetic-based models.

This work improves upon these previous MCRT simulations for VP by incorporating polydisperse particle sizes, and particle volume loading-dependent light scattering physics. These modifications better describe the filled resin to produce a more realistic simulation. Additionally, this simulation determines a resin's critical curing exposure from a working curve of the neat, unfilled resin. Using working curves provides a fast and simple method to determine the curing exposure required for a specific material.

Validation of this simulation is demonstrated by comparing simulated and experimental cure profiles using zinc oxide (ZnO) nanoparticles (20 nm) within a photocurable resin at varying concentrations (1-5 vol%). The high refractive index (2.2) of ZnO, and low refractive index of the matrix (1.48), provide a useful case study that is comparable to other ceramics

used within the nanocomposite field.

3.3 Monte Carlo Ray-Tracing Simulation Details

3.3.1 Monte Carlo Ray-Tracing Model

The goal of the MCRT model is to predict the final cure profile shape by simulating the path of the rays of UV irradiation within the vat[25, 71]. The model accounts for the scattering events from individual particles and tracks the rays' energy as they travel within the vat. The simulation uses concentrated Mie scattering theory to statistically determine the distance and direction the rays travel, as well as the likelihood of particles absorbing or scattering the incident rays[72]. The accumulated energy from all the rays across a voxel of the vat is then compared to the neat resin's critical exposure to determine if the voxel is cured or uncured. Defining this cure boundary effectively defines the cured resin profile. The cure profile width and depth are metrics used to define the accuracy of the simulation compared to experimental trials.

The MCRT model uses five terms to dictate the behavior of the rays[72]:

1. Scattering intensity distribution, $I(\theta)$
2. Scattering coefficient, μ_s (μm^{-1})
3. Absorption coefficient, μ_a (μm^{-1})
4. Transport free path, Δs (μm)
5. Critical exposure to cure the neat resin matrix, $E_{c,0vol\%}$ (mJ/cm^2)

The logic and implementation of these terms in the context of the ray-tracing algorithm are displayed in Figure 3.2.

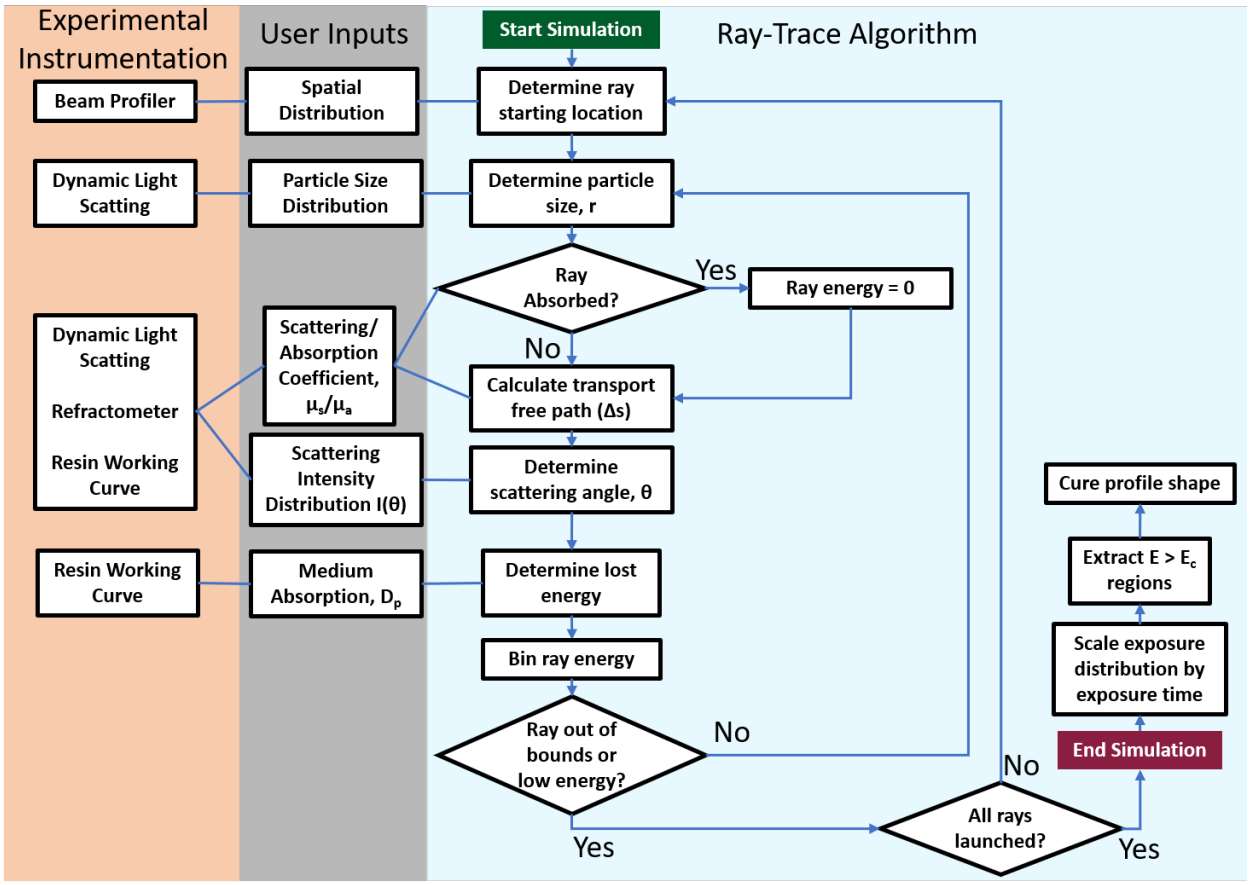

Figure 3.2: Flowchart of the ray-trace algorithm of a single scattering event and the exit conditions to acquire the image of the cure profile shape with corresponding user inputs and instrumentation necessary for resin characterization at each step.

The scattering intensity distribution, $I(\theta)$, serves as the starting point since all other terms are dependent upon it. $I(\theta)$ represents the relative scattering intensity with respect to the scattering angle, θ. When normalized, thus $\int_0^{2\pi} I(\theta)d\theta = 1$, the function yields the probability distribution function and is used to randomly compute the scattering angle by a particle during a scattering event. This probability function determines a ray's change in travel direction, and thus the shape of this function dictates the resulting energy distribution and cure profile shape. $I(\theta)$ is defined as

$$I(\theta) = P(\theta)S_F(\theta), \tag{3.3}$$

where, $S_F(\theta)$ is the structure factor and, $P(\theta)$ is the form factor. The structure factor is an angular function that describes the interparticle locations to correct interparticle polarization effects and interference of the scattered light. In systems with low particle volume loading, i.e. <1vol%, the structure factor becomes a uniform function with values approaching one, in which case light scattering is said to be independent. However, in VP resins, the particle loading is much higher, which requires the implementation of a structure factor, in which case light scattering is said to be dependent. The structure factor used in this work is the Percus-Yevick hard sphere approximation that accounts for particle size dispersity[73]. This is the first instance of modeling VP with an MCRT simulation using a structure factor and accounting for polydisperse particles. The impact of the structure factor on the scattering intensity distribution is displayed in Figure 3.3.

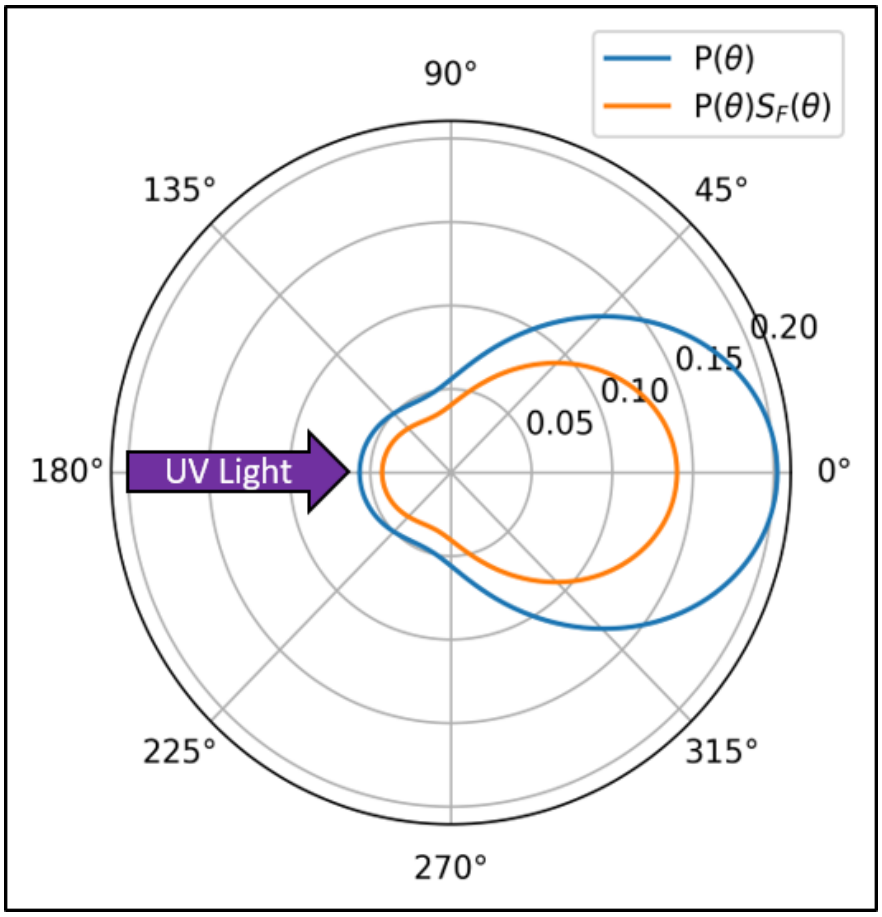

Figure 3.3: Example of scattering intensity distribution using independent light scattering (blue) and dependent light scattering (orange) for a 40 nm ZnO particle at 5 vol%. Dependent light scattering reduces the forward scattering and the magnitude of the scattering intensity distribution; this reduces the likelihood of rays being scattered and increases the probability of a ray being absorbed.

$P(\theta)$ is a scattering intensity distribution for infinitely dilute particles. For unpolarized incident light, $P(\theta)$ is defined as an average of the squared amplitudes of the angular dependent perpendicular and parallel scattering amplitudes, $S_1(\theta)$ and $S_2(\theta)$, respectively.

$$P(\theta) = \frac{|S_1(\theta)|^2 + |S_2(\theta)|^2}{2} \tag{3.4}$$

$S_1(\theta)$ and $S_2(\theta)$ are derived from Mie theory[74], and defined as,

$$S_1(\theta) = \sum_{n=1}^{n_{max}} \frac{2n+1}{n(n+1)}[a_n(m,x)\pi_n(\theta) + b_n(m,x)\tau_n(\theta)], \tag{3.5}$$

and

$$S_2(\theta) = \sum_{n=1}^{n_{max}} \frac{2n+1}{n(n+1)}[(a_n(m,x)\tau_n(\theta) + b_n(m,x)\pi_n(\theta)], \tag{3.6}$$

where

$$x = \frac{2\pi r}{\lambda}, \qquad \text{and} \qquad m = \frac{n_p + ik_p}{n_m}.$$

In Eqs. 3.5 and 3.6, π_n and τ_n represent the angular scattering patterns of the spherical harmonics, and a_n and b_n are the Mie coefficients. These coefficients depend on the size parameter (x) and complex refractive index ratio (m), where r is the particle radius, λ is the radiation wavelength, and n_m and $n_p + ik_p$ are the refractive index of the matrix and particle domain, respectively. Each $P(\theta)$ is associated with a specific particle radius, thus for each scattering event a new $P(\theta)$ is calculated with a new randomly selected particle size, using the particle size distribution as a probability distribution. The absorptive index of the matrix (k_m) is neglected from the form factor calculation as Mie theory is not mathematically stable when using a non-zero k_m. This assumption is valid in most cases since the particles exhibit much higher absorption compared to the matrix. The matrix absorption is accounted for later in the simulation using the Beer-Lambert law within the matrix, as is common in VP cure modeling.

The scattering coefficient, μ_s, and absorption coefficient, μ_a, represent the relative rates of scattering and absorption of the particles. Similar to $I(\theta)$, μ_s is dependent on the particle volume loading[72], ϕ, and defined by,

$$\mu_s = \frac{3\phi\pi Q_s}{2r}\int_{-1}^{1} I(cos\theta)dcos\theta. \tag{3.7}$$

where Q_s is the scattering efficiency factor defined as,

$$Q_s = \frac{2}{x^2}\sum_{n=1}^{n_{max}}(2n+1)(|a_n(m,x)|^2 + |b_n(m,x)|^2). \tag{3.8}$$

The scattering coefficient is a relative measure that must be compared to the absorption coefficient. Light absorption is assumed to be particle loading and particle size independent[72]. Defining the absorption coefficient as,

$$\mu_a = \frac{4\pi k_p}{\lambda}, \tag{3.9}$$

it depends only on the absorption index of the particle, k_p, and the radiation wavelength, λ. In order to assume a constant absorption, the MCRT simulation assumes coherent scattering. Normalizing the μ_s and μ_a such that $\mu_s + \mu_a = 1$ provides the probability of a ray being either elastically scattered or completely absorbed, respectively, determined by inverse transform sampling.

The magnitudes of μ_s and μ_a also contribute in defining the distance between scattering events, Δs, known as the transport free path (TFP),[72]

$$\Delta s = \frac{-\ln(RN)}{\mu_{s,avg} + \mu_a}, \tag{3.10}$$

where $\mu_{s,avg}$ is the weighted average of the scattering coefficients calculated with respect to particle size, and RN is a pseudo-random number uniformly distributed between 0 and 1.

The TFP is a statistical representation of the distance a ray must travel before undergoing a change in direction (scatter), or being absorbed. This distance is related to, but different from, the physical spacing of particles. The TFP is recalculated for each ray at each scattering event, avoiding the need to pre-generate particle volumes and locations, as well as providing the randomness to account for the Brownian motion of the particles. In the context of this simulation, the TFP distance is comprised solely of the resin matrix, enabling a simple relationship to define the absorption of a ray by the matrix using Beer-Lambert's Law,

$$E_n = E_{n,0} e^{-\Delta s / D_p(\lambda)}, \tag{3.11}$$

where E_n is the energy after absorption, $E_{n,0}$ is the initial energy, and $D_p(\lambda)$ is the matrix penetration depth and is dependent on the radiation wavelength. The energy of the ray absorbed by the matrix is recorded and later used to determine if a given voxel is cured or uncured.

3.3.2 Monte Carlo Ray-Tracing Simulation Algorithm

Equations 3.3-3.11 comprise the ray-tracing model, with Fig. 3.2 describing the algorithm of the simulation, the pertinent inputs required, and the instrumentation required to acquire said inputs. The simulation begins by calculating the rays' starting position by using the incident UV intensity distribution, which is measured with a beam profiler (displayed in Figure 3.6). Dynamic light scatting of low loading (0.1 vol%) resin provides the particle size distribution used as the sample set to randomly select the particle size, r, of a given scattering event, with each new scattering event requiring a newly selected particle size.

Absorption of the ray occurs through two mechanisms: the particle, dictated by nor-

malized Eqs. 3.7 and 3.9, and the matrix, dictated by Eqs. 3.10 and 3.11. If the particle absorbs the ray, the energy of the ray is set to zero, referred to as a sudden death event. As the ray travels through the matrix, the energy of the ray is decreased incrementally, referred to as a slow death event.

Once absorption conditions are completed, the ray is scattered/redirected via Eq. 3.3, and the location of the ray's new potential scattering event is calculated. If the ray is within the calculation volume of the simulation and has sufficient energy, the process repeats until the ray either travels outside of the simulation bounds or the energy goes below a specific threshold (e.g. 1% of the ray's original energy in this simulation). Once all rays are terminated, the simulation ends, and the resulting spatial energy distribution is normalized by the simulation mesh size and scaled by the exposure time to produce the spatial exposure distribution. Exposure values below the critical curing exposure, $E_{c,0vol\%}$, are removed from the mesh. Those remaining define the simulated cure profile shape.

3.4 Experimental Methods

The MCRT simulation presented in this work requires specific material parameters, specifically the particle size distribution, the complex refractive index of the photocurable matrix and the particle, UV projector spatial distribution, and the critical curing exposure of the matrix (Figure 4.2). This section discusses the experimental methods of how these parameters were acquired, the logic of the simulation, and the method of producing experimental cure profiles used to validate the simulation across a range of particle volumes.

3.4.1 Photocurable Resin Preparation

ZnO spherical powder and Diphenyl(2,4,6-trimethylbenzoyl)phosphine oxide photointiator (TPO) photoinitiator were purchased from Sigma Aldrich. The dispersing additives

DISPERBYK-985 were acquired from BYK. The photocurable components EBECRYL 893 polyester acrylate were acquired from Allnex. All reagents were used as received without any further purification.

All samples contained 15 vol% DISPERBYK-985, and 1 vol% TPO, with the remaining volume comprised of the EBECRYL 893 and ZnO nanopowder. Resins are made by dissolving the TPO into the DISPERBYK-985. Once dissolved, the solution is added to the ZnO powder followed by the addition of the EBECRYL 893. ZnO is added at varying loadings of 0, 1, 2, 3, 4, and 5 vol%. All resins are placed on a tube roller until the powder is dispersed, followed by sonication for 10 min. Finally, the vials of resin are mixed via a vortex mixer immediately before photocuring.

3.4.2 Resin Characterization

The ZnO particle size distribution was determined using dynamic light scattering (DLS) with a Malvern Zetasizer Nano ZS at concentrations of approximately 0.1 vol% in the resin matrix. The ZnO dry powder was also analyzed using a JEOL IT-500HR FEG scanning electron microscope to verify the DLS results. Literature values of the ZnO complex refractive index were used at $2.2 \pm 1e^{-4}i$[75]. The refractive index of the neat resin of 1.4755 was determined using an Abbe refractometer. The complex refractive index of the matrix resin and ZnO particles are assumed to be constant throughout the simulated exposure.

3.4.3 VP Process Characterization

Specimens were fabricated on a custom top-down VP printer equipped with a 405 nm UV-LED projector. The projected pixel size is 35.5 μm, with a maximum cumulative power flux of 6.2 mW/cm^2 measured by a Dymax ACCU-CAL 160 radiometer. The spatial light intensity distribution was measured using a Newport LBP2-HR-VIS3 laser beam profiler. The resulting spatial intensity was incorporated into the ray-tracing simulation.

3.4.4 Cure Profile Characterization

Cure profiles were fabricated using a 3D-printed custom-built vat filled with resin and a glass slide placed atop the resin surface, similar to the configuration described by Gentry et al.[18]. Twelve 7-pixel squares were projected through a glass slide to cure the resin on the opposite surface. The cured profiles were rinsed with isopropyl alcohol and left to air dry for five minutes.

The profiles were then imaged with a Dino-lite AM3111 digital microscope and cure depth and width were measured from the images at the deepest and widest sections of the profiles. The dimensions of the profiles were then plotted on a log-linear plot with their corresponding applied exposure. These 'working curves' were then used according to Equations 3.1 and 3.2 to determine the experimental C_d and W_{ex} for comparison against the corresponding values obtained from the MCRT simulation.

3.4.5 Monte Carlo Ray-Trace Simulation

Due to the symmetry of the applied irradiation profile, a single center row from the 7X7 pixel projection was simulated as a concession to simulation efficiency. The cumulative energy delivered within 1 s of exposure to the resin is divided evenly between the rays and launched based on the UV source intensity distribution. The MCRT simulation assumes that the matrix complex refractive index and particle size distribution remain constant for the duration of the radiation exposure and volume loading range studied. Since the resin's optical properties do not change during curing, the simulation only needs to be run once to generate a map of the intensity received by each voxel of the photopolymer resin vat. The intensity distribution is then scaled by exposure time to produce an exposure distribution.

Lastly, the simulation assumes the required exposure to cure a given region is inde-

pendent of the particle loading and depends only on the critical curing exposure of the matrix, $E_{c,0vol\%}$. Based on this assumption, the spatial exposure distribution is thresholded thus, $E \geq E_{c,0vol\%}$ is cured, and $E < E_{c,0vol\%}$ is uncured. The cured region's depth and width were measured to generate simulated working curves and compared to experimental working curves obtained using Equations 3.1 and 3.2.

The simulations were performed on a personal computer equipped with an Intel Core i7-8700 3.2 GHz 6-Core Processor, NVIDIA GeForce RTX 2060 6GB GPU, and 64 GB DDR4-3000 CL15 RAM. The simulation was coded in Python 3.10, and each simulation was comprised of 20 million rays, with the total energy input evenly divided equally among the rays.

3.5 Results and discussion

3.5.1 Monte Carlo Ray-Tracing Material Parameters

Neat Resin Curing Properties

The working curve of the neat acrylate resin for MCRT simulation (Figure 3.4) exhibits penetration depth ($D_{p,0vol\%}$) and critical exposure ($E_{c,0vol\%}$) values of 701 μm and 12.3 mJ/cm^2, respectively. These values were acquired using exposure times of between 3.5 s and 5.75 s (14.7 mJ/cm^2 and 24.15 mJ/cm^2 exposures), yielding cure depths between 125 μm and 500 μm. The working curve exhibits a strong log-linear relationship with an r^2 value of 0.99, indicating good agreement with Jacob's equation (Equation 3.1) and accurate $D_{p,0vol\%}$ and $E_{c,0vol\%}$ values for the simulations.

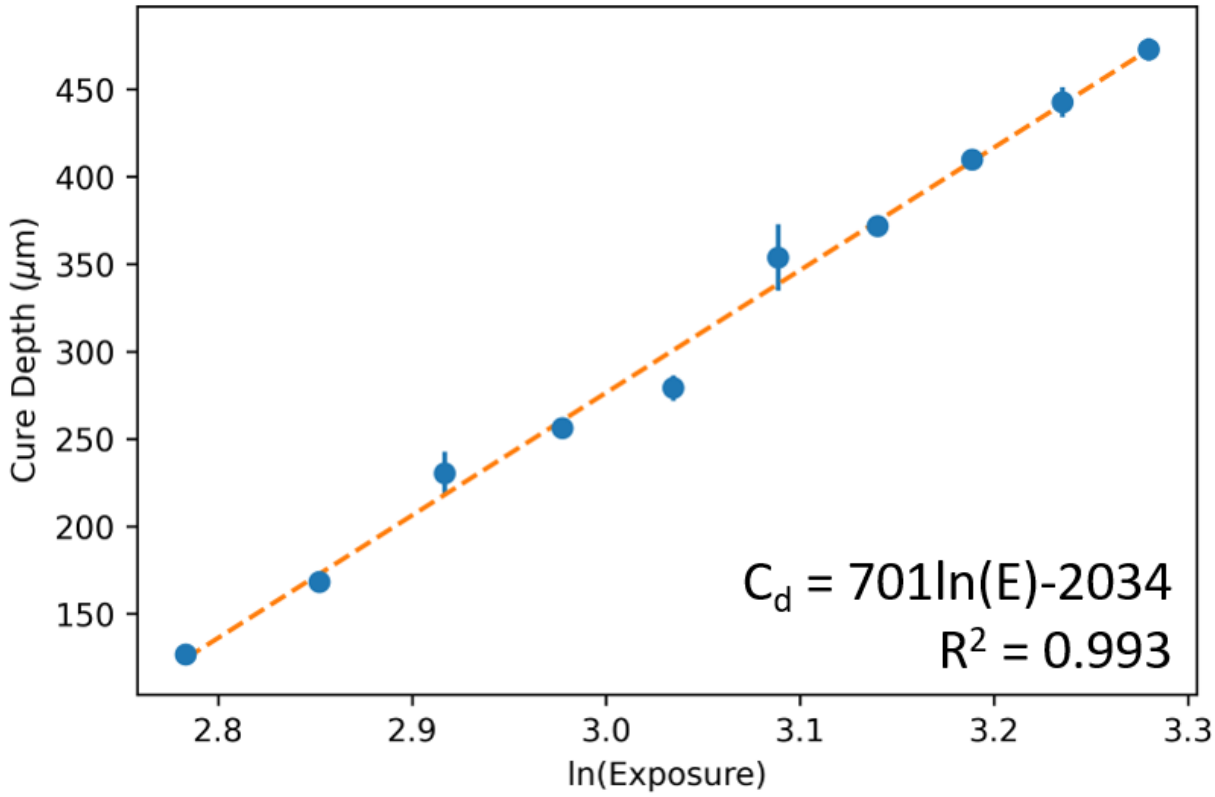

Figure 3.4: Working curve of the polyester acrylate matrix. The dotted line represents the log-linear best-fit line following Equation 3.1. Penetration depth and critical exposure from of the polyester acrylate matrix are 701 μm and 12.3 mJ/cm^2, respectively.

Powder Properties

Scanning electron microscopy (SEM) of the dry ZnO powder, displayed in Figure 3.5a, reveals the sphere-like shape of ZnO particles, approximately 20 nm in diameter. Dynamic light scattering (DLS) confirms this in Figure 3.5b, with a particle diameter spanning 15 to 50 nm, and a mean particle diameter of 21 nm. The MCRT simulation assumes the particles are spherical and that particle size distribution remains constant for all particle volume loadings tested. Particles were also assumed to be monolithic and dispersed with no aggregates in order to keep the scattering physics mathematically simple. This assumption is justified due to the use of small particles and low-volume loading[76, 77].

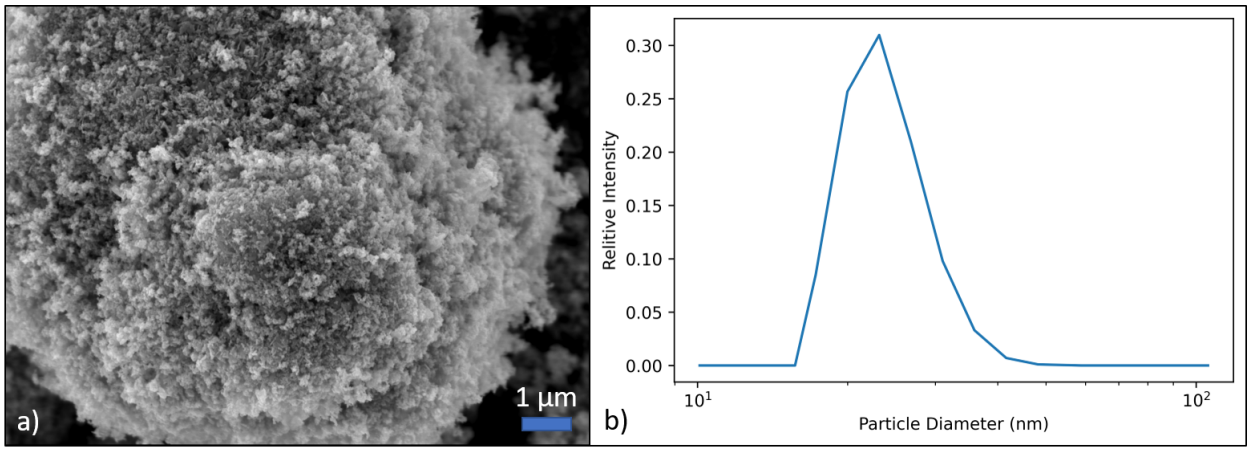

Figure 3.5: a) Scanning electron microscopy of dry ZnO powder at 11k magnification. b) The particle size distribution of ZnO particles dispersed in the photocurable matrix is determined by dynamic light scattering (right).

Process Properties

The UV projector's power flux distribution at the resin surface, displayed in Figure 3.6a, exhibits a 7X7 pixel array with a maximum power flux of 6.8 mW/cm^2 at the center of each pixel, and 6.2 mW/cm^2 cumulative power flux over each pixel area. In order to reduce the computational resources, the MCRT simulation utilizes the center row of pixels (Figure 3.6b) as the spatial intensity distribution when simulating the cure profiles. This method is reasonable due to each pixel not overlapping, indicated by each pixel outputting a similar power flux.

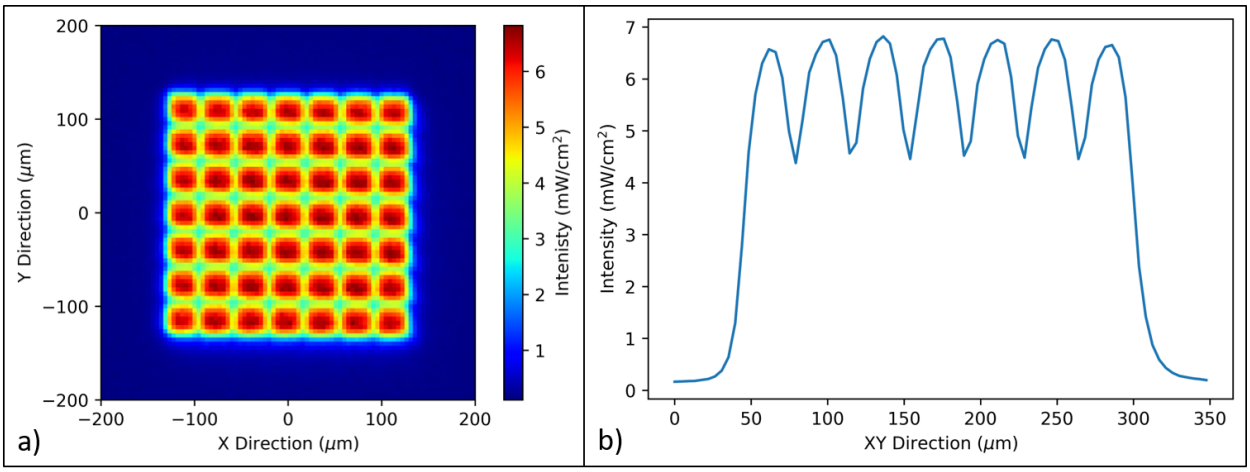

Figure 3.6: a) The intensity distribution of the projected 7-pixel array on the resin surface and b) the center row intensity used as the simulation input.

3.5.2 Simulation Results

Due to projecting only a 7-pixel-wide cure profile (Figure 3.6), and at reduced particle volume loading, individual pixels are observed within the simulated exposure map of the resin vat (top of Figure 3.7). The exposure also exhibits an expected distribution featuring the highest exposure at the resin surface radiating outward. The maximum accumulated exposure is also greater than the incident exposure, which indicates light scattering is redirecting rays and increasing the exposure the resin receives near the resin surface.

Removing exposure values lower than $E_{c,0vol\%}$ defines the cured region and the resulting cure profile. The cure profiles exhibit a curved surface and tapering edges near the resin surface, displayed at the bottom of Figure 3.7. Profiles are observed to decrease in depth with increasing particle volume loading, consistent with previous literature[18, 21, 22, 23].

Due to the tapered edges, the width of each simulated and experimental profile was measured at 5 μm below the glass slide surface to avoid the influence of the tapered edges. The profiles also exhibited increased width, but were not as pronounced as the cure depth de-

crease, potentially suppressed by the ZnO absorbing more light as the particle concentration increased.

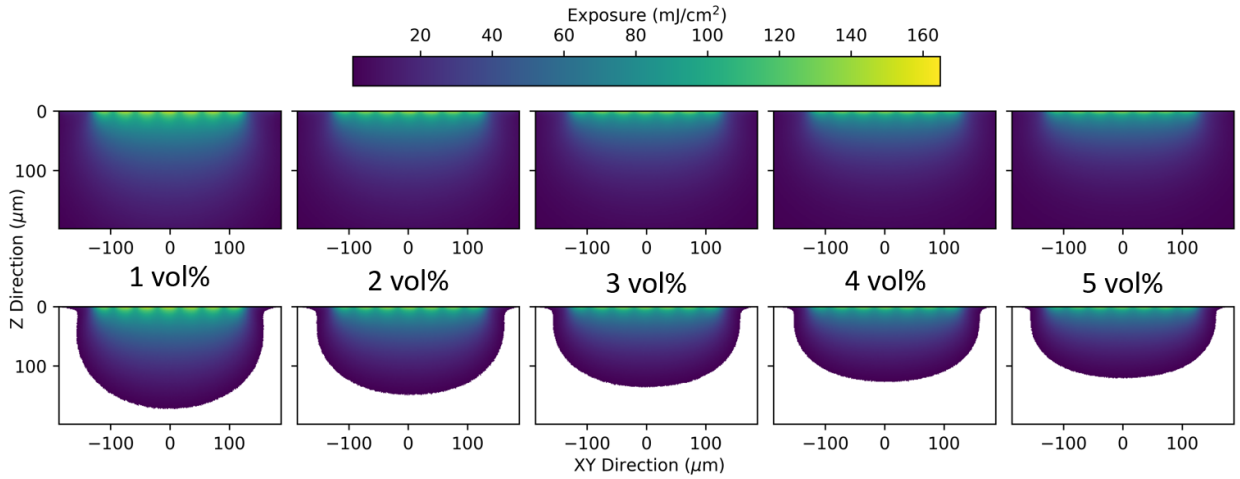

Figure 3.7: Simulated exposure maps of 1-5 vol% ZnO loaded resins exposed for 9 s (top). Removing the regions below $E_{c,0vol\%}$ reveals the cure profile for each loading (below)

.

3.5.3 Experimental Results

When exposed to UV, the unfilled resin exhibited a pyramidal cure profile with straight edges to a curved peak (Figure 3.8). This topology is different than expected compared to the incident surface intensity. The authors hypothesize that the refractive index of the neat resin is increasing during curing due to the crosslinking reaction densifying the polymer chains[78, 79]. This refractive index increase of cured resins creates internal reflections that alter the path of the light, creating a triangular-shaped cure profile[80]. With particles present, a portion of the light energy is absorbed, which slows the exposure received by the resin matrix, slowing the rate of increase in refractive index with respect to time, and minimizing the impact on the cure profile shape. Additionally, an increasing refractive index in a filled system is expected to reduce the scattering of the system as the refractive indices of the matrix and particle become closer.

Filled cure profiles of printed specimens exhibit expected trends of decreasing cure depths and increasing cure widths as ZnO volume loading increases. Due to scattering and absorption from the particles, the filled profiles all exhibit a near-hemispherical shape, reducing the impact of the increasing matrix's refractive index.

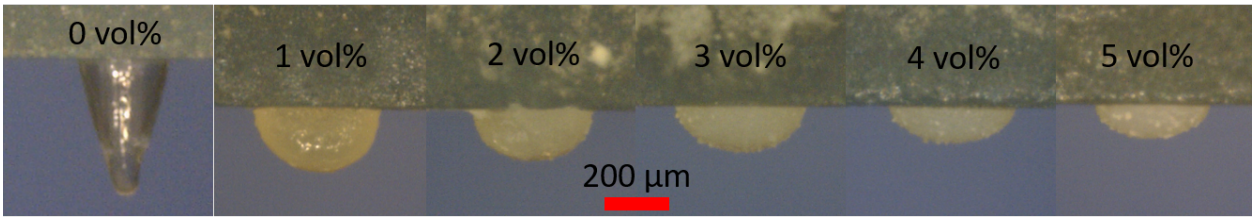

Figure 3.8: Experimental cure profiles of the matrix (0 vol%) were exposed for 4.5 s (27.9 mJ/cm^2), and filled profiles were all exposed for 10 s (62 mJ/cm^2).

3.5.4 Comparing Simulation and Experimental results

The measured C_d and W_{ex} are plotted against the natural log of respective exposure to create working curves for both the simulated and experimental data. Figure 3.9 compares the experimental and simulated working curves, plotted according to Equations 3.1 and 3.2. The simulation exhibits a high degree of accuracy, with all cure depth predictions within 20 μm, and excess width predictions within 15 μm, of experimental values. This error in the predictions is below the typical layer thickness (50 μm) and projection pixel size (35.5 μm), and thus below the controllable feature size of the printer.

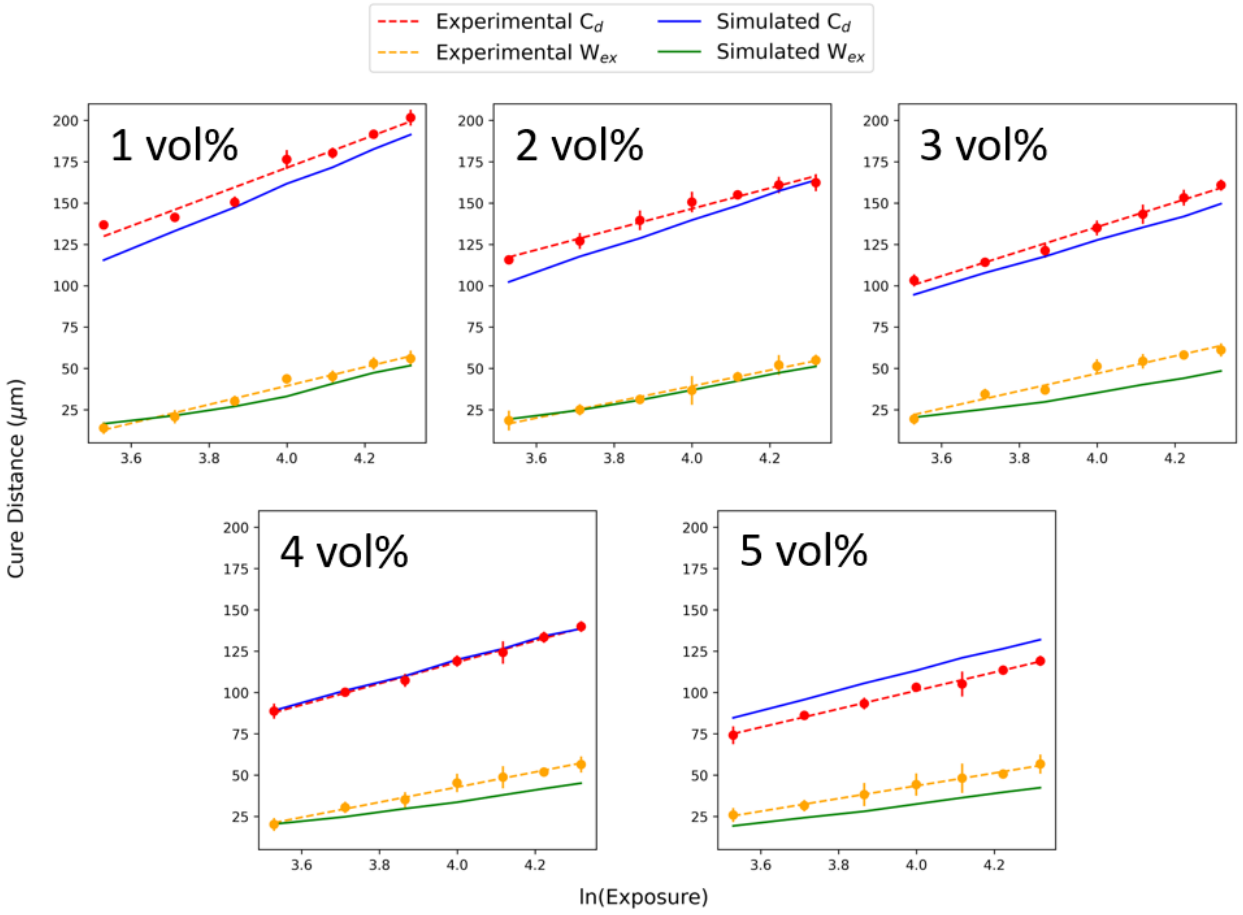

Figure 3.9: Comparison of simulated and experimental working curves. The dotted lines are the linear best-fit relationship based upon Equations 3.1 and 3.2 for the cure depth and over cure width, respectively.

Trends in the cure depth simulations are observed, with the simulation under-predicting the 1 vol% samples and subsequently achieving better predictions as the particle loading increases. In the 5 vol% samples, the simulation over-predicts the experimental cure depths. The opposing trend is seen in the cure widths, as the error between the simulation and experimental cure widths increases as ZnO loading increases.

Figure 3.10 displays the average percent error between the simulated and experimental cure depth and cure width for each ZnO volume loading in Figure 3.9. The value of each

data point indicates the average percent error between the simulated and experimental C_d and W_{ex} for each ZnO concentration tested. The error bars represent the standard deviation of these averages. Low standard deviations indicate the percent error to be near constant between each exposure, thus the slope of the experimental working curves (D_p or W_p) was accurately predicted. Conversely, if the standard deviation is large, the percent error deviates across the exposures tested resulting from the simulation not accurately predicting the slope of the experimental working curves.

In general, the simulation predicts the profile cure depth values and the D_p better than the width, specifically at the higher loadings tested. The percent error for the cure depth and cure width both exhibit the highest values, for the loadings tested, at 5 vol%. This is potentially caused by the filled resin becoming colloidally unstable or the simulation not accounting for the absorption of the matrix within the scattering intensity distribution.

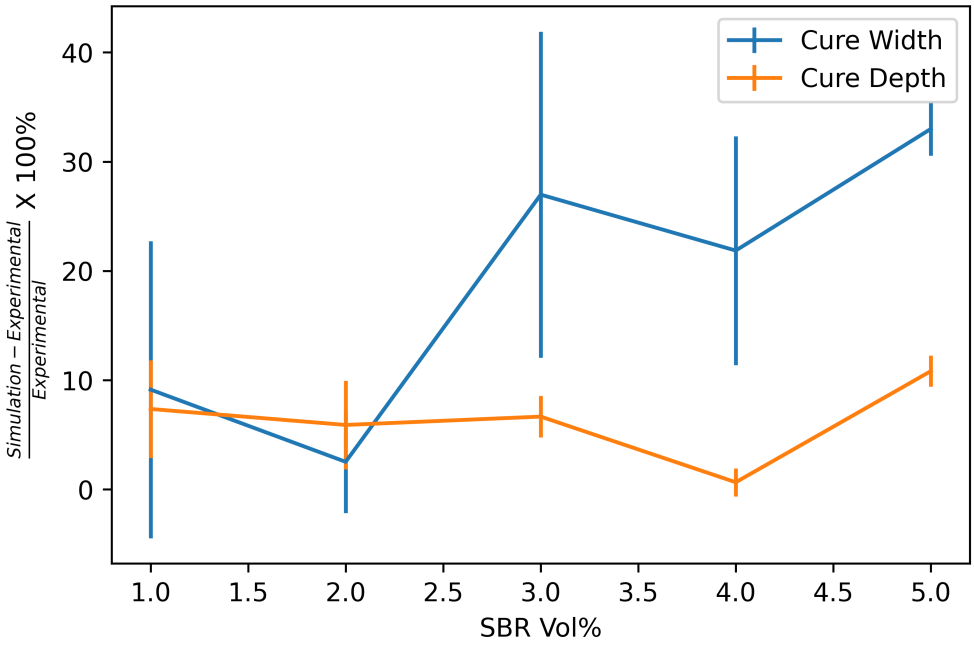

Figure 3.10: Average percent error between the simulated and experimental working curves at each ZnO loading. The error bars represent the standard deviation of these averages. A low standard deviation indicates the percent error of the simulation was constant and the simulation accurately predicted the slope of the cure depth and cure width working curves.

3.5.5 Discussion

Despite the strong agreement between the simulated and experimental working curves, a trend of the simulation over-predicting the cure depth and under-predicting the cure width is observed, especially as loading is increased. This is potentially caused by the ZnO aggregating more as the particle loading increases. As the particles aggregate, the scattering intensity distribution changes, which increases the side scattering and decreases the forward scattering, similar to the scattering of polycrystalline particles[76, 77]. Accounting for aggregated and polycrystalline particles is possible through future iterations of this MCRT simulation but will require the implementation of different scattering models that are currently being developed[81].

Increases in the refractive index of the matrix are not accounted for within the simulation and defy the assumption of constant optical (refractive and absorptive) properties during the simulation. However, this is not suspected to be a source of error within the simulation because as the refractive index increases, it becomes closer to the refractive index of the particle. The closer the refractive indices the less scattering occurs. This would be displayed by the simulation over predicting the cure width, which is not the case.

The particle volume loadings tested are relatively low compared to the high-loading (>35 vol%) ceramic-filled resins used for fabricating and sintering ceramic parts. The capability of this current model is limited to the modeling of nanocomposites, which typically use lower ceramic particle loading (<20 vol%)[17, 54, 55, 61]. Increasing the ceramic concentration presents challenges in both maintaining colloidal stability the assumption of non-aggregated particles that are discussed above.

3.6 Conclusion

Presented is the validation of a Monte Carlo ray-trace simulation that incorporates polydisperse particles, volume-loading-dependent light scattering physics to accurately predict the curing behavior of filled resin, without the need to fabricate or process the filled resins. The MCRT simulation was validated through comparison against ZnO-filled experimental cure depth and cure width measurements, which were in agreement within 20 μm. This highlights the value of this simulation for low-volume loading resins and high-refractive fillers. This accuracy is sufficient for the VP platform, as the simulation is able to match the resolution accuracy of the VP printer for low-concentration fillers.

The simulation exhibited trends of under-predicting cure width as particle volume loading increases. This trend is hypothesized to result from aggregating particles due to colloidal instabilities, hindering the application of the simulation to low loading of ZnO-

filled resins tested. However, the simulation is expected to predict well at higher loadings provided the resin exhibits colloidal stability. Aggregated particles are more difficult to model as the light scattering behavior deviates significantly from the physics used in this work. Overcoming aggregated particles may require a refined scattering model to determine the scattering behavior of aggregated and polycrystalline particles.

The MCRT simulation demonstrates accuracy in predicting cure profile shape with the input of material properties for a bitmap projection. In VP the material properties and a desired part geometry are known, but the bitmap required to produce said geometry is unknown. A more practical use for this simulation is to keep material properties constant and vary the bitmap projection and print parameters. As the bitmap projection and exposure times change, cure profiles are produced. This can be done iteratively to approach a target cure profile shape, enabling parts to better match designed geometries. Performing this process potentially requires executing the simulation thousands of times for each layer. In order to reduce the runtime, a machine-learning algorithm could be trained as a proxy for the simulation and significantly increase the throughput of the model.

3.7 Acknowledgments

This material is based upon work supported by the National Science Foundation under Grant No. 1762712. The authors owe a debt of gratitude to the Virginia Tech MSE characterization laboratory for access to the Abbe refractometer, the Amanda Morris research group for access to the UV-Vis spectrometer, and MII/ICTAS for access to the DLS. A special thanks to Dr. Lorenzo Pattelli from the European Laboratory for Non-Linear Spectroscopy (LENS) for discussions on light scattering of concentrated colloids.

Chapter 4

Simulation of Light Scattering in Vat Photopolymerization Latex Resins Using Monte Carlo Ray-Tracing

Keyton Feller[1,2], Viswanath Meenakshisundaram[1,2], J. Robert Mahan[1], Timothy E. Long[3] and Christopher B. Williams[1,2].

[1] Department of Mechanical Engineering at Virginia Tech.

[2] Macromolecules Innovation Institute at Virginia Tech.

[3] School of Molecular Science and Biodesign Center for Sustainable Macromolecular Materials and Manufacturing at Arizona State University.

Abstract

Vat photopolymerization (VP) of particle-filled resins provides a path toward enhancing the performance of printed photopolymers. Colloidal latex resins, in which polymer nanoparticles are suspended in a photocurable monomer, have been shown as a means of printing high molecular weight polymers without a detrimental impact on resin viscosity. However, VP of such suspension resins results in lower printing spatial resolution compared to optically homogeneous resins. This is due to the suspended particles scattering and/or absorbing the incident radiation and redistributing the light intensity orthogonal to the build direction.

The authors present a Monte Carlo ray-trace-based simulation that models the complex UV scattering behavior of filled colloidal resins in order to predict the resulting cured shape and potentially improve printing resolution. The MCRT simulation accounts for polydisperse particles, multichromatic light sources, and incorporates volume loading-dependent light scattering physics. With this simulation, single layers, or cure profiles, may be simulated using inputs that can be acquired via common characterization methods such as dynamic light scattering, Abbe refractometer, UV-vis spectrometer, beam profilometer, and VP working curves. Simulated cure profiles were validated using experimental printing/curing trials with a photo-curable styrene-butadiene (SBR) latex resin. Simulated cure profiles of SBR loadings from 5 vol% to 25 vol% predicted cure depths within 20% and cure widths within 50% of experimental values.

Keywords: Vat Photopolymerization, Monte Carlo Ray-Tracing, Additive Manufacturing, 3D Printing, Light Scattering, Latex

4.1 Glossary

C_d	Cure Depth
D_p	Penetration Depth
E	Incident Exposure
E_c	Critical Curing (Depth) Exposure
W_{ex}	Excess Width
E_w	Critical Curing (Width) Exposure
$I(\theta)$	Scattering Intensity Distribution
μ_s	Scattering Coefficient
μ_a	Absorption Coefficient
Δs	Transport free path
$E_{c,0vol\%}$	Critical Exposure of Neat Resin
$P(\theta)$	Form Factor
$S_F(\theta)$	Structure Factor
k_p	Particle Absorption Index
r	Particle Radius
λ	Wavelength
Q_s	Scattering Efficiency Factor
E_n	Energy of Ray
$E_{n,0}$	Initial Energy of Ray
$F_X(x)$	Cumulative Distribution Function
$F_X^{-1}(u)$	Inverse Cumulative Distribution Function
Pr	Probability Distribution Function

4.2 Vat Photopolymerization of Filled Resins

Vat photopolymerization (VP) utilizes UV irradiation to selectively cure low-viscosity photoactive resin, enabling high throughput printing of high-resolution features at unrivaled accuracy and precision, with respect to other additive manufacturing processes. However, VP's reliance on photocuring restricts material selection and its resultant properties. Researchers and resin manufacturers have looked to fill resins with particles to create composites and/or to photocure scaffolds around particles, which are later pyrolyzed to remove the scaffold and consolidate the embedded particles. VP of filled resins has enabled a wide variety of novel materials and composites for numerous applications, such as:

- hydroxyappitite[82, 83, 84, 85] for osteogenesis and bone tissue scaffolds,
- barium titanate[67, 86], polyvinylidene floride[38], and lead zirconate titanate[16] for piezoelectrics,
- carbon-based nano-structures[87, 88, 89, 90, 91] for fillers increasing thermal and mechanical properties,
- magnitite[92, 93] for imparting magnetic properties,
- silicon nitride[94] and tunston carbide[95] for high hardness applications,
- copper[96] and cobalt[95] for increasing thermal and electrical conductivity,
- high molecular weight styrene butadiene[2] for high strain hysteresis applications,
- and silica[97, 98, 99, 100], alumina[101, 102, 103, 104], and zirconia[104, 105, 106, 107, 108, 109] for a wide variety of high thermal stability applications.

While these suspended particles expand the VP materials selection and offer additional functionality, they tend to absorb and scatter the incident UV energy, which restricts the XY & Z resolution of each layer. As displayed schematically in Figure 4.1, the light scattering imparted by the suspended particles results in shallower and wider layers. Thus, producing parts from these filled resins at the resolution normally provided by VP requires accounting for light scattering from the particles present. Experimental and analytical approaches have been proposed to overcome the effects of light scattering in resins and maintain process resolution with varying trade-offs between applicability and generalizability.

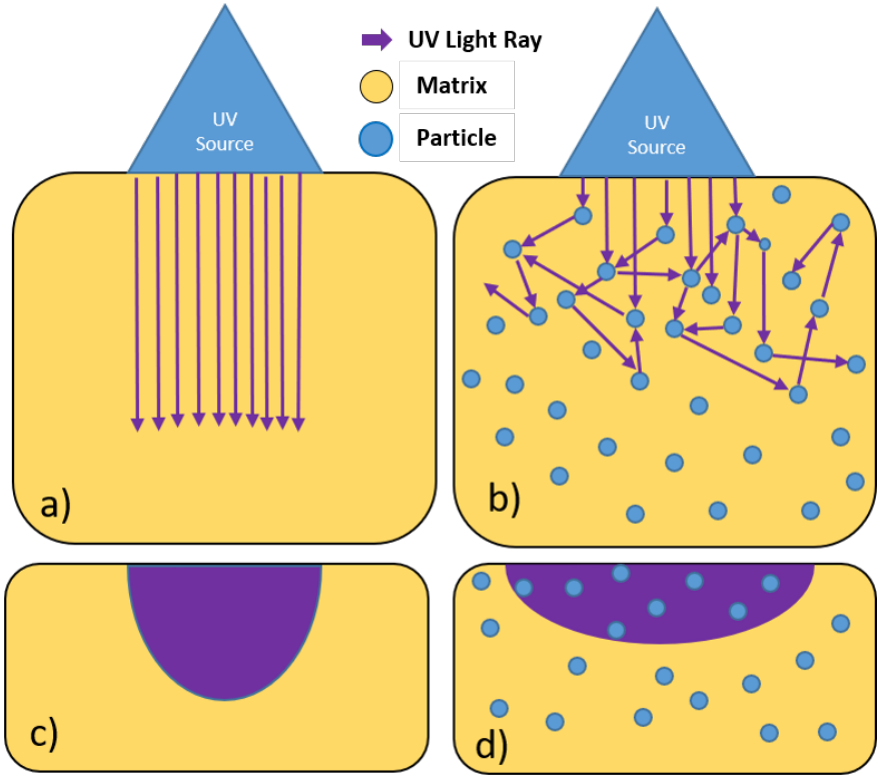

Figure 4.1: a) Homogeneous resin is optically clear causing the incident light to travel straight down limiting exposure to a particular area causing b) the homogeneous resin to cure only in the path of the incident light. c) With particles present, the light is scattered, increasing intensity near the resin surface and orthogonal to the incident direction, d) reducing cure depth and increasing cure width due to the redistribution of light intensity.

A recent experimental approach from Scott et al.[2] uses an embedded camera in the

VP system and computer vision algorithms to image the back-scattering intensity at the resin surface of a styrene-butadiene rubber (SBR) latex resin. The surface intensity measurements are fed into an algorithm along with the resin's working curve constants penetration depth, D_p, and critical curing exposure, E_c, to predict the layer shape. The bitmap shape is then iteratively changed until the predicted shape matches the desired layer shape. While this solution enabled precise printing of colloidal resin, its implementation has to be reconfigured for each resin formulation and VP system.

Many researchers have attempted to create generalized models to predict light scattering and photocuring. Initial approaches focused on developing modifications to the definitions of D_p and E_c to account for the light scattering and generate a modified Jacob's equation, a standard model for predicting VP cure depth. Griffith et al.[69] proposed a formula to linearly relate cure depth to the scattering efficiency factor. This method failed to predict experimental results using traditional definitions of the scattering efficiency factor but was able to force an empirical fit using the interparticle spacing as a proxy for the scattering behavior.

The effects of interparticle spacing and other scattering-related parameters within a cure model are difficult to capture due to complicating variables such as those associated with polydisperse particle systems. Wu et al.[21] demonstrated an experimental approach using a diffuse wave spectroscopy experiment to measure transport mean free path (TMFP), a related quantity to interparticle spacing but dependent on the light scattering properties of the resin rather than the physical spacing of particles. A proposed formula relating TMFP and D_p demonstrated good agreement between experimental and calculated data; however, this model requires a curve-fitting constant to relate these values. The constant's applicability to other resin compositions has yet to be tested.

Neither of these models addresses predicting a composite resin's critical exposure, in-

stead requiring an experimentally derived working curve on multiple filled resins or the specific filled resin of interest. This reduces their applicability and generalizability, as determining D_p and E_c are the critical values used to describe photocurable resins in VP. Other approaches that attempt to redefine both variables result in the isolation of the scattering terms, and require analysis of the resin working curve and/or require even more difficult experimentation to define[22, 23].

A numerical approach described by Tarabeux et al[24]. uses an iterative optimization technique to simulate the curing of multi-layer prints from a rastering laser. This approach requires an initial layer of cured material to define a numerically calculated scattering factor. Once the scattering factor is determined, the printer properties such as laser velocity, power, and spacing are able to be altered and subsequently simulated to provide part shape. While this was a highly applicable approach for fine-tuning processing parameters, this method is only validated on a single resin system and at a fixed particle loading, requiring each new material to be fabricated before being simulated. All of these prior approaches rely upon data acquired from the resin of interest or measurements that are more difficult than the typical trial-and-error working curves.

In order to avoid having to curate the filled resin of interest, Monte Carlo ray-tracing (MCRT) uses fundamental material intrinsic properties to simulate light-matter interactions. This enables individual components of a filled resin to be characterized but simulated as a mixed system. Examples of prior Monte Carlo ray-tracing (MCRT) simulations display the potential of utilizing simple material and printer parameters of particle size, refractive index, E_c of the resin matrix, and the light source intensity distribution to predict a composite resin's cure behaviors[110, 111]. Prior research in MCRT simulation of filled resins has predicted the cure depth and width of ceramic resins within 25%. The error within the simulation may be attributed to assumptions of mono-disperse particles, and the use of

dilute independent light scattering physics.

The authors have developed an MCRT simulation that accounts for polydisperse particles, and multichromatic light sources, and incorporates particle loading-dependent light scattering physics to model the light scattering and photocuring behavior of varying styrene-butadiene rubber (SBR) latex-based resins. Latex resins allow for high loadings and larger particle sizes due to their colloidal stability and amorphous morphology. Similar to the author's previous work, described in Chapter 3 this simulation still uses simple parameters of particle size distribution, the refractive index of matrix and particle phase, critical curing exposure, and the spatial intensity distribution of the light source, but it also uses a lamp-based light source. This source produces a broad spectrum of wavelengths requiring the rays to have a wavelength that dictates their optical behavior. The resulting MCRT simulation is validated by comparing the simulation results with experimentally determined cure depth and width measurements across a range of particle loadings.

4.3 Monte Carlo Ray-Tracing Simulation

The MCRT simulation predicts the photocured shape of filled resins by simulating bundles of photons, or rays, and their interactions with particles and resin. The rays within the simulation have a wavelength, position, direction, and energy value attributed to them, which may be altered by the particles and resin they interact with.

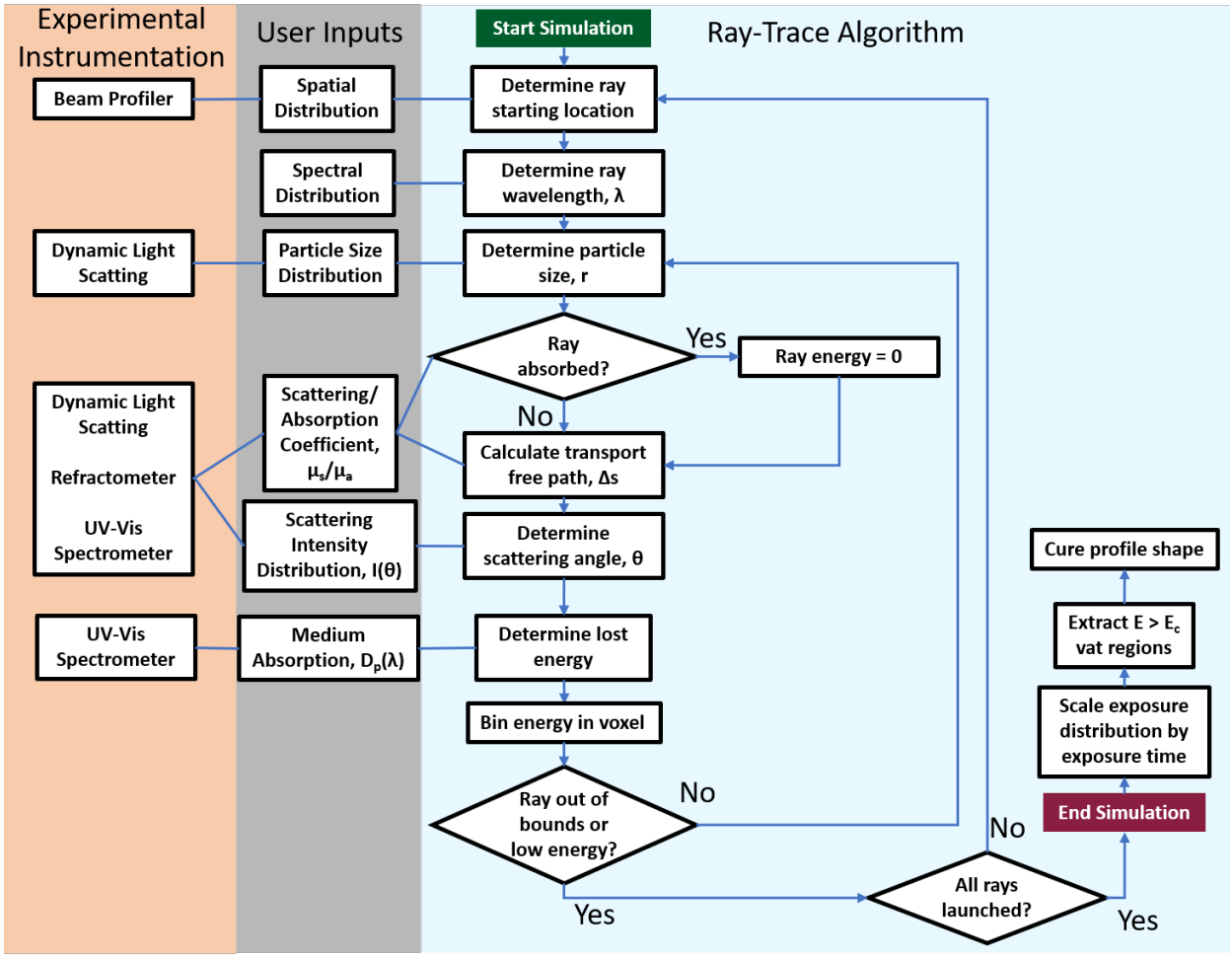

Figure 4.2: Flowchart of the ray-trace algorithm of a single scattering event and the exit conditions to acquire the image of the cure profile shape with corresponding user inputs and instrumentation necessary for each step.

The MCRT simulation begins with defining the starting location of the rays. This is accomplished by measuring the spatial distribution of light intensity of the light source with a beam profiler, shown in Section 4.5.1. The intensity of the spatial distribution is treated as a numerical probability distribution that is randomly sampled to determine the initial location of the ray using inverse transform sampling. This is performed using the cumulative distribution function, defined as,

$$F_X(x) = Pr(X \leq x) = p. \tag{4.1}$$

The cumulative distribution function, $F_X(x)$, describes the probability, p, of obtaining value $X \leq$ the input, x, in a given probability distribution function Pr. The inverse of $F(x)$,

$$F_X^{-1}(u) = x, \tag{4.2}$$

takes a random value, u, generated from a uniform distribution between 0 and 1 to output value x. This sampling method allows any numerical distribution to be pseudo-randomly sampled for the MCRT simulation.

Equations 4.1 and 4.2 are applied to the spectral distribution of the light source which determines the ray's wavelength. Both the spatial and spectral distributions are crucial for modeling VP today, as most VP printer manufacturers leverage lamp-based or UV-LED sources which exhibit a larger spectral bandwidth and non-Gaussian intensity distribution compared to laser-based sources. This requires sampling from a numerical distribution and not analytically described distributions. The energy of the rays is also calculated during these steps by equally dividing it between the incident energy, determined by the integration of the spatial distribution.

With the energy, wavelength, and location determined, the first scattering event is calculated. A scattering event is an interaction of a ray with a particle. The scattering event results in a ray either being redirected in the same or new direction (scattering) or absorbed by the particle (absorption). The first parameter in a scattering event is particle size. Particles within filled resins are polydisperse and are treated as such within the simulation by sampling using the particle size distribution acquired from dynamic light scattering (DLS)

as a probability distribution and sampled using Equation 4.2. For each scattering event, or when a particle size is required for subsequent calculations, a new particle size is sampled to simulate the polydispersity of the filled system.

To determine if the particle absorbs or scatters the ray, the scattering and absorption coefficients define the probability of scattering or absorption, respectively, when normalized, thus $\mu_s + \mu_a = 1$. Scattering and absorption coefficients are defined as,

$$\mu_s = \frac{3\phi\pi Q_s}{2r} \int_{-1}^{1} I(cos\theta) dcos\theta \tag{4.3}$$

and

$$\mu_a = \frac{4\pi k_p}{\lambda}, \tag{4.4}$$

where ϕ is the particle volume loading, r is the particle radius, Q_s is the scattering efficiency factor, $I(\theta)$ is the scattering intensity function, θ, is the scattering angle, λ, is the ray wavelength, and, k_p, is absorption index. If the particle absorbs the ray, the energy of the ray is set to 0; if the ray is scattered, the energy remains constant. Particle scattering and absorption are deemed sudden death events as the ray has binary outcomes.

The next step determines the distance the ray travels to the scattering event, referred to as the transport-free path, Δs. The transport-free path is defined as,

$$\Delta s = \frac{-\ln(RN)}{\mu_{s,avg} + \mu_a}. \tag{4.5}$$

Where RN is a random number uniformly distributed between 0 and 1, $\mu_{s,avg}$, is a weighted average across all μ_s values, with respect to the particle size and particle size distribution. The μ_a term does not need to be averaged as it only depends upon wavelength which is

fixed for the duration of the simulation for each specific ray. The ray travels straight down, orthogonal to the resin surface for the first scattering event, the distance of the transport-free path.

Rays that were determined to be scattered, require the scattering angle, θ, to determine the new direction of the ray. The scattering angle is determined from the scattering intensity function, $I(\theta)$ defined as,

$$I(\theta) = P(\theta)S_F(\theta), \tag{4.6}$$

where $P(\theta)$ is the form factor and $S_F(\theta)$ is the structure factor. The form factor is derived from Mie theory, which assumes the scattering particle is infinitely dilute (< 1 vol%). In filled systems, the particle loading is higher causing interference from the neighboring particles and changing the scattering intensity distribution. This phenomenon is called dependent light scattering and is corrected by using a structure factor. The structure factor used in this simulation is the Percus-Yevick hard sphere approximation modified to account for both a polydisperse particle distribution and charge interactions under a Yukawa (screened Coulomb) potential[73]. Prior VP MCRT work has ignored dependent scatter; i.e., the structure factor is assumed to be 1[110, 111]. Similar to previous variables, the scattering angle is sampled from $I(\theta)$ using Eq. 4.2 to dictate the ray's new direction.

The last phenomenon to account for the scattering event is the loss of the ray's energy due to the resin absorption. In photocurable resins, light is absorbed by the photoinitiator to initiate polymerization. The resin absorption can be accounted for by using the resin penetration depth D_p, from the working curve of the neat resin[112]. However, in multichromatic UV light sources, each wavelength is absorbed differently; this requires the absorption of each wavelength to be known. This is accomplished by UV-Vis spectroscopy of the resin

to define the absorption across the bandwidth of the UV light source (Section 4.4.2). Using Beer-Lambert's Law, the energy of the ray, E, is defined as,

$$E = E_0 e^{-\Delta s / D_p(\lambda)}, \tag{4.7}$$

where E_0, is the intial energy of the ray before traveling distance Δs to the scattering event. Equation 4.7 is applied for each ray with corresponding $D_p(\lambda)$ for the ray's wavelength. The energy absorbed by the matrix is added to a voxel mesh.

These steps complete one scattering event resulting in the evaluation of the ray's energy and location. If the energy and location of the ray are sufficient, the new particle size for the next scattering event is calculated for the simulation to repeat. If the energy of the ray is too low or the ray is out of the bounds, set by the simulation, the ray is eliminated. If more rays need to be simulated, the next ray is generated to begin the simulation. If all rays have been simulated, the simulation ends.

The simulation outputs a spatial energy distribution that is normalized by the simulation mesh size to produce the power flux distribution. This distribution is scaled by the desired exposure time to produce the spatial exposure distribution. The exposure values for each voxel in the simulation are compared to the critical curing exposure, $E_{c,0vol\%}$, acquired from the neat resin working curve. Voxels below $E_{c,0vol\%}$ are removed from the mesh while those greater than $E_{c,0vol\%}$ define the simulated cure profile shape.

4.4 Experimental Methods

The MCRT simulation produces an exposure distribution within the vat using experimentally measured scattering parameters of particle size distribution, complex refractive index, and the UV irradiation source's intensity distribution. In an effort to validate this

MCRT simulation and its use on colloidal resins, resins featuring a range of SBR particle volume loadings were synthesized, characterized, and printed in a top-down VP system. The results of the MCRT-simulated cure profiles are then compared against the physical measurements of printed specimens for each loading.

4.4.1 Photocurable Latex Resin

Styrene butadiene rubber (SBR) latex (Rovene 1476) was donated from Mallard Creek Polymers Inc. The latex contains 50 vol% SBR with particle diameters ranging from 120-170 nm. The particles are charged and stabilized with a small amount of carboxylic acid neutralized by ammonia. Matrix components include 1-Vinyl-2-pyrrolidone (NVP) and poly(ethylene glycol) (PEGDA 575 g/mol), purchased from Millipore Sigma and used as received. The water-soluble photoinitiator, lithium phenyl-2,4,6-trimethylbenzoylphosphate (LAP) was synthesized from dimethyl phenylphosphonite (purchased from Alfa Aesar), 2,4,6-trimethylbenzoyl chloride, lithium bromide (purchased from Fisher Scientific), and 2-butanone (MEK) (purchased from Millipore Sigma), and combined following the procedure described in Fairbanks et al.[113]. All reagents were used as received.

Photocurable latex resins used were modified from previous work[2, 3] at loadings of 0, 5, 10, 15, 20, 25, 30 vol% SBR particles with respect to the entire system. The NVP, PEGDA concentrations were kept constant for all samples at 9.25 vol%. LAP was also kept constant at 0.5 wt% of the total resin mass for all samples. The remaining vol% was comprised of added deionized water. Resin formulation is completed under constant stirring, which begins with the addition of deionized water to the SBR latex, followed by multiple small additions of LAP until the entire amount is dissolved, and lastly, slow (1 drop/s) drop-wise addition of the NVP/PEGDA mixture.

4.4.2 Characterization of Resin

The SBR particle size distribution was determined using dynamic light scattering (DLS) with a Malvern Zetasizer. Measurements were taken at 1 vol% SBR in deionized water and repeated in triplicate. The refractive index of the matrix was measured using an Abbe refractometer, and literature values were used for the RI of the SBR of 1.57[114]. The penetration depth of the matrix, $D_{p,0vol\%}$, and the absorption index of the SBR, k_p, were measured using an Agilent Cary5000 UV-Vis-NIR. Absorption of the liquid matrix and an SBR film were measured separately at wavelengths, λ, ranging from 350 nm to 500 nm in polystyrene cuvettes. The absorption values, A, were converted to absorption coefficient, α,

$$\alpha = 2.303A/t, \tag{4.8}$$

where t is the path length of the sample. The absorption coefficients are then converted into penetration depth, D_p, or the imaginary component,

$$D_p = \frac{1}{\alpha}, \tag{4.9}$$

and the refractive index, k, of the matrix or SBR

$$k = \frac{\alpha\lambda}{4\pi}. \tag{4.10}$$

4.4.3 Characterization of VP Process

A custom top-down mask-based VP printer, equipped with a high-resolution 1080p Texas Instruments DMD (0.65”) projector, was used to fabricate experimental specimens

for simulation validation. A Dymax Bluewave 75 spot-cure lamp broad spectrum UV with emission ranging from 350 to 500 nm was used as the light source. Filters within the projector significantly reduced the power flux below 400 nm. After magnification, the projected pixel size is 31.75 μm, with a maximum cumulative power flux of 22.68 mW/cm^2. The spatial light intensity distribution was measured using a Newport LBP2-HR-VIS3 laser beam profiler. The spectral intensity distribution provided by the light source manufacturer was used, displayed in Section 4.5.1. The resulting spatial and spectral intensity distributions were incorporated into the ray-trace simulation to determine ray location and wavelength, as per Figure 4.2.

4.4.4 Characterization of Printed Cure Profiles

Cure profiles were fabricated by projecting UV radiation through a glass slide that is placed on the surface of the resin vat; similar to the configuration described by Gentry et al.[18]. A 32-square pixel bitmap was projected for different exposures through the glass slide, curing the resin on the opposite surface. The resultant cure profiles were rinsed with DI water, and excess water on the glass slide was blown away with compressed air. The remaining water on cured layers was then removed with a Kimwipe. The printed cured profiles were then imaged from the size with a Dino-lite AM3111 digital microscope. Figure 4.3 provides a schematic of the measured dimensions of the cure profiles.

The neat resin cure profiles are characterized using Jacob's equation to relate the exposure dosage to the resulting cure depth (Z-direction) defined as,

$$C_d = D_p ln\left(\frac{E}{E_c}\right), \tag{4.11}$$

where, E, is the incident exposure irradiation of the resin surface, C_d, is the cure depth

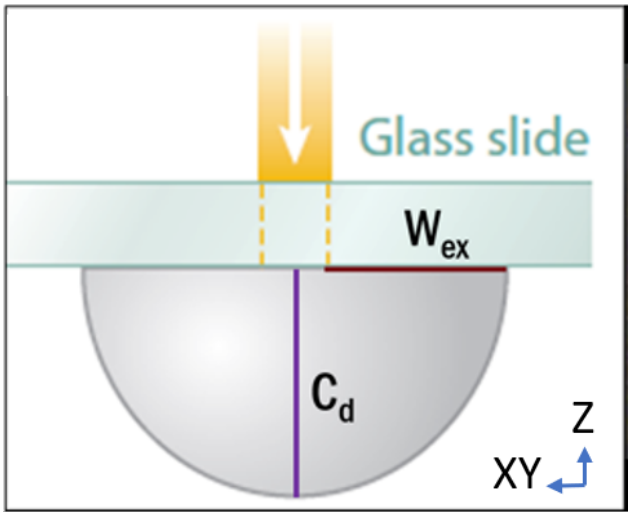

Figure 4.3: Schematic of a cure profile and the measured quantities of cure depth, C_d, and cure width overcure, W_{ex}, to characterize a cure profile.

of the cure profile, D_p, is the penetration depth, and E_c is the critical curing exposure. Equation 4.11 is used to calculate the critical curing exposure of the neat resin, $E_{c,0vol\%}$, used in the simulation. Jacob's equation is derived from Beer-Lambert's Law which assumes a homogeneous material; however, filled resins are still able to be modeled using a quasi-Beer-Lambert relationship to describe the cure depth and width directions[18]. Relating cure width and exposure is described by,

$$W_{ex} = W_p ln\left(\frac{E}{E_w}\right), \tag{4.12}$$

where W_{ex} is the excess cure width or the cure profile width minus the desired cure width from the bitmap projection (1016 μm for this work). W_p is the cure width sensitivity or the rate of change in the profile cure width, and, E_w, is the width critical exposure dosage. Due to the quasi-Beer-Lambert relationship, E_c and E_w of filled resins are not real exposure values but relative terms to describe the ease of the resin to cure in the Z or XY direction, respectively.

4.4.5 Implementation of the Monte Carlo Ray-Trace Simulation

The experimental inputs of UV projector intensity distribution, particle size distribution, refractive index, and medium D_p (referred to as $D_{p,0vol\%}$) are used to calculate transport free path, scattering coefficient, absorption coefficient, and scattering intensity distribution. These terms dictate the rays' travel and interactions within the simulation, as shown in Figure 4.2.

The simulation begins with determining the position and wavelength of the ray using the spatial and spectral intensity distribution, displayed in Section 4.5.1 (Figure 4.4). The first particle size is calculated which dictates how the ray is scattered/absorbed. If the particle absorbs the ray, its energy is reduced to 0, if the ray is scattered, the energy remains constant. The transport-free path, the distance the ray travels in the matrix to reach the particle, and the scattering angle are calculated, to determine the direction and distance the ray travels after scattering. The energy of the ray is reduced based on the distance traveled and the $D_{p,0vol\%}$. This process continues until all of the rays are absorbed or exceed the spatial bounds set by the simulation. The energy of the rays are recorded throughout the simulation to produce a spatial exposure distribution that is scaled by the desired exposure time. Exposure values less than $E_{c,0vol\%}$ are defined as uncured and are removed to produce a simulated cure profile.

The simulations were performed on a personal computer equipped with an Intel Core i7-8700 3.2 GHz 6-Core Processor, NVIDIA GeForce RTX 2060 GPU, and 64 GB DDR4-3000 CL15 RAM. The simulation was coded in Python 3.8, and each simulation was comprised of 40 million rays.

4.5 Results and Discussion

4.5.1 Characterization of MCRT Simulation Inputs

Irradiation

Previous MCRT simulations of VP are based on laser sources, enabling an assumption of a single wavelength and a Gaussian intensity variation within the beam radius[111]. However, such simple analytical curves cannot represent the output of projectors with bulb sources that contain spectral distributions across multiple wavelengths. Figure 4.4 displays the measured spectral distribution and the UV source intensity distribution at the resin surface for the lamp used in the experiments described here. Because simple analytical equations can describe neither of these distributions, the present simulation uses numerical representations of these measurements for all bitmap projections and spectral distributions. Both distributions are described by probability distribution functions when determining the wavelength and starting location for a given ray entering the resin in Section 4.5.2.

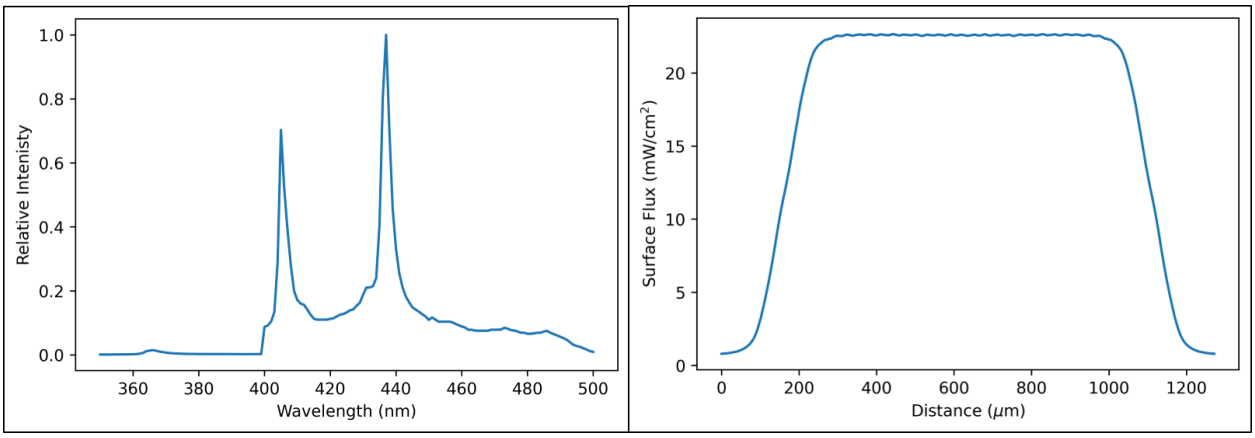

Figure 4.4: Spectral distribution of the incident radiation (left) and spatial flux distribution at the resin surface (right). These data are utilized as probability distribution functions to determine the wavelength and starting location of a given ray.

Particle Size

Particle size distribution measurements via DLS revealed SBR particle radii between 45 and 128 nm, with a mean radius of 70 nm, as shown in Figure 4.5. The particle size distribution is assumed to remain constant and independent of particle volume loading within the MCRT simulation.

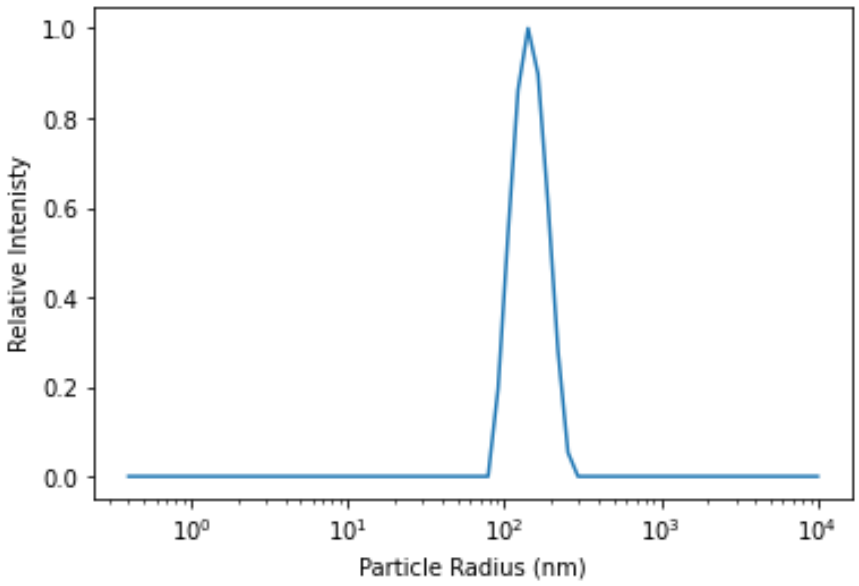

Figure 4.5: Dynamic light scattering of SBR latex particles at 1 vol%. The mean particle radius is 70 nm.

Literature sources indicate a refractive index of SBR of approximately 1.57[114]. Refractive index measurements of the uncured and cured matrix via refractometry yielded 1.355 and 1.356, respectively, indicating the refractive index is not increasing significantly and is constant for the duration of the exposure. The increase of refractive index in the matrix is potentially suppressed due to the high water content being the dominant factor in the refractive index of the matrix. Other solvent-based resins are expected to exhibit similar behavior while photocurable moieties are at low-volume loadings (<50 vol%).

Absorption

The absorption index of the SBR and penetration depth of the matrix as measured by UV-vis spectroscopy are displayed in Figure 4.6. Both the matrix and SBR exhibit higher absorption at lower wavelengths. Inversely, the majority of the projector spectral intensity (Figure 4.4), occurs at wavelengths >400 nm. This creates an inefficient energy transfer to the photoinitiator (LAP), as it only absorbs light <420 nm[113], which leaves only a 20 nm bandwidth to be used for photo-curing. Because of the nonlinear relationship between D_p and wavelength, the simulation uses wavelength-dependent $D_p(\lambda)$ data from UV-vis spectroscopy, rather than an average D_p that is typically acquired from an experimentally established working curve.

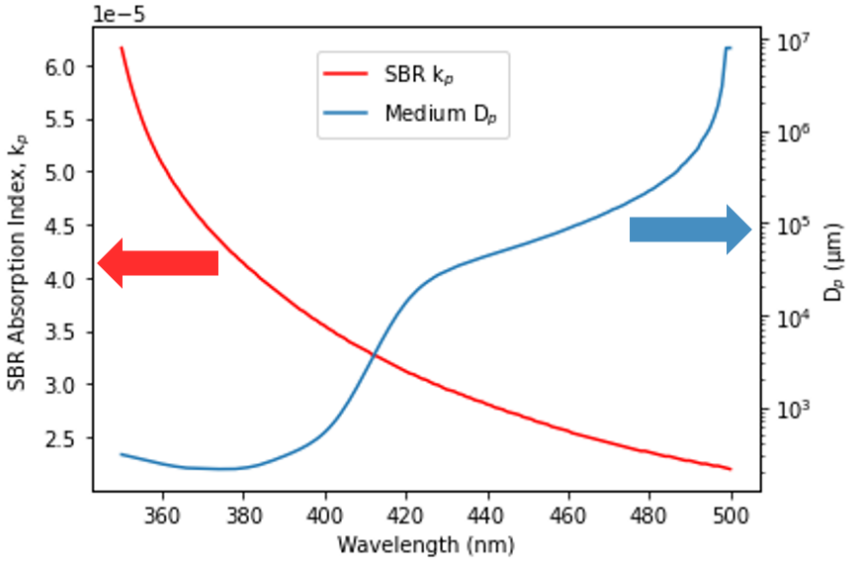

Figure 4.6: Measured absorption of SBR film and penetration depth of the matrix.

The low absorption rate of the matrix at wavelengths above 400 nm (Figure 4.6) results in the 0 vol% SBR resin's high D_p and E_c values of 6835 ± 256 μm and 40.4 ± 8.7 mJ/cm^2, respectively, extracted from the 0 vol% experimental working curve shown in Figure 4.7. The neat resin's lack of light attenuation results in low crosslink density and tall cure profiles.

Due to the neat resin's low cure modulus, these profiles are difficult to measure and may exhibit different photocuring properties than those measured, discussed in Section 4.5.4.

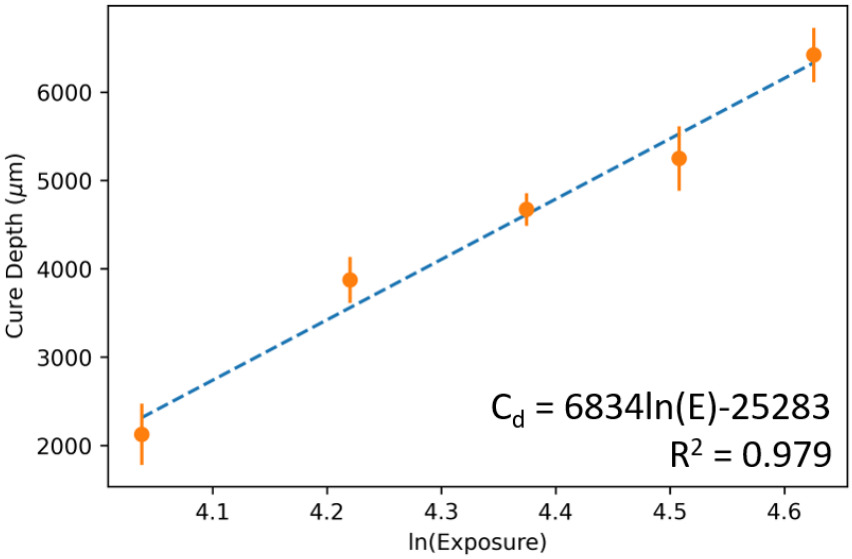

Figure 4.7: Experimental working curve of the resin matrix containing no particles. The equation and R^2 value of the log-linear best-fit line is displayed. Penetration depth and critical exposure of the neat resin are 6834 μm and 40.4 mJ/cm2, respectively.

4.5.2 MCRT Simulation Results

The simulation of each SBR resin formulation displays a smooth exposure gradient into the vat with the highest energy at the surface of the resin. Examples of simulated exposure distributions for 6 s (136 mJ/cm^2) of exposure time across each SBR volume loading tested are displayed at the top of Figure 4.8.

The resulting exposure distributions of the 5 vol% and 30 vol% resins exhibited a maximum exposure value at the resin surface of 300 to 333 mJ/cm^2, respectively, for a 6 s exposure (136 mJ/cm^2). These maximum accumulated exposure values are more than double compared to unfilled resin, which had a maximum exposure of 136 mJ/cm^2. This is an expected outcome due to scattering light energy accumulating near the resin surface for

filled resins.

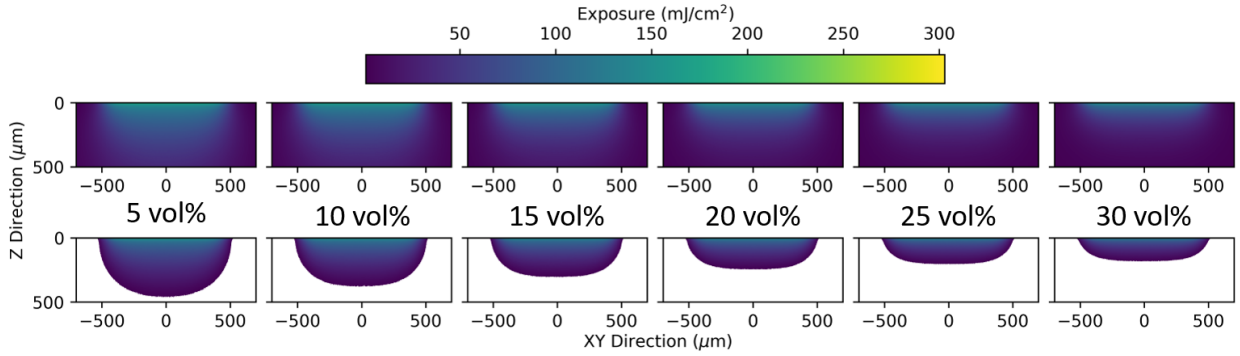

Figure 4.8: Exposure distribution from 5 to 30 vol% exposed for 6 s (136 mJ/cm^2) created by the simulation (top). Removing the pixels below the critical exposure to cure, $E_{c,0vol\%}$, displays the cure profiles (bottom). Due to increased particle scattering and absorption, the cure profile depth reduces as SBR vol% increases.

By removing the exposure values below $E_{c,0vol}$ from the MCRT exposure maps (Figure 4.8a), the cure profiles are revealed. The resultant predicted cure profile is visualized at the bottom of Figure 4.8. Due to the increased scattering and absorption, the simulated cure profiles display a reduced cure depth as the SBR vol% increases. The cure width is expected to increase as the SBR vol% increases, however, the authors suspect that the absorption of SBR reduced the increase in width. Most notably, the simulated profiles exhibit a tapering effect at the resin surface, resulting in a very thin cure depth at either end of the profiles.

4.5.3 Experimental Printing Results

Experimental printing conditions demonstrate that introducing SBR particles increases light attenuation and decreases profile depth, observed in Figure 4.9. The 0 vol% SBR resin cure profiles exhibited a curved surface, despite the incident intensity distribution being flat. The curved surface is attributed to the resin being a gel and the surface tension of the water forcing the cure profile to be rounded, unlike non-solvent-laden resins which exhibit more triangular cure profiles.

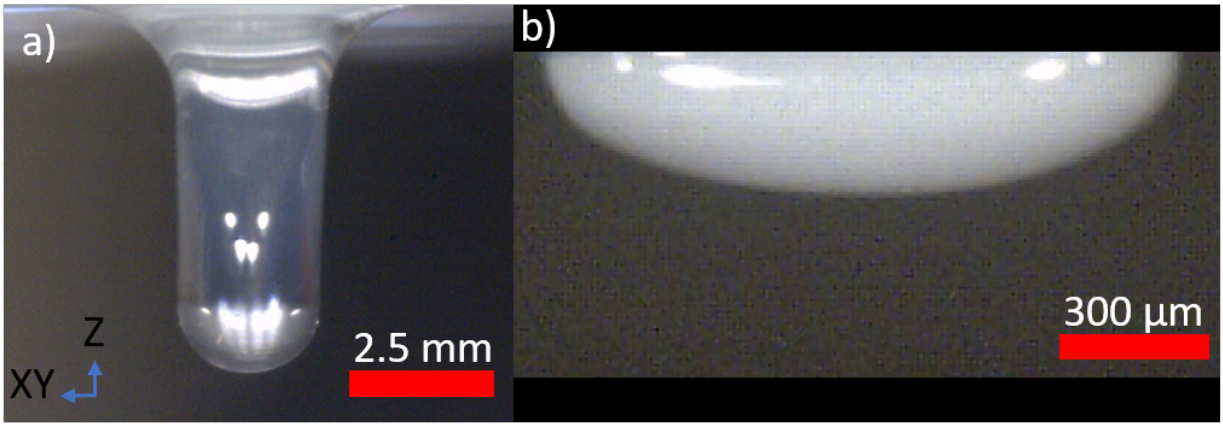

Figure 4.9: a) The experimental cure profile of 0 vol% SBR exposure for 4.5s (102 mJ/cm^2) and b) the experimental cure profile of 25 vol% SBR at 9 s (204 mJ/cm^2).

A substantial reduction of the D_p is observed even at 5 vol% SBR, from 6834 μm (Figure 4.7) to 211 μm (Figure 4.10b). As the SBR loading increases, the D_p decreases, with the exception of the 30 vol% samples. This is potentially caused by colloidal instability from observed particle aggregation, believed to be caused by the relatively high LAP concentration compared to previous latex printing resins[3].

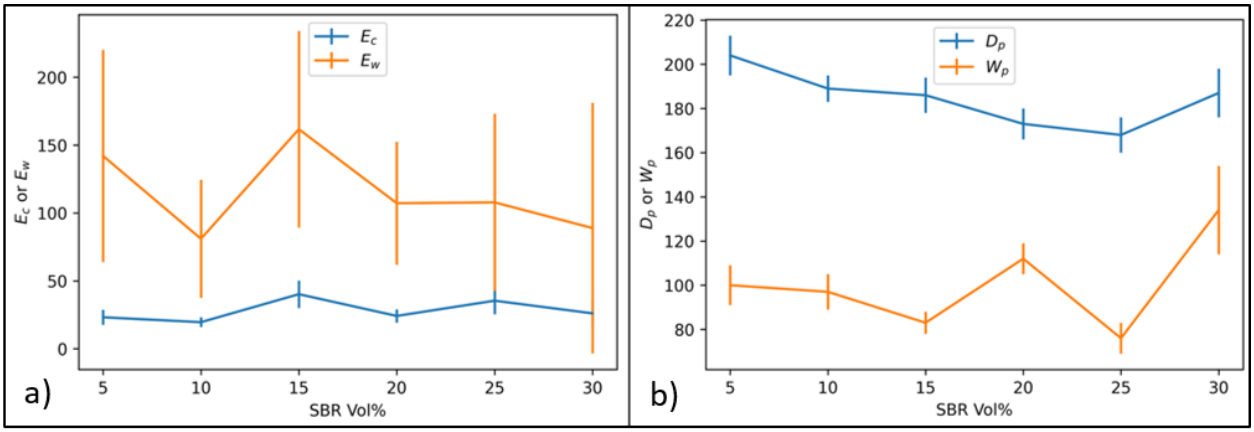

Figure 4.10: Plots of working constants a) critical depth exposure, E_c, critical width exposure, E_w, and b) penetration depth, D_p, and penetration width, W_p, with respect to the SBR vol%. While all working curve constants were expected to decrease with increasing SBR vol%, only D_p displayed a decreasing trend, with the exception of the 30 vol% resin due to colloidal instability.

The authors hypothesized that E_C would also decrease with increasing particle loading due to specific regions of the vat receiving higher exposures due to scattering; however, the light absorption of the particles may be suppressing this effect. Unlike the simulated cure profiles in Figure 4.8 that displayed tapering edges, only a few experimental cure profiles displayed them. The authors hypothesize these features may have been present in potentially all of the experimental data but were destroyed during the cure profile washing and drying steps. This region of the cure profile would likely exhibit low modulus due to the low energy absorbed as shown by the bottom of Figure 4.8 and would be further impacted by oxygen inhibition in experimentally measured profiles. These artifacts may be the result of the high amount of error exhibited in the experimental cure width measurements. Alternatively, it may result from changes in the optical properties of the resin during curing, which was not taken into account in the simulation. However, changes in absorption properties during curing were unable to be measured.

Investigating the curing behavior in the XY direction displays that W_p is less than D_p for all SBR loading cases. This indicates that light is attenuated more in the XY direction compared to the Z, causing faster curing in the Z direction. This is in agreement with E_w values, which are greater than E_c, indicating curing in the Z direction is dominating. Similar to curing in the Z direction, no trends were observed in E_w; however, this could be a result of the large error of the cure profile measurements. The W_p data also exhibits no trend, but mimics the D_p data with a large increase in both values for the 30 vol% SBR case. Causes for the high error are contributed to the rapid drying of the profiles due to the high surface area of the cure profiles. The cure profile width contracts due to water evaporation, shrinking the profiles over short periods of time. This phenomenon will be discussed in greater detail in Section 4.5.5.

4.5.4 Comparison of Simulation and Experimental Results

Figure 4.11 displays the cure depth and cure width of simulated and experimental cure profiles vs the natural log of the exposures applied to the resin surface. The cure depths and widths of the simulated profiles were measured at their thickest and widest section of the cure profiles, respectively. Due to the large variance in experimental cure profile measurements, the lower and upper bounds of the predicted depth and width measurements (created by using the bounds of the $E_{c,0vol\%}$ standard deviation from the neat resin working curve) are shown in Figure 4.11. Despite a constant standard deviation in $E_{c,0vol\%}$, the variation in the simulation predictions is larger at lower SBR volume loading due to reduced light attenuation, enabling deeper cure profiles. The cure widths of simulated cure profiles are generally constant which may be caused by the particle absorption reducing the sensitivity of filled resin to cure width changes.

Comparing the cure depths, the simulation tends to over-predict the thickness and the resulting slope at low-volume loadings. As the volume loading increases, the simulation accuracy improves, with near-perfect accuracy for the 25 vol%. The 30 vol% experimental trials exhibited colloidal destabilization with particle aggregation and separation from the matrix, which causes a large change in resin optical properties that the simulation is not accounting for, and leads to a large prediction error.

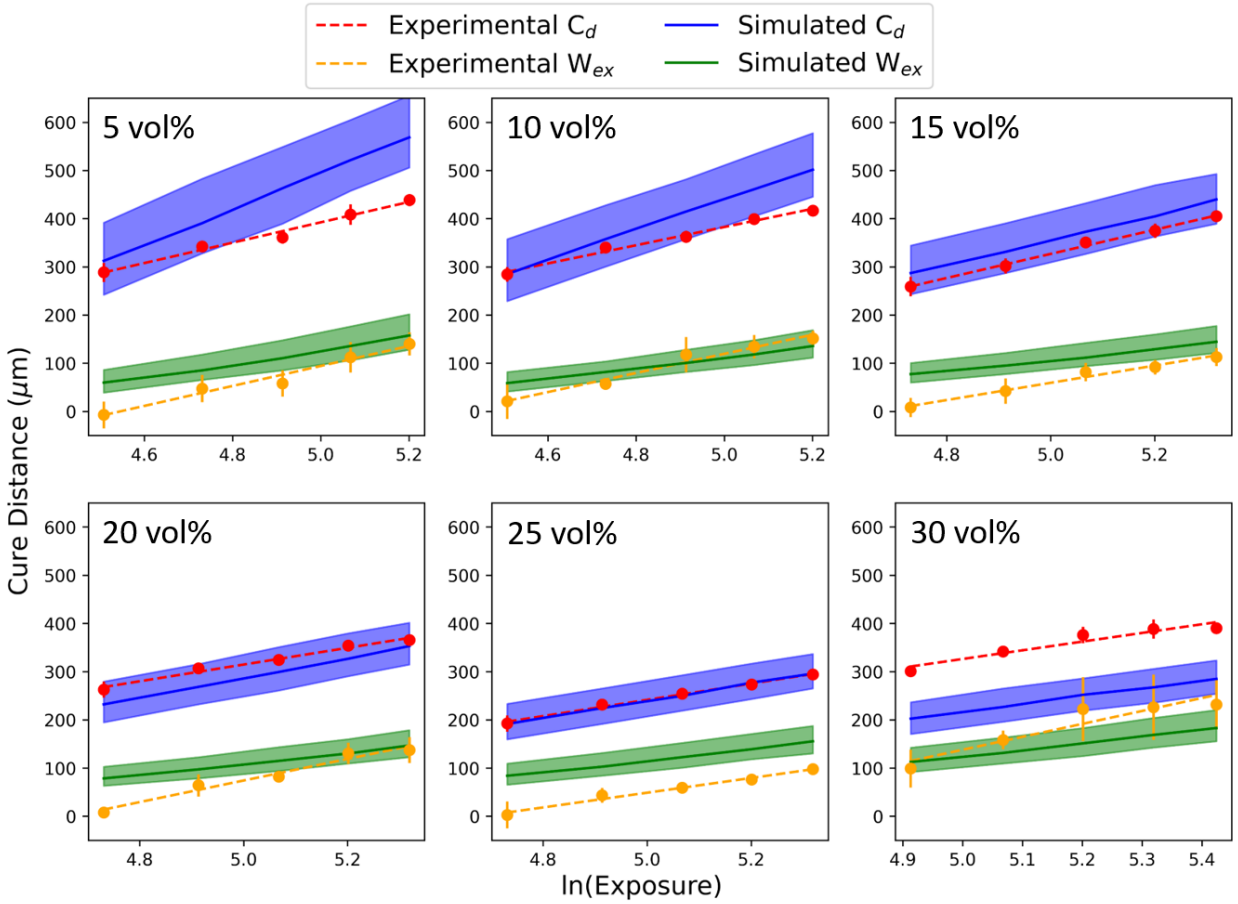

Figure 4.11: Experimental and simulated working curves of cure depth and width of 5 to 30 vol% SBR samples. Error bars on experimental data represent the standard deviation on that particular sample; the aura around the simulated data represents the resulting cure distance of the upper and lower bound of the $E_{c,0vol\%}$ standard deviation.

Comparing cure widths, the simulation consistently over-predicts the value of W_{ex}, with the exception of the 30 vol% samples. The simulation also under-predicts the W_{ex} slope, resulting in poor predictions at low exposures, with accuracy increasing at the higher exposures used.

Figure 4.12 consolidates Figure 4.11 by recording the percent error between the simulation and experimental trial across all exposures for each SBR volume loading. The percent error value corresponds to the simulation accuracy in predicting C_d or W_{ex} on average for a

specific SBR loading. The standard deviation of the percent error is represented by the error bars. Unsurprisingly, the simulation exhibits better accuracy in cure depth predictions with an average of all predictions falling within 20% of the experimental trials, with the exception of the 30 vol% as previously discussed in Section 4.5.3. The standard deviation of the C_d predictions is also much smaller, indicating the simulation performed better at predicting the slope of the working curves (D_p or W_p).

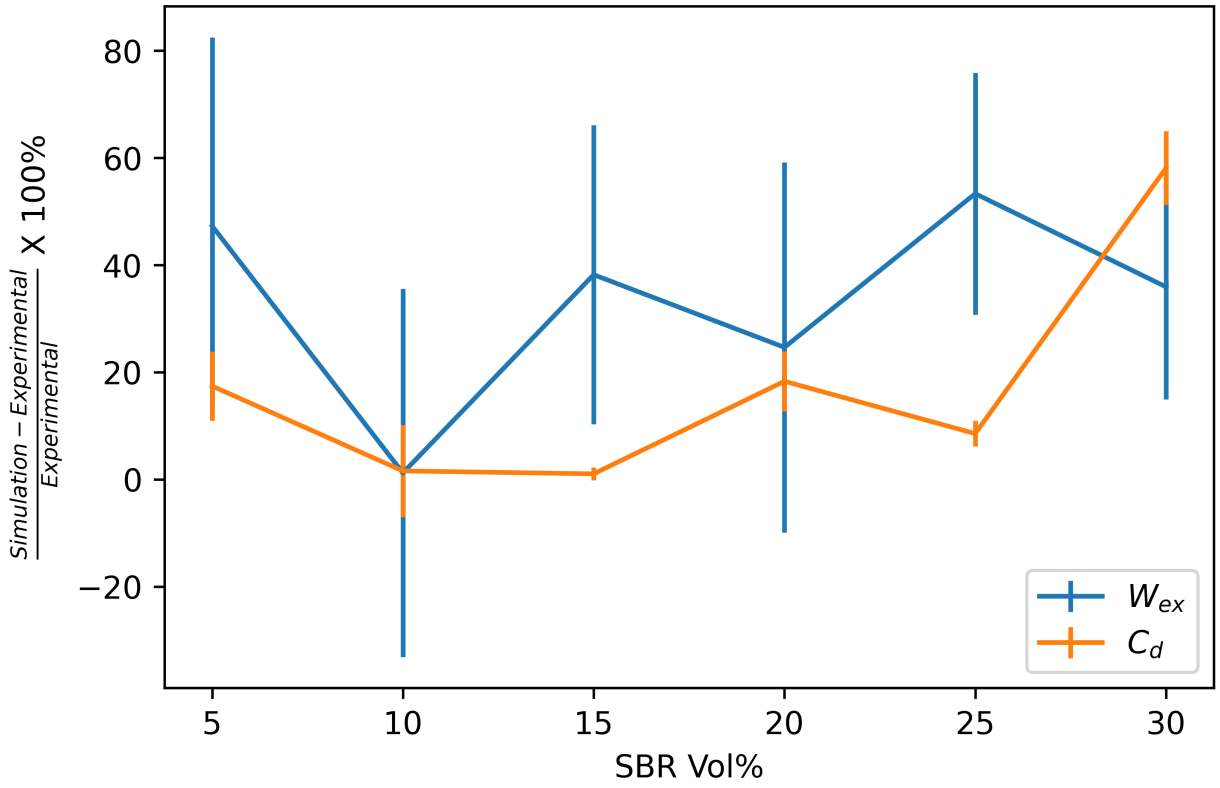

Figure 4.12: Average difference between experimental and mean of simulation data for each vol% sample. No obvious trend in the simulation performance is observed. Error bars represent the standard deviation of differences of each plot in Fig. 4.11.

4.5.5 Discussion

The authors hypothesize that the two largest sources of error result from the neat resin's low absorption (Figure 4.6a) and low cure modulus. The neat resin's low absorption

results in large cure depths exceeding 2-6 mm which is significantly larger than the typical layer height used for VP (50-150 μm). The large cure depths may be causing changes in the resin absorptivity, or optical bleaching, resulting in a non-linearity of the working curve [115]. Compounding the large cure depths with the low modulus of the profiles causes the profiles to deform under low-force events, such as the movement of the glass slide, reducing the accuracy of the cure profile measurements. The combination of the neat resin's large profiles and low cure modulus results in difficult, error-prone cure depth measurements with $\pm$ 500 μm standard deviation (Figure 4.7).

Another source of error is caused by the drying-induced shrinkage of the filled latex-cured profiles. The filled cure profiles are rinsed and the excess water is manually dabbed from the glass slide. The profiles will also quickly dry due to the large surface area and potential additives within the SBR latex. Variations in the water content of the profile alter the swelling and size of the profiles. Differences in the cure profile volume and SBR content will alter the water content and drying rate of the profile.

Other potential causes for discrepancies between the simulated and experimental results could include photocuring phenomena that the simulation does not directly account for, such as oxygen inhibition. Oxygen inhibition plays a large role in the retardation of free radical polymerization, requiring resins to have sufficient photoinitiator concentration to both consume the oxygen present and initiate the polymerization reaction. The resins used in this study contain a low concentration of photoinitiator (0.5 wt%) that is more susceptible to oxygen inhibition effects. The MCRT simulation partially accounts for the oxygen/photoinitiator consumption through the neat resin working curve (Figure 4.7), but as stated above, suffers from other sources of errors. Assuming the neat resin's working curve is accurate, the oxygen and photoinitiator consumption rates may differ due to higher light intensity in the filled resins from light scattering (Figure 4.8).

4.6 Conclusion

Presented is a Monte Carlo ray-trace simulation for predicting the cure profile shape of vat photopolymerization resins containing light-scattering particles. In contrast to other attempts to model similar systems, this simulation utilizes only common experiments to determine material constants and handles all data numerically to easily treat polydisperse particle distributions and non-Gaussian, broad-spectrum light sources. The physical models utilized are universal and are valid for use in any spherical particle-filled resin system. However, predicting the curing behavior of the latex-based (solvent-based) resins results in additional challenges to achieving accurate predictions.

The objective of this work is to demonstrate the prediction of an SBR-filled latex cure profile shape using an MCRT simulation. The MCRT simulation predicts the cure depth and width within two-layer thicknesses (100 μm) on average for all stable colloidal samples. The simulation demonstrated higher accuracy in predicting cure depths (<20% error) compared to cure widths (50% error).

Experimental measurements of the printed low-modulus hydrogel, which shrank during drying due to the included solvent, proved challenging and likely led to experimental measurement errors. Measurement error is expected to be reduced by increasing the photoinitiator concentration and increasing the crosslinker concentration to produce smaller and higher modulus cure profiles.

Improving the measurement of cure profiles and decreasing error in experimental data is crucial to the validation of this simulation and being a viable modeling technique for latex-based resins. Developing latex resins with high colloidal stability allows for an increased concentration of photoinitiator will reduce susceptibility to oxygen inhibition and the cure depth of the neat resin. Additionally, increasing crosslink density by increasing

the concentration of crosslinkers will allow for stiffer cure profiles. Both of these changes in resin composition, if adopted, are hypothesized to decrease the error of the measurements and may result in better agreement with the simulation.

4.7 Funding

This material is based upon work supported by the National Science Foundation under Grant No. 1762712.

4.8 Acknowledgments

The authors owe a debt of gratitude to the Virginia Tech MSE characterization laboratory for access to the Abbe refractometer, the Amanda Morris research group for access to the UV-Vis spectrometer, and MII/ICTAS for access to the DLS. A special thanks to Dr. Lorenzo Pattelli from the European Laboratory for Non-Linear Spectroscopy (LENS) for discussions on light scattering of concentrated colloids.

Chapter 5

Conclusions, Contributions, and Future Work

5.1 Summary

The overall research goal of this dissertation is to improve the printability and processing of performance polymers with vat photopolymerization focusing on solvent-based printing. The research was conducted from two perspectives:

1. Novel vat photopolymerization materials were developed to address the lack of performance materials while maintaining ease of processing.

2. A process simulation was developed to predict the light scattering and photocuring behavior of particle-filled resins.

The results of this work demonstrate a novel polyimide printing platform that maintains low viscosity and is also modular to allow for tunable properties without additional synthetic steps that are capable of printing high-resolution parts. The process simulation demonstrated a high degree of accuracy at low particle volume loadings and utilized only easily acquired experimental inputs. The chapter-wise overview of the conclusions is presented in Sections 5.1.1-5.1.6.

5.1.1 Summary of Chapter 2

Table 5.1: Research Objective (RO) 1 and its developmental objective (DO) and driving research questions (RQ).

RO1	**Investigate the influence of scaffold architecture and monomer composition in polysalt-polyimide resins (Chapter 2)**
RQ1.1	How does incorporating a non-bonded scaffold influence photocuring and the printing of complex parts?
RQ1.2	How does a scaffold with low thermal stability affect burnout and thermal properties?
RQ1.3	How is morphology affected during the imidization protocol?

To address RO1 an ODPA-ODA polyimide polysalt was synthesized through tetra-acid and half-ester routes with a TEGDMA scaffold. The monomers were selected both to study the impact of polarity on solvent retention and resulting imidization, as well as demonstrate the modularity of the polysalt platform when used with an unbound scaffold. Parts were processed up to 400 ^{o}C with some specimens processed stopped at 300 ^{o}C to analyze the post-processing.

5.1.2 RQ 1.1

Both the tetra-acid (ODPAC-ODA) and half-ester (ODPAE-ODA) systems demonstrated photocuring using a photorheometer with crossover time of 7 s and 10 s, respectively, and both materials achieved a plateau storage modulus near 10^5 Pa. Tetra-acid and half-ester resins were printed with 8 s and 12 s exposure times, respectively, and enable solid parts as thick as 3 mm and complex latticed parts to be fabricated.

5.1.3 RQ 1.2

Thermal post-processing removes a large majority of the TEGDMA scaffold with only 3 wt% of the scaffold remaining within the final part processed, determined with TGA. An 8% increase in char yield was observed in the half-ester composition compared to the tetra-acid when processed to 400 ^{o}C. The char yield inequality was also observed in scaffold-free control specimens, lending evidence that the scaffold does not affect the degradation process of the materials. The cause of the increased char yield is attributed to incomplete imidization of the half-ester. The degradation of the half-ester increased the T_g to 380 ^{o}C compared to the tetra-acid T_g of 260 ^{o}. The degradation is likely caused by the reduced polarity of the half-ester resulting in poorer solvent retention and reduced imidization. The lower imidization leaves amide-based repeat units which degrade between 300 and 400 ^{o}C

5.1.4 RQ 1.3

Printed parts are homogeneous and transparent immediately after printing but become opaque within 12 hours of air drying, for thick and latticed part geometries. Once post-processed to 300 ^{o}C both tetra-acid and half-ester thick parts exhibit a connected globular morphology, with each glob containing a micro-nano structured morphology. When processed to 400 ^{o}C, the macro-nano structured morphology disappeared resulting in homogenous globs. Scaffold-free control specimens exhibited similar morphology to printed specimens, with less porosity observed within the lower scale morphology. Interestingly the half-ester latticed parts exhibited a fully homogenous microstructure when processed to 300 and 400 ^{o}C, but the tetra-acid lattice processed to 300 ^{o}C exhibited a highly connected globular morphology similar to the thicker samples. The formation of the morphologies observed is attributed to solvent volatilization during post-processing. Specimens that are thin and/or with lower polarity expel more solvent allowing for less solvent present during post-processing

and reduced porosity.

5.1.5 Summary of Chapter 3

Table 5.2: Research Objective (RO) 2 and its developmental objective (DO) and driving research questions (RQ).

RO2	**Model and predict cure profile shape of ceramic filled resins using Monte Carlo ray tracing simulation (Chapter 3)**
DO2.1	Develop a Monte Carlo ray-tracing simulation to model the light scattering behavior of photocurable resins.
RQ2.2	What is the accuracy of the MCRT simulation when photocuring of ZnO-filled resins?

To address this research objective, first, an MCRT simulation was developed using volume-loading-dependent light-scattering physics to determine how particles scatter the incident light. Rays are launched in the resin and redirected or absorbed each time they collide with a particle, losing energy as they travel through the matrix. This process produces an exposure map that determines regions of cured and uncured resin, revealing the cure profile shape. The MCRT simulation requires inputs of the complex refractive index of the particles and matrix, particle size distribution, and spectral and spatial intensity distribution of the UV source. These variables are used to calculate volume-dependent light scattering terms to simulate light rays and resin absorption to produce a 2D representation of the cure profile shape. Experimental cure profiles are fabricated and imaged to optically measure the depth and width of the cure profile. The simulation predicted the dimensions of ZnO-filled resins cure profiles with a dimensional error of 10% (20 μm) or less for the cure depth and 30% (15 μm) or less for the cure width for particle loadings up to 5 vol% (Figure 3.9 & 3.10). This error corresponds to length scales smaller than a single projected pixel, which is below

the controllable resolution of the printer. This indicates the simulation accurately predicts cure profile shapes and demonstrates this simulation viability for predicting nanocomposite resins that contain low-volume loadings of small particles.

5.1.6 Summary of Chapter 4

Table 5.3: Research Objective (RO) 3 and its developmental objective (DO) and driving research questions (RQ).

RO3	**Model and predict photocuring in light scattering resins (Chapter 4)**
RQ3.1	What is the accuracy of the MCRT simulation when photocuring of latex-based resins?

Latex-based resins have displayed fabrication of high elongation elastomers but struggle to achieve high resolution in VP-based printing due to light scattering. Predicting the light scattering behavior provides a means to improve the resolution and fabricate high-performance parts are VP-relevant resolutions. SBR-latex resin was developed with SBR loadings varying from 5-30 vol%. The MCRT simulation predicted all of the cure depths within 20% (100 μm) or less and cure widths within 50% (100 μm) or less (Figure 4.11 & 4.12). The simulation exhibited higher error compared to the ZnO resins, believed to be caused by the high water content within the latex resin. Once the cure profiles are formed, the water quickly evaporates causing the profiles to shrink and making dimensional measurements inconsistent. Another potential cause of the high error is the low photoinitiator concentration, which reduced the resin matrix absorption, creating large, weak, and difficult cure profiles to measure (Figure 4.7).

5.2 Contributions

5.2.1 Scientific Contributions

The following is a list of scientific contributions that advance the materials development and process corrections to the vat photopolymerization field.

1. **Chapter 2** Investigated the impact of scaffold architecture on polysalt resin

   (a) Unbound scaffold in gel-based resins enables near-complete removal of photocurable scaffold to produce parts with properties uninfluenced by the printing/scaffold process.

   (b) Developed polysalt platform which is modular to print a variety of salt-based monomers, including polyimides and polyamides, without redesigning synthetic strategy.

2. **Chapter 3 4:** Developed a physics-based MCRT simulation to predict the photocuring and light scattering behavior of filled resins. First VP ray-tracing-based simulation to:

   (a) Utilize polydisperse particle size distributions for a more accurate representation of particles with resins.

   (b) Model multichromatic light and projection-based light sources expanding the VP modeling space from laser-based sources.

   (c) leverage volume-dependent light scattering physics through the use of structure factors for more accurate light scattering physics at high particle volume loading.

(d) Use a combination of both sudden and slow death ray tracing techniques in the same simulation to maximize data generated per ray, reducing computational time/resources.

(e) These additions provide a physically accurate representation of the filled resins and light source parameters to accurately predict photocured shape but allow future development for improving printing parameters and printing resolution.

5.2.2 Publications

Chapters 2-4 represent completed, or planned peer-review publications. The title and associated research objective are listed below:

1. **RO 1:** Vat Photopolymerization of ODPA-ODA Polysalt through nonbound scaffolding. *Prepared for submission in Polymer*

2. **RO 3:** Simulating Ceramic Filled Vat Photopolymerization Resins Using Monte Carlo Ray-Tracing. *Prepared for submission in Journal of Applied Optics*

3. **RO 2:** Simulation of Light Scattering in Vat Photopolymerization Latex Resins Using Monte Carlo Ray-Tracing. *Prepared for submission in Additive Manufacturing*

5.2.3 Co-authored Publications

1. Kasprzak, C. R., Brown, J., **Feller, K. D.**, Scott, P. J., Meenakshisundaram, V., Williams, C. B., Long, T. E., (2022). Vat Photopolymerization of Reinforced Styrene-Butadiene Elastomers: A Degradable Scaffold Approach,*ACS Appl. Mater. Interfaces, 14, 16, 18965–1897*

2. White, B. T., Meenakshisundaram, V., **Feller, K. D.**, Williams, C. B., Long, T. E.,

(2021), Vat photopolymerization of unsaturated polyesters utilizing a polymerizable ionic liquid as a non-volatile reactive diluent, *Polymer, 14, 16, 18965–1897*

3. Scott, P. J., Meenakshisundaram, V., Hedge, M., Kasprzak, C. R., Winkler, C. R., **Feller, K. D.**, Williams, C. B., Long, T. E., (2020), 3D Printing Latex: A Route to Complex Geometries of High Molecular Weight Polymers, *ACS Appl. Mater. Interfaces, 12, (9), 10918–1092*

4. Scott, P. J., Kasprzak, C. R., **Feller, K. D.**, Meenakshisundaram, V., Williams, C. B., Long, T. E., (2020) Light and latex: advances in the photochemistry of polymer colloids, *Polym Chem, 11, 3498-3524*

5. Appuhamillage, G. A., Chartrain, N., Meenakshisundaram, V., **Feller, K. D.**, Williams, C. B., Long, T. E., (2019), 110th Anniversary: Vat Photopolymerization-Based Additive Manufacturing: Current Trends and Future Directions in Materials Design, *Ind. Eng. Chem. Res. 58 (33), 15109-15118*

6. Aduba, D. C., **Feller, K. D.**, Long, T. E., Williams, C. B., (2017), A Topological Exploration of Shrinkage in Sintered Bioceramic Parts Fabricated by Vat Photopolymerization, *International Solid Freeform Fabrication Symposium, Conference Proceedings*

5.3 Limitations, Assumptions and Future Work

5.3.1 Polysalt modular platform

The non-bound TEGDMA with ODPA-ODA polysalt is a highly modular platform that could be invaluable to produce a wide variety of printed parts and properties. However, difficulties in the development of the ODPA-ODA polysalt highlight some limitations in the process. The post-processing protocol developed for the polysalt is not optimized with

parts experiencing warpage and cracking potentially due to varying levels of solvent content. Further experimentation is required to optimize the processing steps to fabricate consistent parts. Interestingly, the half-ester-based polyimides underwent partial degradation in both printed and control specimens during imidization. This outcome had a beneficial result of greatly increasing the Tg of printed parts but highlights the lack of exploration of producing non-printed polymers through polysalt precursors.

Future work on the polysalt platform includes further investigation and optimization of the post-processing protocol to reduce part warpage and potentially limit phase separation. Expanding testing to mechanical testing of tensile properties, and exploring the impact of printing on the dielectric properties. Further exploration into the generalizability of this method through testing a wider variety of polyimides, polyamides, and other polysalt-compatible polymers.

5.3.2 Monte Carlo Ray-Tracing Simulation

Like all MCRT simulations, the simulation developed in this dissertation is based on numerous assumptions. The most critical assumption is the assumption of constant material optical properties throughout the exposure. This assumption is valid for the refractive index in the latex-based resin, but the photoinitiator consumption was not accounted for. As the initiator is reacted, the absorption of the material decreases and the light energy traverses farther in the resin. Accounting for this factor in future work is expected to assist in better predictions of the cure width which the simulation tended to under-predict in both the latex and ceramic resins. This addition does require the simulation to be run for each time step, significantly increasing the time for the simulation.

Oxygen inhibition is another factor that may need to be addressed in future iterations of this simulation. Despite the simulation partially accounting for this in the Z-direction, oxygen inhibition varies with dosage. The energy dosage in the XY direction is different potentially resulting in poorer predictions for cure width.

The current simulation relies upon the working curve of the resin to define the criteria of curing based on an exposure value. Using the working curve is very simple to use but can only define curing as a binary value (cured or uncured). However, curing is not a binary property, it is continuous and is frequently related to (storage/loss) modulus. To better capture the contiguous nature of curing, the simulation can utilize photorheological data to relate exposure to modulus. This allows the simulation to output a modulus map instead of an exposure map to better describe the mechanical properties throughout a layer or part. Alternatively, the exposure can be related to reaction conversion through the use of free radical polymerization kinetics-based models[68]. These models do require more experimentation to construct but are simplified through the use of an FTIR-photorheometer to relate exposure, modulus, and conversion together[116]. The simulation currently operates by taking in material properties and a bitmap intensity distribution to output the cure profile shape referred to as the forward model. The simulation in this state is not particularly useful as the cured shape is traditionally a fixed variable that is targeted. A more useful model should output the bitmap intensity distribution, an easily adjusted print parameter, required to photocure the desired layer shape, referred to as the inverse model. This advancement could be achieved by executing the simulation repeatedly making small changes to approach an optimized solution is reached. This methodology is slow, especially for resin systems with low absorption that requires long computational run times.

A faster solution is leveraging a generative adversarial network (GAN). A GAN is a machine-learning method that contains a generator and a discriminator neural network. The generator is trained using the intensity distribution (and material properties) as the input

and cured layer shape as an output, a proxy for the simulation, or a forward model. Simultaneously, the discriminator is trained by using the generated cured layer shape as the input and intensity distribution as the output, the inverse model. This approach is appealing as the simulation can generate a training set of data to train both a forward and inverse model, which are faster than the initial simulation and capable of being applicable to today's VP demands.

5.4 Bibliography

Bibliography

[1] Clay B. Arrington, Maruti Hegde, Viswanath Meenakshisundaram, Joseph M. Dennis, Christopher B. Williams, and Timothy E. Long. Supramolecular Salts for Additive Manufacturing of Polyimides. *ACS Applied Materials and Interfaces*, 13(40):48061–48070, 2021. ISSN 19448252. doi: 10.1021/acsami.1c13493.

[2] Philip J. Scott, Viswanath Meenakshisundaram, Maruti Hegde, Christopher R. Kasprzak, Christopher R. Winkler, Keyton D. Feller, Christopher B. Williams, and Timothy E. Long. 3D Printing Latex: A Route to Complex Geometries of High Molecular Weight Polymers. *ACS Applied Materials Interfaces*, 12(9):10918–10928, mar 2020. ISSN 1944-8244. doi: 10.1021/acsami.9b19986. URL https://pubs.acs.org/doi/10.1021/acsami.9b19986.

[3] Christopher Kasprzak, James R. Brown, Keyton Feller, Philip J. Scott, Viswanath Meenakshisundaram, Chris Williams, and Timothy Long. Vat Photopolymerization of Reinforced Styrene–Butadiene Elastomers: A Degradable Scaffold Approach. *ACS Applied Materials Interfaces*, 14(16):18965–18973, apr 2022. ISSN 1944-8244. doi: 10.1021/acsami.2c03410. URL https://pubs.acs.org/doi/10.1021/acsami.2c03410.

[4] Jill Z. Manapat, Qiyi Chen, Piaoran Ye, and Rigoberto C. Advincula. 3D Printing of Polymer Nanocomposites via Stereolithography. *Macromolecular Materials and Engineering*, 302(9):1600553, sep 2017. ISSN 14387492. doi: 10.1002/mame.201600553. URL https://onlinelibrary.wiley.com/doi/10.1002/mame.201600553.

[5] Witold Nawrot and Karol Malecha. Additive manufacturing revolution in ceramic microsystems. *Microelectronics International*, 37(2):79–85, may 2020. ISSN 1356-5362.

doi: 10.1108/MI-11-2019-0073. URL https://www.emerald.com/insight/content/doi/10.1108/MI-11-2019-0073/full/html.

[6] Maruti Hegde, Viswanath Meenakshisundaram, Nicholas Chartrain, Susheel Sekhar, Danesh Tafti, Christopher B. Williams, and Timothy E. Long. 3D Printing All-Aromatic Polyimides using Mask-Projection Stereolithography: Processing the Nonprocessable. *Advanced Materials*, 29(31):1701240, aug 2017. ISSN 0935-9648. doi: 10.1002/adma.201701240. URL https://onlinelibrary.wiley.com/doi/10.1002/adma.201701240.

[7] Yuxiong Guo, Zhongying Ji, Yun Zhang, Xiaolong Wang, and Feng Zhou. Solvent-free and photocurable polyimide inks for 3d printing. *J. Mater. Chem. A*, 5:16307–16314, 2017. doi: 10.1039/C7TA01952A. URL http://dx.doi.org/10.1039/C7TA01952A.

[8] Yuxiong Guo, Jiawen Xu, Changyou Yan, Yanqiu Chen, Xiaoqin Zhang, Xin Jia, Yu Liu, Xiaolong Wang, and Feng Zhou. Direct Ink Writing of High Performance Architectured Polyimides with Low Dimensional Shrinkage. *Advanced Engineering Materials*, 21(5):1801314, may 2019. ISSN 1438-1656. doi: 10.1002/adem.201801314. URL https://onlinelibrary.wiley.com/doi/10.1002/adem.201801314.

[9] Jana Herzberger, Viswanath Meenakshisundaram, Christopher B. Williams, and Timothy E. Long. 3D Printing All-Aromatic Polyimides Using Stereolithographic 3D Printing of Polyamic Acid Salts. *ACS Macro Letters*, 7(4):493–497, apr 2018. ISSN 2161-1653. doi: 10.1021/acsmacrolett.8b00126. URL https://pubs.acs.org/doi/10.1021/acsmacrolett.8b00126.

[10]

[11] Zhiqiang Liu, Yilun Cai, Feifan Song, Jiajin Li, Jian Zhang, Yi Sun, Guoqiang Luo, and Qiang Shen. Study on chemical graft structure modification and mechanical properties

of photocured polyimide. *ACS Omega*, 7(11):9582–9593, 2022. doi: 10.1021/acsomega.1c06933. URL https://doi.org/10.1021/acsomega.1c06933.

[12] Kejie Wang, Rongzhen Liu, and Chonggao Bao. SiC paste with high curing thickness for stereolithography. *Ceramics International*, 48(19):28692–28703, oct 2022. ISSN 02728842. doi: 10.1016/j.ceramint.2022.06.183. URL https://linkinghub.elsevier.com/retrieve/pii/S0272884222021861.

[13] Keunbada Son, Jung-Ho Lee, and Kyu-Bok Lee. Comparison of Intaglio Surface Trueness of Interim Dental Crowns Fabricated with SLA 3D Printing, DLP 3D Printing, and Milling Technologies. *Healthcare*, 9(8):983, aug 2021. ISSN 2227-9032. doi: 10.3390/healthcare9080983. URL https://www.mdpi.com/2227-9032/9/8/983.

[14] Guojiao Ding, Rujie He, Keqiang Zhang, Niping Zhou, and Hao Xu. Stereolithography 3D printing of SiC ceramic with potential for lightweight optical mirror. *Ceramics International*, 46(11):18785–18790, aug 2020. ISSN 02728842. doi: 10.1016/j.ceramint.2020.04.196. URL https://linkinghub.elsevier.com/retrieve/pii/S0272884220311408.

[15] Xiangquan Wu, Chunjie Xu, and Zhongming Zhang. Preparation and optimization of Si3N4 ceramic slurry for low-cost LCD mask stereolithography. *Ceramics International*, 47(7):9400–9408, apr 2021. ISSN 02728842. doi: 10.1016/j.ceramint.2020.12.072. URL https://linkinghub.elsevier.com/retrieve/pii/S0272884220336701.

[16] Olivier Dufaud, Herve Le Gall, and Serge Corbel. Stereolithography of lead zirconate titanate ceramics for MEMS applications. page 28, apr 2003. doi: 10.1117/12.498777. URL http://proceedings.spiedigitallibrary.org/proceeding.aspx?doi=10.1117/12.498777.

[17] H. Eng, S. Maleksaeedi, S. Yu, Y.Y.C. Choong, F.E. Wiria, C.L.C. Tan, P.C. Su, and J. Wei. 3D Stereolithography of Polymer Composites Reinforced with Orientated Nanoclay. *Procedia Engineering*, 216:1–7, 2017. ISSN 18777058. doi: 10.1016/j.proeng.2018.02.080. URL https://linkinghub.elsevier.com/retrieve/pii/S1877705817333556.

[18] Susan P. Gentry and John W. Halloran. Depth and width of cured lines in photopolymerizable ceramic suspensions. *Journal of the European Ceramic Society*, 33 (10):1981–1988, sep 2013. ISSN 09552219. doi: 10.1016/j.jeurceramsoc.2013.02.033. URL https://linkinghub.elsevier.com/retrieve/pii/S0955221913001386.

[19] Alessandro Bove, Jean-Marc Tulliani, Manuela Galati, and Flaviana Calignano. Investigation of the influence of process parameters on dimensional accuracy and post-sintering crack formation in ceramic 3D printing for porcelain-based commercial resins. *Progress in Additive Manufacturing*, nov 2022. ISSN 2363-9512. doi: 10.1007/s40964-022-00363-x. URL https://link.springer.com/10.1007/s40964-022-00363-x.

[20] Michelle L. Griffith and John W. Halloran. Freeform Fabrication of Ceramics via Stereolithography. *Journal of the American Ceramic Society*, 79(10):2601–2608, aug 2005. ISSN 00027820. doi: 10.1111/j.1151-2916.1996.tb09022.x. URL https://onlinelibrary.wiley.com/doi/10.1111/j.1151-2916.1996.tb09022.x.

[21] K. C. Wu, K. F. Seefeldt, M. J. Solomon, and J. W. Halloran. Prediction of ceramic stereolithography resin sensitivity from theory and measurement of diffusive photon transport. *Journal of Applied Physics*, 98(2):024902, jul 2005. ISSN 0021-8979. doi: 10.1063/1.1980531. URL http://aip.scitation.org/doi/10.1063/1.1980531.

[22] Vladislava Tomeckova and John W. Halloran. Predictive models for the photopoly-

merization of ceramic suspensions. *Journal of the European Ceramic Society*, 30(14): 2833–2840, oct 2010. ISSN 09552219. doi: 10.1016/j.jeurceramsoc.2010.01.027. URL https://linkinghub.elsevier.com/retrieve/pii/S0955221910000415.

[23] Vladislava Tomeckova and John W. Halloran. Critical energy for photopolymerization of ceramic suspensions in acrylate monomers. *Journal of the European Ceramic Society*, 30(16):3273–3282, dec 2010. ISSN 09552219. doi: 10.1016/j.jeurceramsoc.2010.08.003. URL https://linkinghub.elsevier.com/retrieve/pii/S0955221910003778.

[24] J. Tarabeux, V. Pateloup, P. Michaud, and T. Chartier. Development of a numerical simulation model for predicting the curing of ceramic systems in the stereolithography process. *Journal of the European Ceramic Society*, 38(11):4089–4098, sep 2018. ISSN 09552219. doi: 10.1016/j.jeurceramsoc.2018.03.052. URL https://linkinghub.elsevier.com/retrieve/pii/S0955221918301985.

[25] Cheng Sun and Xiang Zhang. The influences of the material properties on ceramic micro-stereolithography. *Sensors and Actuators A: Physical*, 101(3):364–370, oct 2002. ISSN 09244247. doi: 10.1016/S0924-4247(02)00264-9. URL https://linkinghub.elsevier.com/retrieve/pii/S0924424702002649.

[26] M K Ghosh and K L Mittal. *Polyimides : fundamentals and applications*. Marcel Dekker, 1996.

[27] Deyan Kong, Jie Li, Anru Guo, and Xinli Xiao. High temperature electromagnetic shielding shape memory polymer composite. *Chemical Engineering Journal*, 408: 127365, mar 2021. ISSN 13858947. doi: 10.1016/j.cej.2020.127365. URL https://linkinghub.elsevier.com/retrieve/pii/S1385894720334896.

[28] Masatoshi Hasegawa, Zemin Shi, Rikio Yokata, Feifeng He, and Hideo Ozawa. Thermo-processable polyimides with high Tg and high thermo-oxidative stability as derived

from 2,3,3 ,4 -biphenyltetracarboxylic dianhydride. *High Performance Polymers*, 13 (4):355–364, 2001. ISSN 09540083. doi: 10.1088/0954-0083/13/4/312.

[29] Stefan Chisca, Valentina Elena Musteata, Ion Sava, and Maria Bruma. Dielectric behavior of some aromatic polyimide films. *European Polymer Journal*, 47(5):1186–1197, 2011. ISSN 00143057. doi: 10.1016/j.eurpolymj.2011.01.008. URL http://dx.doi.org/10.1016/j.eurpolymj.2011.01.008.

[30] Jian Jun He, Hai Xia Yang, Feng Zheng, and Shi Yong Yang. Dielectric Properties of Fluorinated Aromatic Polyimide Films with Rigid Polymer Backbones. *Polymers*, 14 (3):1–14, 2022. ISSN 20734360. doi: 10.3390/polym14030649.

[31] Der-Jang Liaw, Kung-Li Wang, Ying-Chi Huang, Kueir-Rarn Lee, Juin-Yih Lai, and Chang-Sik Ha. Advanced polyimide materials: Syntheses, physical properties and applications. *Progress in Polymer Science*, 37(7):907–974, jul 2012. ISSN 00796700. doi: 10.1016/j.progpolymsci.2012.02.005. URL https://linkinghub.elsevier.com/retrieve/pii/S0079670012000214.

[32] Hong-jiang Ni, Jin-gang Liu, Zhen-he Wang, and Shi-yong Yang. A review on colorless and optically transparent polyimide films: Chemistry, process and engineering applications. *Journal of Industrial and Engineering Chemistry*, 28:16–27, aug 2015. ISSN 1226086X. doi: 10.1016/j.jiec.2015.03.013. URL https://linkinghub.elsevier.com/retrieve/pii/S1226086X15000854.

[33] M. Hasegawa and K. Horie. Photophysics, photochemistry, and optical properties of polyimides. *Progress in Polymer Science*, 26(2):259–335, mar 2001. ISSN 00796700. doi: 10.1016/S0079-6700(00)00042-3. URL https://linkinghub.elsevier.com/retrieve/pii/S0079670000000423.

[34] Paul M. Hergenrother. The use, design, synthesis, and properties of high performance/high temperature polymers: An overview, 2003. ISSN 09540083.

[35] Daniel A. Rau, Jana Herzberger, Timothy E. Long, and Christopher B. Williams. Ultraviolet-Assisted Direct Ink Write to Additively Manufacture All-Aromatic Polyimides. *ACS Applied Materials Interfaces*, 10(41):34828–34833, oct 2018. ISSN 1944-8244. doi: 10.1021/acsami.8b14584. URL https://pubs.acs.org/doi/10.1021/acsami.8b14584.

[36] Clay B. Arrington, Daniel A. Rau, Christopher B. Williams, and Timothy E. Long. UV-assisted direct ink write printing of fully aromatic Poly(amide imide)s: Elucidating the influence of an acrylic scaffold. *Polymer*, 212:123306, jan 2021. ISSN 00323861. doi: 10.1016/j.polymer.2020.123306. URL https://linkinghub.elsevier.com/retrieve/pii/S0032386120311319.

[37] Bagrat Grigoryan, Daniel W. Sazer, Amanda Avila, Jacob L. Albritton, Aparna Padhye, Anderson H. Ta, Paul T. Greenfield, Don L. Gibbons, and Jordan S. Miller. Development, characterization, and applications of multi-material stereolithography bioprinting. *Scientific Reports*, 11(1):3171, dec 2021. ISSN 2045-2322. doi: 10.1038/s41598-021-82102-w. URL http://www.nature.com/articles/s41598-021-82102-w.

[38] Qiming Chen, Rong Xu, Zitao He, Kejie Zhao, and Liang Pan. Printing 3D Gel Polymer Electrolyte in Lithium-Ion Microbattery Using Stereolithography. *Journal of The Electrochemical Society*, 164(9):A1852–A1857, 2017. ISSN 0013-4651. doi: 10.1149/2.0651709jes. URL https://iopscience.iop.org/article/10.1149/2.0651709jes.

[39] Napolabel B. Palaganas, Joey Dacula Mangadlao, Al Christopher C. de Leon, Jerome O. Palaganas, Katrina D. Pangilinan, Yan Jie Lee, and Rigoberto C. Advin-

cula. 3D Printing of Photocurable Cellulose Nanocrystal Composite for Fabrication of Complex Architectures via Stereolithography. *ACS Applied Materials Interfaces*, 9(39):34314–34324, oct 2017. ISSN 1944-8244. doi: 10.1021/acsami.7b09223. URL https://pubs.acs.org/doi/10.1021/acsami.7b09223.

[40] Yujun Zhang, Yan Wang, Hongwei Duan, Hailin Cao, and Mingyan Zhang. Non-woven Membranes of ODPA-ODA Polyimide Prepared by Electrospinning. In *2007 2nd IEEE International Conference on Nano/Micro Engineered and Molecular Systems*, pages 17–20. IEEE, jan 2007. ISBN 1-4244-0609-9. doi: 10.1109/NEMS.2007.352017. URL http://ieeexplore.ieee.org/document/4160575/.

[41] Dimitris S. Achilias, Maria M. Karabela, and Irini D. Sideridou. Thermal degradation of light-cured dimethacrylate resins. *Thermochimica Acta*, 472(1-2):74–83, jun 2008. ISSN 00406031. doi: 10.1016/j.tca.2008.02.004. URL https://linkinghub.elsevier.com/retrieve/pii/S0040603108000439.

[42] V. N. Rai, Beena Jain, C. Mukherjee, P. Choudhary, Pallavi Saxena, and A. Mishra. Study of degradation behavior in Kapton foil after gamma irradiation at low fluence. *Radiation Effects and Defects in Solids*, 175(9-10):879–891, 2020. ISSN 10294953. doi: 10.1080/10420150.2020.1780593.

[43] Leila S. S. M. Magalhães, Danielle B. Andrade, Roosevelt D. S. Bezerra, Alan I. S. Morais, Francilio C. Oliveira, Márcia S. Rizzo, Edson C. Silva-Filho, and Anderson O. Lobo. Nanocomposite Hydrogel Produced from PEGDA and Laponite for Bone Regeneration. *Journal of Functional Biomaterials*, 13(2), 2022. ISSN 2079-4983. doi: 10.3390/jfb13020053. URL https://www.mdpi.com/2079-4983/13/2/53.

[44] J.M. Cervantes-Uc, J.V. Cauich-Rodríguez, H. Vázquez-Torres, and A. Licea-Claveríe. TGA/FTIR study on thermal degradation of polymethacrylates containing carboxylic

groups. *Polymer Degradation and Stability*, 91(12):3312–3321, dec 2006. ISSN 01413910. doi: 10.1016/j.polymdegradstab.2006.06.005. URL https://linkinghub.elsevier.com/retrieve/pii/S0141391006002072.

[45] Ajay Vasudeo Rane, Lithu Mathew, Krishnan Kanny, Sixberth Mlowe, Neerish Revaprasadu, and Sabu Thomas. Attenuated Total Reflectance Fourier Transform Infrared Spectroscopy: A Tool to Determine Reinforcement of Carbon Black in Polylactic Acid Composites. *Materials Performance and Characterization*, 8(1):20190146, jan 2019. ISSN 23791365. doi: 10.1520/MPC20190146. URL http://www.astm.org/doiLink.cgi?MPC20190146.

[46] Dongxu Pei, Bing Lv, Jianhua Wang, Shengli Qi, Guofeng Tian, and Dezhen Wu. Structure and properties of polyimide aerogels with different skeleton flexibilities. *Soft Materials*, 19(1):50–55, jan 2021. ISSN 1539-445X. doi: 10.1080/1539445X.2020.1740735. URL https://www.tandfonline.com/doi/full/10.1080/1539445X.2020.1740735.

[47] Xiao-Yan Liu, Mao-Sheng Zhan, Yan-Xia Shen, and Kai Wang. Effect of tetraacid on the properties of ODPA/4,4 -ODA polyimide foams. *Journal of Applied Polymer Science*, 119(6):3253–3263, mar 2011. ISSN 00218995. doi: 10.1002/app.32899. URL https://onlinelibrary.wiley.com/doi/10.1002/app.32899.

[48] Yongkang Bai, Long Mao, and Yuejun Liu. High temperature shape memory polyimide ionomer. *Journal of Applied Polymer Science*, 133(30):2–9, 2016. ISSN 10974628. doi: 10.1002/app.43630.

[49] Kadir Demirelli, Esin Kaya, Mehmet Coşkun, and Eyüp Bağci. Thermal degradation of two different polymers bearing amide pendant groups prepared by ATRP method.

Journal of Thermal Analysis and Calorimetry, 114(2):917–926, nov 2013. ISSN 1388-6150. doi: 10.1007/s10973-013-2986-6. URL http://link.springer.com/10.1007/s10973-013-2986-6.

[50] M.-J. Brekner and C. Feger. Curing studies of a polyimide precursor. *Journal of Polymer Science Part A: Polymer Chemistry*, 25(7):2005–2020, jul 1987. ISSN 0887624X. doi: 10.1002/pola.1987.080250720. URL https://onlinelibrary.wiley.com/doi/10.1002/pola.1987.080250720.

[51] Michael-Joachim Brekner and Claudius Feger. Curing studies of a polyimide precursor. II. Polyamic acid. *Journal of Polymer Science Part A: Polymer Chemistry*, 25(9):2479–2491, sep 1987. ISSN 0887624X. doi: 10.1002/pola.1987.080250913. URL https://onlinelibrary.wiley.com/doi/10.1002/pola.1987.080250913.

[52] Claudius Feger. Curing of polyimides. *Polymer Engineering and Science*, 29(5):347–351, mar 1989. ISSN 0032-3888. doi: 10.1002/pen.760290514. URL https://onlinelibrary.wiley.com/doi/10.1002/pen.760290514.

[53] Gayan A. Appuhamillage, Nicholas Chartrain, Viswanath Meenakshisundaram, Keyton D. Feller, Christopher B. Williams, and Timothy E. Long. 110th Anniversary : Vat Photopolymerization-Based Additive Manufacturing: Current Trends and Future Directions in Materials Design. *Industrial Engineering Chemistry Research*, 58(33):15109–15118, aug 2019. ISSN 0888-5885. doi: 10.1021/acs.iecr.9b02679. URL https://pubs.acs.org/doi/10.1021/acs.iecr.9b02679.

[54] Anh-Vu Do, Behnoush Khorsand, Sean M. Geary, and Aliasger K. Salem. 3D Printing of Scaffolds for Tissue Regeneration Applications. *Advanced Healthcare Materials*, 4(12):1742–1762, aug 2015. ISSN 21922640. doi: 10.1002/adhm.201500168. URL https://onlinelibrary.wiley.com/doi/10.1002/adhm.201500168.

[55] Xuan Zhou, Nathan J. Castro, Wei Zhu, Haitao Cui, Mitra Aliabouzar, Kausik Sarkar, and Lijie Grace Zhang. Improved Human Bone Marrow Mesenchymal Stem Cell Osteogenesis in 3D Bioprinted Tissue Scaffolds with Low Intensity Pulsed Ultrasound Stimulation. *Scientific Reports*, 6(1):32876, dec 2016. ISSN 2045-2322. doi: 10.1038/srep32876. URL http://www.nature.com/articles/srep32876.

[56] Vitor M. Correlo, Luciano F. Boesel, Mrinal Bhattacharya, Joao F. Mano, Nuno M. Neves, and Ruis L. Reis. Hydroxyapatite Reinforced Chitosan and Polyester Blends for Biomedical Applications. *Macromolecular Materials and Engineering*, 290(12): 1157–1165, dec 2005. ISSN 1438-7492. doi: 10.1002/mame.200500163. URL https://onlinelibrary.wiley.com/doi/10.1002/mame.200500163.

[57] Hyun-Wook Kang and Dong-Woo Cho. Development of an Indirect Stereolithography Technology for Scaffold Fabrication with a Wide Range of Biomaterial Selectivity. *Tissue Engineering Part C: Methods*, 18(9):719–729, sep 2012. ISSN 1937-3384. doi: 10.1089/ten.tec.2011.0621. URL https://www.liebertpub.com/doi/10.1089/ten.tec.2011.0621.

[58] Reymark D. Maalihan, Bryan B. Pajarito, and Rigoberto C. Advincula. 3D-printing methacrylate/chitin nanowhiskers composites via stereolithography: Mechanical and thermal properties. *Materials Today: Proceedings*, 33:1819–1824, 2020. ISSN 22147853. doi: 10.1016/j.matpr.2020.05.063. URL https://linkinghub.elsevier.com/retrieve/pii/S2214785320336191.

[59] Yuchao Wu, Chao Li, Tingting Chen, Renhui Qiu, and Wendi Liu. Photo-curing 3D printing of micro-scale bamboo fibers reinforced palm oil-based thermosets composites. *Composites Part A: Applied Science and Manufacturing*, 152:106676, jan 2022.

ISSN 1359835X. doi: 10.1016/j.compositesa.2021.106676. URL https://linkinghub.elsevier.com/retrieve/pii/S1359835X21003936.

[60] Qiming Wang, Julie A. Jackson, Qi Ge, Jonathan B. Hopkins, Christopher M. Spadaccini, and Nicholas X. Fang. Lightweight Mechanical Metamaterials with Tunable Negative Thermal Expansion. *Physical Review Letters*, 117(17):175901, oct 2016. ISSN 0031-9007. doi: 10.1103/PhysRevLett.117.175901. URL https://link.aps.org/doi/10.1103/PhysRevLett.117.175901.

[61] Caterina Credi, Alessandro Fiorese, Marco Tironi, Roberto Bernasconi, Luca Magagnin, Marinella Levi, and Stefano Turri. 3D Printing of Cantilever-Type Microstructures by Stereolithography of Ferromagnetic Photopolymers. *ACS Applied Materials Interfaces*, 8(39):26332–26342, oct 2016. ISSN 1944-8244. doi: 10.1021/acsami.6b08880. URL https://pubs.acs.org/doi/10.1021/acsami.6b08880.

[62] S J Leigh, C P Purssell, D R Billson, and D A Hutchins. Using a magnetite/thermoplastic composite in 3D printing of direct replacements for commercially available flow sensors. *Smart Materials and Structures*, 23(9):095039, sep 2014. ISSN 0964-1726. doi: 10.1088/0964-1726/23/9/095039. URL https://iopscience.iop.org/article/10.1088/0964-1726/23/9/095039.

[63] Hyung-Mun Yun, Su-Jin Ahn, Kyung-Ran Park, Mi-Joo Kim, Jung-Ju Kim, Guang-Zhen Jin, Hae-Won Kim, and Eun-Cheol Kim. Magnetic nanocomposite scaffolds combined with static magnetic field in the stimulation of osteoblastic differentiation and bone formation. *Biomaterials*, 85:88–98, apr 2016. ISSN 01429612. doi: 10.1016/j.biomaterials.2016.01.035. URL https://linkinghub.elsevier.com/retrieve/pii/S0142961216000491.

[64] John W Halloran. Ceramic Stereolithography: Additive Manufacturing for Ce-

ramics by Photopolymerization. *Annual Review of Materials Research*, 46(1): 19–40, jul 2016. ISSN 1531-7331. doi: 10.1146/annurev-matsci-070115-031841. URL www.annualreviews.orghttp://www.annualreviews.org/doi/10.1146/annurev-matsci-070115-031841.

[65] Anton Sotov, Artem Kantyukov, Anatoly Popovich, and Vadim Sufiiarov. LCD-SLA 3D printing of BaTiO3 piezoelectric ceramics. *Ceramics International*, 47(21):30358–30366, nov 2021. ISSN 02728842. doi: 10.1016/j.ceramint.2021.07.216. URL https://linkinghub.elsevier.com/retrieve/pii/S0272884221022550.

[66] Tara Tariverdian, Aliasghar Behnamghader, Peiman Brouki Milan, Hadi Barzegar-Bafrooei, and Masoud Mozafari. 3D-printed barium strontium titanate-based piezoelectric scaffolds for bone tissue engineering. *Ceramics International*, 45(11):14029–14038, aug 2019. ISSN 02728842. doi: 10.1016/j.ceramint.2019.04.102. URL https://linkinghub.elsevier.com/retrieve/pii/S0272884219309277.

[67] Xuan Song, Zeyu Chen, Liwen Lei, Kirk Shung, Qifa Zhou, and Yong Chen. Piezoelectric component fabrication using projection-based stereolithography of barium titanate ceramic suspensions. *Rapid Prototyping Journal*, 23(1):44–53, jan 2017. ISSN 1355-2546. doi: 10.1108/RPJ-11-2015-0162. URL https://www.emerald.com/insight/content/doi/10.1108/RPJ-11-2015-0162/full/html.

[68] Jim H. Lee, Robert K. Prud'homme, and Ilhan A. Aksay. Cure depth in photopolymerization: Experiments and theory. *Journal of Materials Research*, 16(12): 3536–3544, dec 2001. ISSN 0884-2914. doi: 10.1557/JMR.2001.0485. URL http://link.springer.com/10.1557/JMR.2001.0485.

[69] Michelle L. Griffith and John W. Halloran. Freeform fabrication of ceramics via stereolithography. *Journal of the American Ceramic Society*, 79(10):2601–2608, 1996.

doi: https://doi.org/10.1111/j.1151-2916.1996.tb09022.x. URL https://ceramics.onlinelibrary.wiley.com/doi/abs/10.1111/j.1151-2916.1996.tb09022.x.

[70] J. Robert Mahan. *The Monte Carlo Ray-Trace Method in Radiation Heat Transfer and Applied Optics*. Wiley Sons Ltd and ASME Press, 2019.

[71] C. Sun and X. Zhang. Experimental and numerical investigations on microstereolithography of ceramics. *Journal of Applied Physics*, 92(8):4796–4802, oct 2002. ISSN 0021-8979. doi: 10.1063/1.1503410. URL http://aip.scitation.org/doi/10.1063/1.1503410.

[72] L. Bressel and O. Reich. Theoretical and experimental study of the diffuse transmission of light through highly concentrated absorbing and scattering materials. *Journal of Quantitative Spectroscopy and Radiative Transfer*, 146:190–198, oct 2014. ISSN 00224073. doi: 10.1016/j.jqsrt.2014.01.007. URL https://linkinghub.elsevier.com/retrieve/pii/S0022407314000168.

[73] Robert Botet, Sylvie Kwok, and Bernard Cabane. Percus–Yevick structure factors made simple. *Journal of Applied Crystallography*, 53(6):1570–1582, dec 2020. ISSN 1600-5767. doi: 10.1107/S1600576720014041. URL https://scripts.iucr.org/cgi-bin/paper?S1600576720014041.

[74] Christian Mätzler. MATLAB Functions for Mie Scattering and Absorption. Technical Report July 2002, 2002. URL http://arrc.ou.edu/$\sim$rockee/NRA_2007_website/Mie-scattering-Matlab.pdf.

[75] L. Miao, S. Tanemura, M. Tanemura, S. P. Lau, and B. K. Tay. Thickness-dependent optical properties of ZnO thin films. *Journal of Materials Science: Materials in Electronics*, 18(S1):343–346, oct 2007. ISSN 0957-4522. doi: 10.1007/s10854-007-9243-3. URL http://link.springer.com/10.1007/s10854-007-9243-3.

[76] M. H. Shachar, G. Uahengo, E. H. Penilla, Y. Kodera, and J. E. Garay. Modeling the effects of scattering and absorption on the transmission of light in polycrystalline materials. *Journal of Applied Physics*, 128(8):083103, aug 2020. ISSN 0021-8979. doi: 10.1063/5.0014937. URL http://aip.scitation.org/doi/10.1063/5.0014937.

[77] H.N. Yoshimura and H. Goldenstein. Light scattering in polycrystalline alumina with bi-dimensionally large surface grains. *Journal of the European Ceramic Society*, 29(2): 293–303, jan 2009. ISSN 09552219. doi: 10.1016/j.jeurceramsoc.2008.03.008. URL https://linkinghub.elsevier.com/retrieve/pii/S0955221908001453.

[78] F. Choueikani, F. Royer, S. Douadi, A. Skora, D. Jamon, D. Blanc, and A. Siblini. Low birefringent magneto-optical waveguides fabricated via organic-inorganic sol-gel process. *The European Physical Journal Applied Physics*, 47(3):30401, sep 2009. ISSN 1286-0042. doi: 10.1051/epjap/2009096. URL http://www.epjap.org/10.1051/epjap/2009096.

[79] Andreas Erdmann, Clifford L. Henderson, and C. Grant Willson. Impact of exposure induced refractive index changes of photoresists on the photolithographic process. *Journal of Applied Physics*, 89(12):8163–8168, jun 2001. ISSN 0021-8979. doi: 10.1063/1.1359165. URL http://aip.scitation.org/doi/10.1063/1.1359165.

[80] D Kong, M Michihata, K Takamasu, and S Takahashi. In-Process Measurement of Resin's Curing Degree in Micro-Stereolithography Using Internal Reflection at Critical angle. *Journal of Physics: Conference Series*, 1065:142024, aug 2018. ISSN 1742-6588. doi: 10.1088/1742-6596/1065/14/142024. URL https://iopscience.iop.org/article/10.1088/1742-6596/1065/14/142024.

[81] Rolf Apetz and Michel P. B. Bruggen. Transparent Alumina: A Light-Scattering Model. *Journal of the American Ceramic Society*, 86(3):480–486, mar 2003. ISSN

00027820. doi: 10.1111/j.1151-2916.2003.tb03325.x. URL https://onlinelibrary.wiley.com/doi/10.1111/j.1151-2916.2003.tb03325.x.

[82] Jin Woo Lee, GeunSeon Ahn, Dae Shick Kim, and Dong-Woo Cho. Development of nano- and microscale composite 3D scaffolds using PPF/DEF-HA and micro-stereolithography. *Microelectronic Engineering*, 86(4-6):1465–1467, apr 2009. ISSN 01679317. doi: 10.1016/j.mee.2008.12.038. URL https://linkinghub.elsevier.com/retrieve/pii/S0167931708006473.

[83] A. Ronca, L. Ambrosio, and D.W. Grijpma. Preparation of designed poly(d,l-lactide)/nanosized hydroxyapatite composite structures by stereolithography. *Acta Biomaterialia*, 9(4):5989–5996, apr 2013. ISSN 17427061. doi: 10.1016/j.actbio.2012.12.004. URL https://linkinghub.elsevier.com/retrieve/pii/S1742706112005880.

[84] Mike A. Geven, Viktor Varjas, Lukas Kamer, Xinjiang Wang, Jiang Peng, David Eglin, and Dirk W. Grijpma. Fabrication of patient specific composite orbital floor implants by stereolithography. *Polymers for Advanced Technologies*, 26(12):1433–1438, dec 2015. ISSN 10427147. doi: 10.1002/pat.3589. URL http://doi.wiley.com/10.1002/pat.3589.

[85] John J.A. Barry, Alexandr V. Evseev, Mikhail A. Markov, Clare E. Upton, Colin A. Scotchford, Vladimir K. Popov, and Steven M. Howdle. In vitro study of hydroxyapatite-based photocurable polymer composites prepared by laser stereolithography and supercritical fluid extraction. *Acta Biomaterialia*, 4(6):1603–1610, nov 2008. ISSN 17427061. doi: 10.1016/j.actbio.2008.05.024. URL https://linkinghub.elsevier.com/retrieve/pii/S1742706108001402.

[86] Kanguk Kim, Wei Zhu, Xin Qu, Chase Aaronson, William R. McCall, Shaochen Chen,

and Donald J. Sirbuly. 3D Optical Printing of Piezoelectric Nanoparticle–Polymer Composite Materials. *ACS Nano*, 8(10):9799–9806, oct 2014. ISSN 1936-0851. doi: 10.1021/nn503268f. URL https://pubs.acs.org/doi/10.1021/nn503268f.

[87] J. H. Sandoval, K. F. Soto, L. E. Murr, and R. B. Wicker. Nanotailoring photocrosslinkable epoxy resins with multi-walled carbon nanotubes for stereolithography layered manufacturing. *Journal of Materials Science*, 42(1):156–165, jan 2007. ISSN 0022-2461. doi: 10.1007/s10853-006-1035-2. URL http://link.springer.com/10.1007/s10853-006-1035-2.

[88] Dong Lin, Shengyu Jin, Feng Zhang, Chao Wang, Yiqian Wang, Chi Zhou, and Gary J Cheng. 3D stereolithography printing of graphene oxide reinforced complex architectures. *Nanotechnology*, 26(43):434003, oct 2015. ISSN 0957-4484. doi: 10.1088/0957-4484/26/43/434003. URL https://iopscience.iop.org/article/10.1088/0957-4484/26/43/434003.

[89] Sandeep Kumar, Manfred Hofmann, Bettina Steinmann, E. Johan Foster, and Christoph Weder. Reinforcement of Stereolithographic Resins for Rapid Prototyping with Cellulose Nanocrystals. *ACS Applied Materials Interfaces*, 4(10):5399–5407, oct 2012. ISSN 1944-8244. doi: 10.1021/am301321v. URL https://pubs.acs.org/doi/10.1021/am301321v.

[90] Yuanyuan Zhang, Houmin Li, Xi Yang, Tao Zhang, Kaiqiang Zhu, Wei Si, Zhenliang Liu, and Houjun Sun. Additive manufacturing of carbon nanotube-photopolymer composite radar absorbing materials. *Polymer Composites*, 39(S2):E671–E676, may 2018. ISSN 02728397. doi: 10.1002/pc.24117. URL http://doi.wiley.com/10.1002/pc.24117.

[91] U. Kalsoom, A. Peristyy, P. N. Nesterenko, and B. Paull. A 3D printable diamond

polymer composite: a novel material for fabrication of low cost thermally conducting devices. *RSC Advances*, 6(44):38140–38147, 2016. ISSN 2046-2069. doi: 10.1039/C6RA05261D. URL http://xlink.rsc.org/?DOI=C6RA05261D.

[92] S.J. Leigh, C.P. Purssell, J. Bowen, D.A. Hutchins, J.A. Covington, and D.R. Billson. A miniature flow sensor fabricated by micro-stereolithography employing a magnetite/acrylic nanocomposite resin. *Sensors and Actuators A: Physical*, 168(1): 66–71, jul 2011. ISSN 09244247. doi: 10.1016/j.sna.2011.03.058. URL https://linkinghub.elsevier.com/retrieve/pii/S0924424711002287.

[93] Lu Lu, Ping Guo, and Yayue Pan. Magnetic-Field-Assisted Projection Stereolithography for Three-Dimensional Printing of Smart Structures. *Journal of Manufacturing Science and Engineering*, 139(7), jul 2017. ISSN 1087-1357. doi: 10.1115/1.4035964. URL https://asmedigitalcollection.asme.org/manufacturingscience/article/doi/10.1115/1.4035964/454620/MagneticFieldAssisted-Projection-Stereolithography.

[94] Yao Liu, Lijin Cheng, Hao Li, Qing Li, Yuan Shi, Fei Liu, Qiumei Wu, and Shaojun Liu. Formation mechanism of stereolithography of Si3N4 slurry using silane coupling agent as modifier and dispersant. *Ceramics International*, 46(10):14583–14590, jul 2020. ISSN 02728842. doi: 10.1016/j.ceramint.2020.02.258. URL https://linkinghub.elsevier.com/retrieve/pii/S0272884220305848.

[95] P.J. Bartolo and J. Gaspar. Metal filled resin for stereolithography metal part. *CIRP Annals*, 57(1):235–238, 2008. ISSN 00078506. doi: 10.1016/j.cirp.2008.03.124. URL https://linkinghub.elsevier.com/retrieve/pii/S0007850608000942.

[96] Marilyne Roumanie, Cécile Flassayer, Adrien Resch, Laurent Cortella, and Richard Laucournet. Influence of debinding and sintering conditions on the composition

and thermal conductivity of copper parts printed from highly loaded photocurable formulations. *SN Applied Sciences*, 3(1), 2021. ISSN 2523-3963. doi: 10.1007/s42452-020-04049-3. URL https://doi.org/10.1007/s42452-020-04049-3.

[97] Z Chen, D Li, W Zhou, and L Wang. Curing characteristics of ceramic stereolithography for an aqueous-based silica suspension. *Proceedings of the Institution of Mechanical Engineers, Part B: Journal of Engineering Manufacture*, 224 (4):641–651, apr 2010. ISSN 0954-4054. doi: 10.1243/09544054JEM1751. URL http://journals.sagepub.com/doi/10.1243/09544054JEM1751.

[98] Charles Manière, Gabriel Kerbart, Christelle Harnois, and Sylvain Marinel. Modeling sintering anisotropy in ceramic stereolithography of silica. *Acta Materialia*, 182:163–171, jan 2020. ISSN 13596454. doi: 10.1016/j.actamat.2019.10.032. URL https://linkinghub.elsevier.com/retrieve/pii/S1359645419306949.

[99] C. Esposito Corcione, A. Greco, F. Montagna, A. Licciulli, and A. Maffezzoli. Silica moulds built by stereolithography. *Journal of Materials Science*, 40(18):4899–4904, sep 2005. ISSN 0022-2461. doi: 10.1007/s10853-005-3888-1. URL http://link.springer.com/10.1007/s10853-005-3888-1.

[100] T. Chartier, A. Badev, Y. Abouliatim, P. Lebaudy, and L. Lecamp. Stereolithography process: Influence of the rheology of silica suspensions and of the medium on polymerization kinetics – Cured depth and width. *Journal of the European Ceramic Society*, 32(8):1625–1634, jul 2012. ISSN 09552219. doi: 10.1016/j.jeurceramsoc.2012.01.010. URL https://linkinghub.elsevier.com/retrieve/pii/S0955221912000246.

[101] C. Hinczewski, S. Corbel, and T. Chartier. Stereolithography for the fabrication of ceramic three- dimensional parts. *Rapid Prototyping Journal*, 4(3):104–111, sep 1998.

ISSN 1355-2546. doi: 10.1108/13552549810222867. URL https://www.emerald.com/insight/content/doi/10.1108/13552549810222867/full/html.

[102] Emil Johansson, Oscar Lidström, Jan Johansson, Ola Lyckfeldt, and Erik Adolfsson. Influence of Resin Composition on the Defect Formation in Alumina Manufactured by Stereolithography. *Materials*, 10(2):138, feb 2017. ISSN 1996-1944. doi: 10.3390/ma10020138. URL http://www.mdpi.com/1996-1944/10/2/138.

[103] Soshu Kirihara and Toshiki Niki. Three-Dimensional Stereolithography of Alumina Photonic Crystals for Terahertz Wave Localization. *International Journal of Applied Ceramic Technology*, 12(1):32–37, jan 2015. ISSN 1546542X. doi: 10.1111/ijac.12320. URL http://doi.wiley.com/10.1111/ijac.12320.

[104] Haidong Wu, Wei Liu, Rongxuan He, Ziwei Wu, Qiangguo Jiang, Xuan Song, Yong Chen, Lixia Cheng, and Shanghua Wu. Fabrication of dense zirconia-toughened alumina ceramics through a stereolithography-based additive manufacturing. *Ceramics International*, 43(1):968–972, jan 2017. ISSN 02728842. doi: 10.1016/j.ceramint.2016.10.027. URL https://linkinghub.elsevier.com/retrieve/pii/S027288421631776X.

[105] Rongxuan He, Wei Liu, Ziwei Wu, Di An, Meipeng Huang, Haidong Wu, Qiangguo Jiang, Xuanrong Ji, Shanghua Wu, and Zhipeng Xie. Fabrication of complex-shaped zirconia ceramic parts via a DLP- stereolithography-based 3D printing method. *Ceramics International*, 44(3):3412–3416, feb 2018. ISSN 02728842. doi: 10.1016/j.ceramint.2017.11.135. URL https://linkinghub.elsevier.com/retrieve/pii/S0272884217325932.

[106] Xingbang Li, He Zhong, Jingxian Zhang, Yusen Duan, Hainan Bai, Jingjing Li, and Dongliang Jiang. Dispersion and properties of zirconia suspensions for stereolithogra-

phy. *International Journal of Applied Ceramic Technology*, 17(1):239–247, jan 2020. ISSN 1546-542X. doi: 10.1111/ijac.13321. URL https://onlinelibrary.wiley.com/doi/abs/10.1111/ijac.13321.

[107] Jinjin Zhang, Luyang Wei, Xiuxia Meng, Fangyong Yu, Naitao Yang, and Shaomin Liu. Digital light processing-stereolithography three-dimensional printing of yttria-stabilized zirconia. *Ceramics International*, 46(7):8745–8753, may 2020. ISSN 02728842. doi: 10.1016/j.ceramint.2019.12.113. URL https://linkinghub.elsevier.com/retrieve/pii/S0272884219336028.

[108] Kai Liu, Kai Zhang, David L. Bourell, Fangjie Chen, Huajun Sun, Yusheng Shi, Jiang Wang, Mengqiang He, and Jiaqi Chen. Gelcasting of zirconia-based all-ceramic teeth combined with stereolithography. *Ceramics International*, 44(17): 21556–21563, dec 2018. ISSN 02728842. doi: 10.1016/j.ceramint.2018.08.219. URL https://linkinghub.elsevier.com/retrieve/pii/S0272884218322958.

[109] Marta Revilla-León, Mohammad Mujtaba Methani, Dean Morton, and Amirali Zandinejad. Internal and marginal discrepancies associated with stereolithography (SLA) additively manufactured zirconia crowns. *The Journal of Prosthetic Dentistry*, 124(6):730–737, dec 2020. ISSN 00223913. doi: 10.1016/j.prosdent.2019.09.018. URL https://linkinghub.elsevier.com/retrieve/pii/S0022391319306109.

[110] Cheng Sun and Xiang Zhang. The influences of the material properties on ceramic micro-stereolithography. *Sensors and Actuators A: Physical*, 101(3):364–370, oct 2002. ISSN 09244247. doi: 10.1016/S0924-4247(02)00264-9. URL https://linkinghub.elsevier.com/retrieve/pii/S0924424702002649.

[111] C. Sun and X. Zhang. Experimental and numerical investigations on microstereolithography of ceramics. *Journal of Applied Physics*, 92(8):4796–4802, oct 2002. ISSN 0021-

8979. doi: 10.1063/1.1503410. URL http://aip.scitation.org/doi/10.1063/1.1503410.

[112] Paul F Jacobs. *Fundamentals of Stereolithography*. Number July. International Solid Freeform Fabrication Symposium, 1992. ISBN 0-87263-425-6.

[113] Benjamin D. Fairbanks, Michael P. Schwartz, Christopher N. Bowman, and Kristi S. Anseth. Photoinitiated polymerization of PEG-diacrylate with lithium phenyl-2,4,6-trimethylbenzoylphosphinate: polymerization rate and cytocompatibility. *Biomaterials*, 30(35):6702–6707, dec 2009. ISSN 01429612. doi: 10.1016/j.biomaterials.2009.08.055. URL https://linkinghub.elsevier.com/retrieve/pii/S0142961209009041.

[114] Aurelia Arnold, Irving Madorsky, and Lawrence A. Wood. Measurement of Refractive Index of Elastomers. *Rubber Chemistry and Technology*, 25(3):693–699, sep 1952. ISSN 1943-4804. doi: 10.5254/1.3543432. URL https://meridian.allenpress.com/rct/article/25/3/693/89560/Measurement-of-Refractive-Index-of-Elastomers.

[115] Joe Bennett. Measuring UV curing parameters of commercial photopolymers used in additive manufacturing. *Additive Manufacturing*, 18:203–212, dec 2017. ISSN 22148604. doi: 10.1016/j.addma.2017.10.009. URL https://linkinghub.elsevier.com/retrieve/pii/S2214860417301732.

[116] Christian Gorsche, Reghunathan Harikrishna, Stefan Baudis, Patrick Knaack, Branislav Husar, Joerg Laeuger, Helmuth Hoffmann, and Robert Liska. Real Time-NIR/MIR-Photorheology: A Versatile Tool for the in Situ Characterization of Photopolymerization Reactions. *Analytical Chemistry*, 89(9):4958–4968, may 2017. ISSN 0003-2700. doi: 10.1021/acs.analchem.7b00272. URL https://pubs.acs.org/doi/10.1021/acs.analchem.7b00272.

Appendices

Appendix A

Appendix of Supplemental Information for Chapter 2

A.1 H^1 NMR Spectra of ODPA

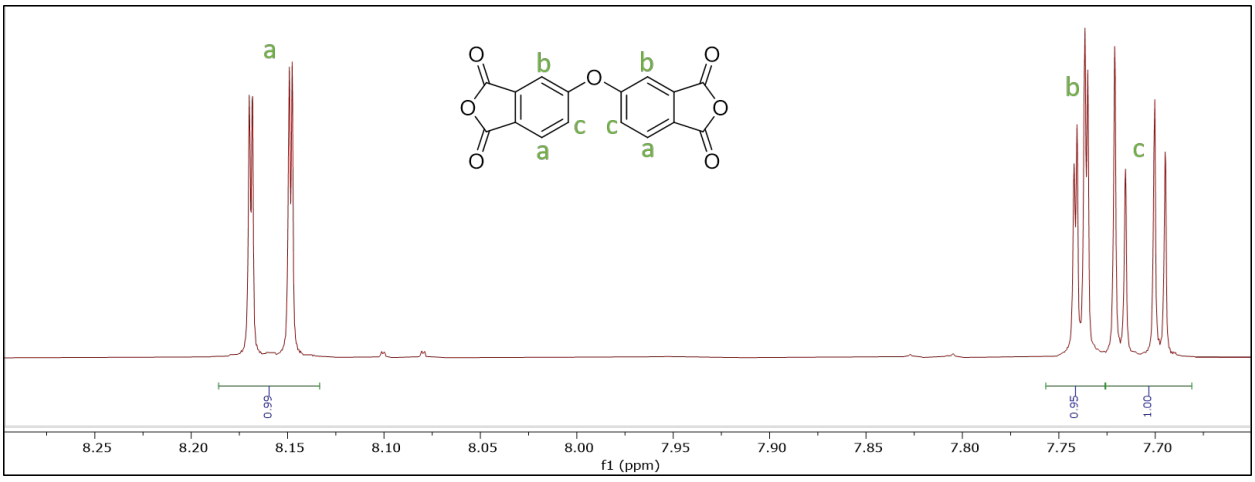

Figure A.1: ^{1}H NMR of ODPA as received from a chemical supplier.

A.2 H^1 NMR Spectra of ODPAC

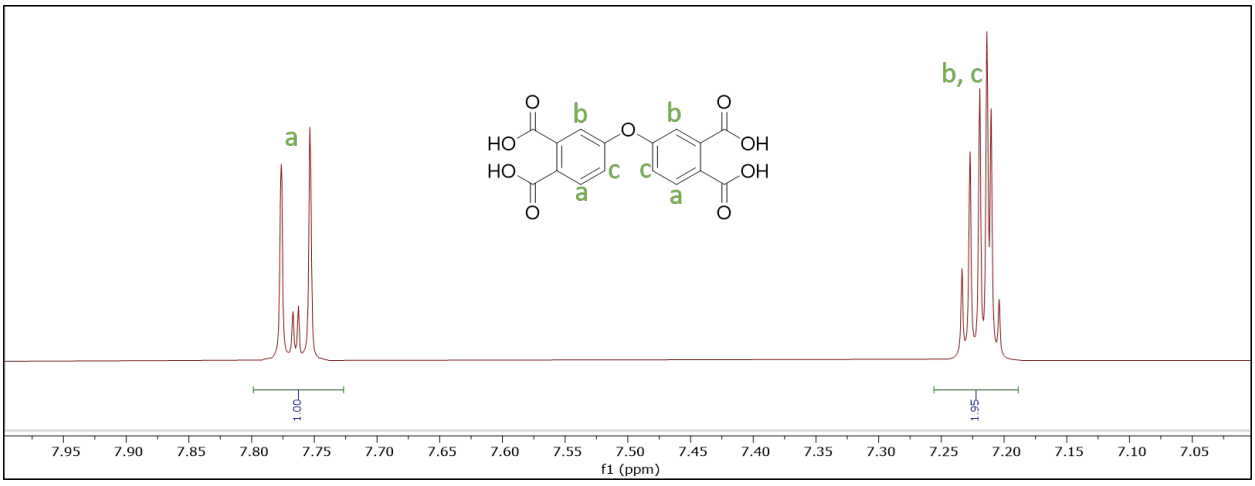

Figure A.2: ^{1}H NMR of ODPAC exhibiting quantitative conversion. Due to the adjacency of the carboxylic acids, acidic protons are not visible.

A.3 H[1] NMR Spectra of ODPAE

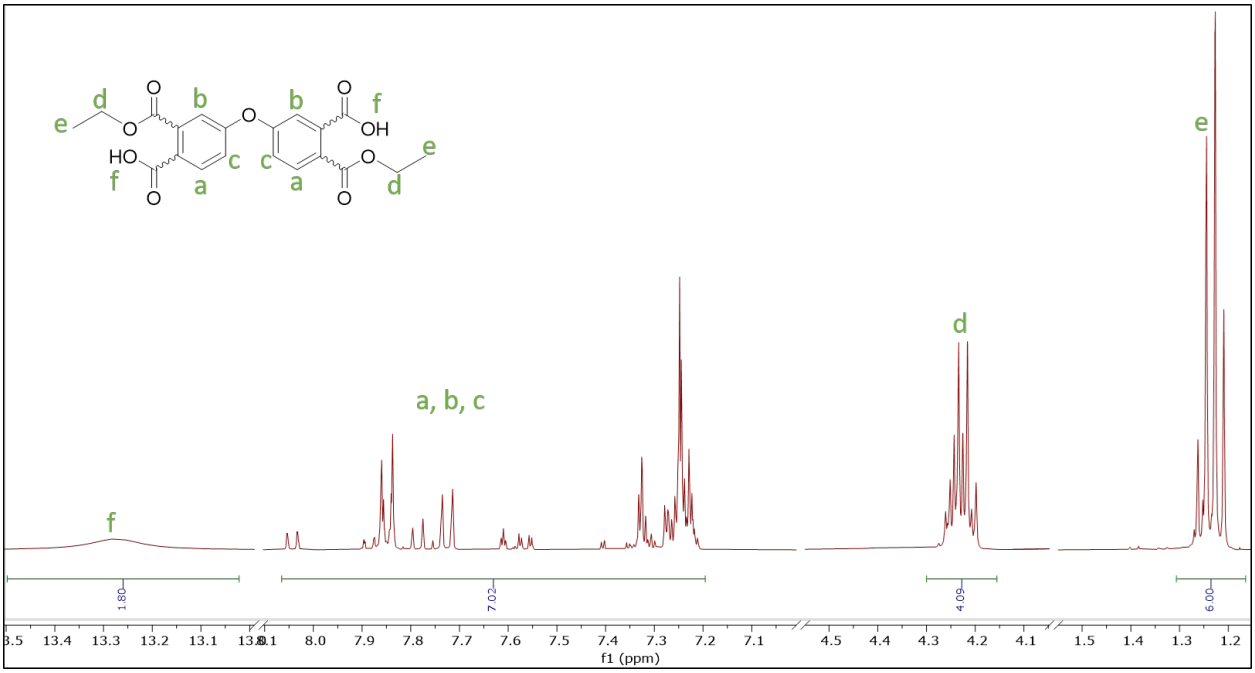

Figure A.3: [1]H NMR of the meta and para isomers of ODPAE. Due to the isomers present, specific aromatic peaks corresponding to each isomer were overlapping and unable to be identified. Aromatic proton integration is over-represented indicating an incomplete conversion or potential side reactions.

A.4 Photorheology complex viscosities of OPDAE-ODA and ODPAC-ODA polysalt resins

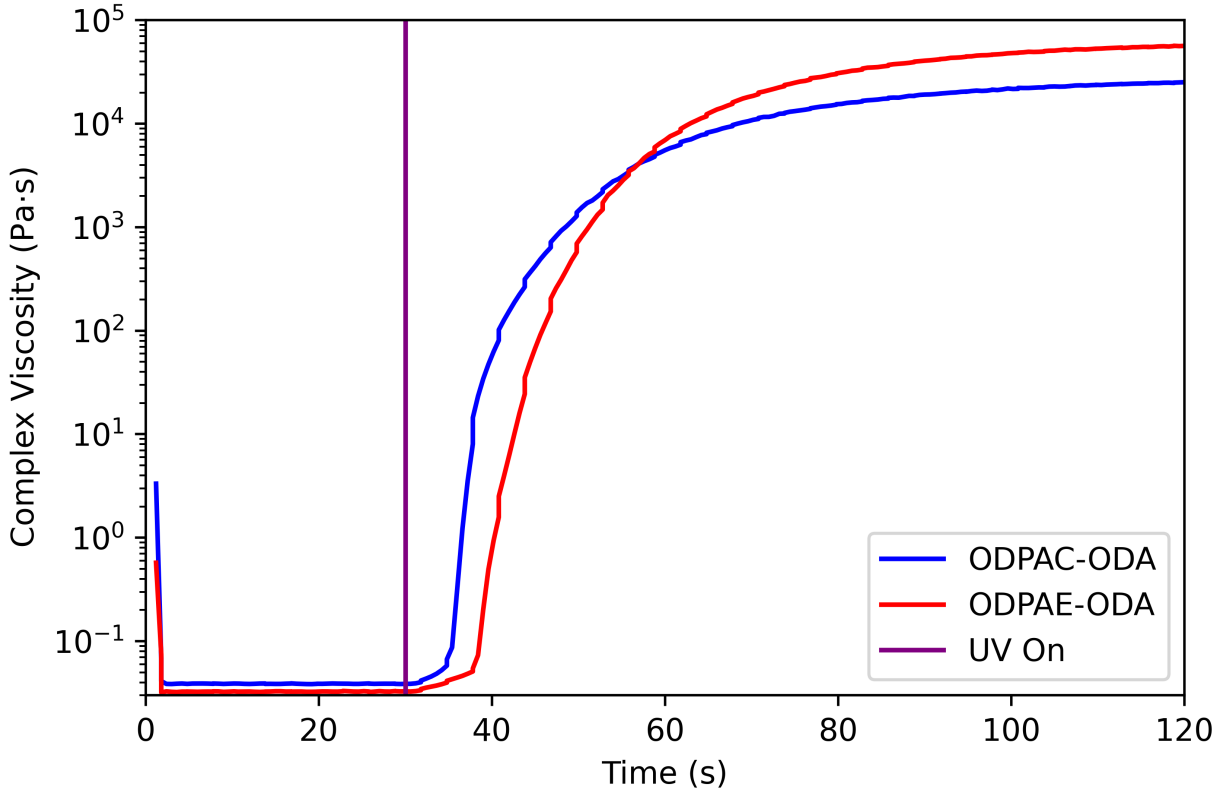

Figure A.4: Complex viscosity of OPDAE-ODA and ODPAC-ODA with respect to the exposure time. Resins exhibit low precured viscosities of approximately 0.03 Pa·s,

A.5 Printed thick parts of ODPAE-ODA

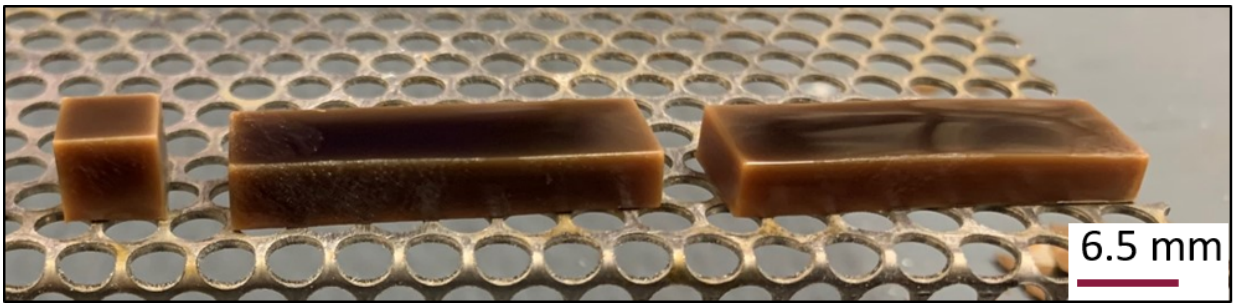

Figure A.5: Printed cube and rectangular parts after three days of air drying. Parts exhibit light edges corresponding to a higher rate of solvent loss.

A.6 SEM of ODPAC-ODA cross-sectioned lattice strut

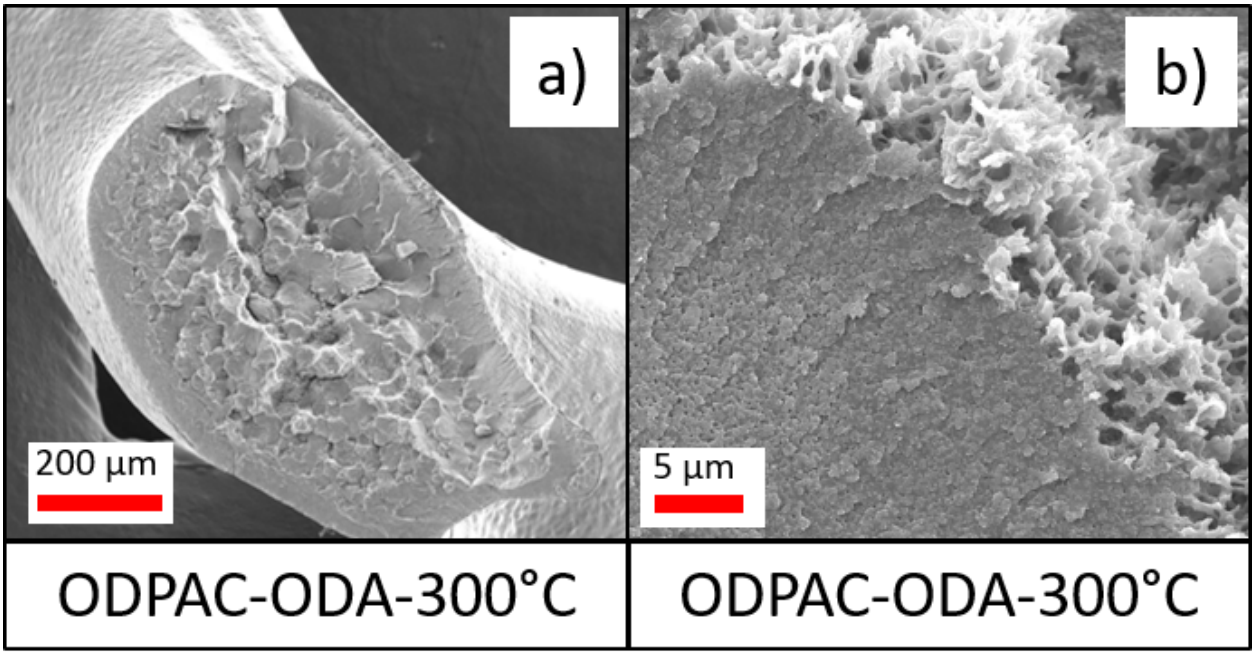

Figure A.6: SEM of printed lattice cross-section of ODPAC-ODA-300C at 30x (a) and 3000x (b) magnification. Unlike ODPAE-ODA, ODPAC-ODA maintains phase-separated morphology believed to be caused by reduced solvent evaporation and subsequent volatilization during heating.

A.7 SEM of ODPAE-ODA fracture surfaces

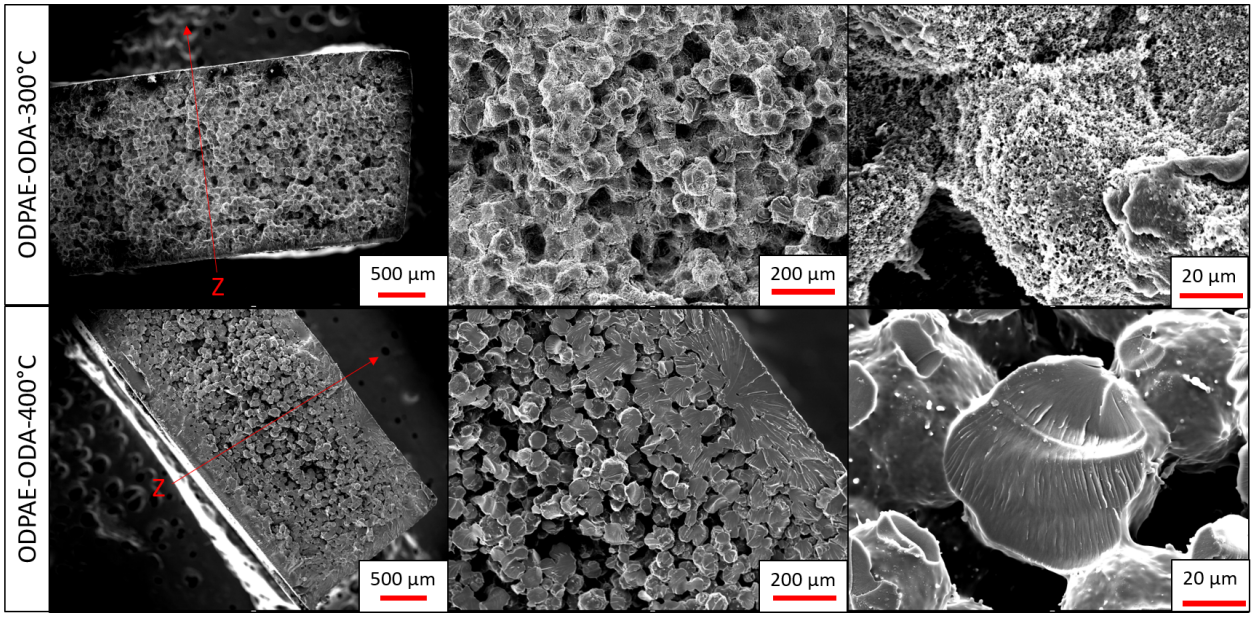

Figure A.7: SEM of ODPAE-ODA-300 (top) and ODPAE-ODA-400 (bottom) fracture surface. The printed direction is denoted in the left images. Printing layers are not detected but the density of the part appears higher near the edge of the parts forming, caused by faster solvent evaporation. Globular morphology and nanoscale porosity is observed within the sample but disappear/densifies upon heating to 400 ^{o}C.